

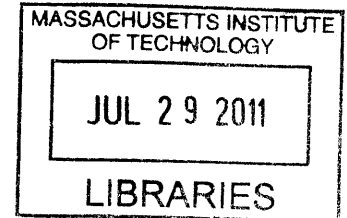
High-Resolution 3-D Refractive Index Imaging and Its Biological Applications

by

Yongjin Sung

B.S., Seoul National University (2000)

M.S., Seoul National University (2002)



Submitted to the Department of Mechanical Engineering
in partial fulfillment of the requirements for the degree of

ARCHIVES

Doctor of Philosophy in Mechanical Engineering

at the

MASSACHUSETTS INSTITUTE OF TECHNOLOGY

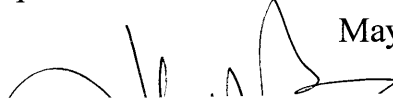
June 2011

© 2011 Massachusetts Institute of Technology. All rights reserved.

Signature of Author 

Department of Mechanical Engineering

May 20, 2011

Certified by 

George Barbastathis

Professor of Mechanical Engineering

Thesis Supervisor

Accepted by 

David E. Hardt

Chairman, Department Committee on Graduate Students

High-Resolution Three-Dimensional Imaging and Its Biological Applications

by

Yongjin Sung

Submitted to the Department of Mechanical Engineering
on May 20, 2011, in partial fulfillment of the
requirements for the degree of
Doctor of Philosophy in Mechanical Engineering

Abstract

This thesis presents a theory of 3-D imaging in partially coherent light under a non-paraxial condition. The transmission cross-coefficient (TCC) has been used to characterize partially coherent imaging in a 2-D and 3-D paraxial model. It is shown that the 3-D TCC under the non-paraxial condition is an overlap integral of three hemispheres or 3-D pupil functions. By an inspection of the overlap integral, a simple formula is derived that can be efficiently calculated by multiple applications of the 3-D fast Fourier transform (FFT) instead of a 6-D integral. The theory is applied to phase contrast and differential interference contrast (DIC), and it provides the most rigorous 3-D model that has ever been suggested.

Contrast-agent-free microscopy is highly desirable to study the dynamics and physiological activity of various structures in living cells. Refractive index is an intrinsic contrast source, but at the same time it is an important biochemical parameter that is proportional to the concentration of molecules. By measuring the refractive index quantitatively, the alteration of cells under chemicals or drugs as well as their normal physiological activities can be monitored in most native conditions. This thesis presents 3-D optical diffraction tomography (ODT) to retrieve the 3-D refractive index map of a transparent biological sample and applies them to some interesting biological problems: the study of cell growth and monitoring the effect of drugs on multiple myeloma cells.

In most practical applications of ODT, the angular coverage of an incident beam is limited due to finite system numerical aperture. The refractive index map reconstructed from the restricted data set suffers from the missing cone artifact: elongation of the reconstructed shape along the optical axis and underestimation of the value of the refractive index. This thesis presents that the missing-cone artifact can be effectively suppressed by applying positivity and piecewise-smoothness constraints in the iterative reconstruction framework. By filling the missing cone, a 3-D refractive index map can be reconstructed from the scattering into the entire $4\text{-}\pi$ solid angle. . With the improved accuracy, we attempt to quantify the dry mass of chromosomes in single living cells in their mitotic phase.

Thesis reader: Roger Kamm, Professor of Mechanical Engineering, and Biological Engineering, MIT

Thesis reader: Colin J. R. Sheppard, Professor and Head of the Division of Bioengineering, NUS

Thesis reader: Peter So, Professor of Mechanical Engineering, and Biological Engineering, MIT

Thesis Supervisor: George Barbastathis

Title: Professor of Mechanical Engineering

Acknowledgments

I would like to thank my advisors, the late Prof. Michael Feld for his guidance, and Prof. George Barbastathis for being my thesis advisor after Michael's passing. I deeply appreciate Prof. Robert Silbey and Prof. Andrei Tokmakoff in Spectroscopy Laboratory for their help and guidance through the faculty support program. I cannot thank enough to Dr. Ramachandra Dasari and Dr. Charles Holbrow for their support and having their doors open whenever I needed help.

I especially thank my thesis committee: Prof. Colin Sheppard for guiding me into the beautiful theory of 3-D partially coherent imaging; Prof. Roger Kamm for his insightful comments on the biological subjects in my research and his kind and warm support; Prof. Peter So for his support and helpful discussion on my research. I couldn't have finished my thesis without the help of my thesis committee.

I appreciate Prof. Marc Kirschner in Harvard Medical School for his collaboration with us on the cell cycle study, and invaluable comments on the research. I am grateful for my enthusiastic collaborators, Prof. Amit Tzur in Bar Ilan University and Dr. Giada Bianchi in Dana Farber Cancer Institute, who is in Mayo clinic now. I also thank Dr. Chen-rei Wan for providing cardiomyocyte samples, Dr. Laura Waller for insightful discussion as a colleague and a mentor in my class project.

Prof. Wonshik Choi in Korea University has been a brilliant colleague who taught me a lot of things about tomographic phase microscopy he developed, and a mentor I could rely on. I am so much privileged to interact with and learn from such talented people: Zahid Yaqoob, Niyom Lue, Dan Fu, Timothy Hilman, Seungeun Oh, Yongkeun Park, Jeon Woong Kang, Youngwoon Choi, Luis Galindo, and Zina Queen, just to name a few. I would also like to express many thanks to Korean students and researchers at MIT, colleagues in Hyundai Motor Company, and old friends of mine.

Financial support of the research projects described in this thesis was provided by NIH, NSF, and Hamamatsu corporation. I am also heartily grateful for the fellowship from Kwanjeong Lee Chong-Hwan Foundation. Most importantly, I would like to thank my parents and my sister Ji-Hyun for their prayers, endless support and love. Finally, I'd like to thank my better half, lovely wife Jae Yung. She makes me wish to be a good person like her.

I will miss every moment I spent at MIT, and I wish my learning can be used for something good.

Contents

1. Introduction	13
1.1. Imaging Transparent Biological Samples	13
1.2. Outline of the Thesis	16
2. Theory of 3-D Partially Coherent Imaging	19
2.1. Development of the Theory of Optical Imaging	19
2.1.1. 2-D Coherent Imaging	19
2.1.2. 2-D Partially Coherent Imaging	21
2.1.3. Imaging of 3-D Objects	22
2.2. 3-D PCTF under Non-Paraxial Condition	24
2.3. Simple Formula for 3-D Partially Coherent Imaging	28
2.4. Application to Phase Contrast and Nomarski Differential Interference Contrast (DIC)	33
3. 3-D Refractive Index Imaging by Quantitative Phase Measurement	39
3.1. Tomographic Phase Microscopy (TPM)	39
3.1.1. Quantitative Phase Imaging	39
3.1.2. Tomographic Reconstruction of 3-D Refractive Index Map	42
3.2. Optical Diffraction Tomography	44
3.2.1. Fourier Diffraction Theorem	44
3.2.2. Data Acquisition and Processing	46

3.2.3. Born vs. Rytov Approximation	50
3.2.4. Comparison with Inverse Radon Approach	52
4. Cellular Dry Mass Measurement	57
4.1. Refractive Index and Cellular Dry Mass	57
4.2. Tomographic Measurement of Cellular Dry Mass	59
4.3. Cell Growth Study	63
4.3.1. Background	63
4.3.2. Results and Discussion	64
4.4. Drug Effect Monitoring of Multiple Myeloma Cells	67
4.4.1. Background	67
4.4.2. Results and Discussion	69
5. $4\text{-}\pi$ Tomographic Phase Microscopy	75
5.1. Introduction	75
5.2. Iterative Reconstruction with Additional Constraints	78
5.2.1. Diffraction Tomography as Inverse Problem	78
5.2.2. Edge Preserving Regularization	81
5.2.3. Effect of Constraints on Missing Angle Recovery	83
5.3. Stain-Free Chromosome Imaging in Live Cells	89
5.3.1. Bead Calibration	89
5.3.2. Dry Mass of Chromosomes	91
6. Summary and Future Directions	95
6.1. Summary	95
6.2. Future Directions	97

List of Figures

1-1	Images of human glial brain tissue by (a) bright field and (b) phase contrast (Nikon website). (c) Schematic diagram of Zernike's phase contrast microscopy	15
2-1	2-D image formation in coherent light	20
2-2	2-D image formation in partially coherent light	22
2-3	Bragg condition	23
2-4	Optical transfer of a point source	24
2-5	Graphical representation of the 3-D TCC under non-paraxial condition	28
2-6	Modified 3-D Shepp-Logan phantom	31
2-7	$C_{point}(\vec{p}_1; \vec{p}_2)$ in \vec{p}_2 space	32
2-8	Horizontal cross-sections of bright field image reconstructed using (a) line, and (b) point intersection terms (after subtracting background)	33
2-9	2-D pupil functions used for the calculation of the phase contrast	34
2-10	Schematic of a DIC microscope with two typical Wollaston prisms	34
2-11	Comparison of cross-sections imaged by (a),(d) bright field, (b),(e) phase contrast and (c),(f) Nomarski DIC	36
2-12	Cross-sections of the effective transfer function for Nomarski DIC	37
3-1	Examples of quantitative phase measurement techniques	40
3-2	Data processing for Hilbert phase microscopy	42
3-3	Tomographic phase microscopy	43
3-4	Mapping of the complex E-field onto the 3D Fourier space of the object function	48
3-5	Iterative constraint algorithm	49
3-6	Comparison of the Born and Rytov approximations in diffraction tomography	51
3-7	Comparison between filtered back-projection algorithm and	

	diffraction tomography with the Rytov approximation	53
3-8	Bright field images, and 3D tomogram of HT-29 cells reconstructed by the filtered back-projection algorithm and diffraction tomography	55
4-1	(a) Composition of biological cells, and (b) linear relationship of the refractive index and the concentration of substances in solution	58
4-2	(a) Projection assumption, (b-c): diffraction corrected measurement of dry mass	59
4-3	(a) Experimental set-up for spiral-scan tomographic phase microscopy, (b) spiral scan path of an incident beam, (c) phase image calculated by the method suggested in this paper	61
4-4	Bead defocus test	62
4-5	Phase delay induced by a RKO cell	63
4-6	Division asymmetry of eukaryotic cells	66
4-7	Collins-Richmond model for HT-29 (a-c) and RKO cells (d-f)	68
4-8	Volume and dry mass of normal plasma cells and MM.1S multiple myeloma cells	71
4-9	Cross-section of refractive index map of a RPMI8226 human myeloma cell at 0hr and 4hr after the treatment (20nM bortezomib)	71
4-10	Dry mass change after adding proteasome inhibitor (20nM bortezomib) to MM.1S and RPMI8226 cells (140 cells for each)	72
4-11	Dry mass change after adding proteasome inhibitor (20nM bortezomib) to MM.1S (multiple myeloma) cells (140 cells for each)	73
4-12	Dry mass change after adding proteasome inhibitor (20nM bortezomib) to RPMI8226 (multiple myeloma) cells (140 cells for each)	73
4-13	Dry mass change after adding proteasome inhibitor of various concentrations to RPMI8226 (multiple myeloma) cells (140 cells for each)	74
5-1	Transfer function of diffraction tomography and some results of reconstruction	77
5-2	Modified 3-D Shepp-Logan phantom and its scattering fields calculated for various illumination angles	80
5-3	Noise handling capability of edge preserving regularization	82
5-4	Flow chart for the iterative reconstruction with the positivity and the piecewise smoothness constraints	84
5-5	Simulation with a spherical bead	86

5-6	(a) A spherical bead squashed in the optical axis direction with the aspect ratio of 2 to 1, (b) spatial frequency spectrum of (a)	86
5-7	Simulation with a squashed bead in Fig. 6(a)	87
5-8	non-homogeneous sample consisting of two regions of different refractive index	88
5-9	Simulation with a non-homogeneous sample representing a biological cell	88
5-10	Fourier mapping and direct inversion	89
5-11	Iterative reconstruction with the positivity and the piecewise smoothness constraint	91
5-12	Dry mass of chromosomes	93
6-1	(a) Transfer function of diffraction tomography in transmission mode. (b) $U-W$ cross-section of the transfer function in transmission and reflection mode	98

List of Tables

4-1 Specific refraction increments of some substances of biological importance 58

Chapter 1

Introduction

1.1. Imaging Transparent Biological Samples

Optical microscopes have long become essential tools for biology and medicine, and recent innovations in optical microscopic techniques continue to bring unprecedented capability to the hands of biologists and clinical researchers by pushing the limits of the conventional microscopes: achieving higher spatial resolution; expanding imaging depth; and inventing new ways to obtain useful information from biological samples. Currently, fluorescence-based techniques are prevalent because of their capability to provide molecular specific information with high spatial and temporal resolution [1-5]. However, it is difficult to quantify the fluorescence signal, and the effects of exogenous agents or genetic manipulation on cell physiology remain unknown [6].

Contrast-agent-free microscopy is highly desirable to study the dynamics and physiological activity of various structures in living cells. In such techniques as phase contrast, differential interference contrast (DIC), quantitative phase imaging, etc., the source of image contrast is the refractive index, more precisely the spatial variation of the refractive index. The variation of refractive index is usually very weak, so it requires the modulation of light to enhance the contrast. For example, Zernike's phase contrast puts a quarter-wave dot on the optical axis at the Fourier plane [7]; Nomarski DIC adopts two Wollaston prisms to generate the interference of two beams travelling through a sample with a slight lateral shift [8];

and quantitative phase imaging utilizes the interference of a sample beam and a modulated reference beam [9-11].

To demonstrate the advantage of such light modulation, bright field imaging and Zernike's phase contrast are compared using a simple 2-D model. For a purely transparent sample with negligible absorption, the field amplitude and the intensity of the bright field image may be written, respectively:

$$\begin{aligned}
 E(x, y) &\approx E_s(x, y)(1 + i\varphi(x, y)), \\
 I(x, y) &\approx |E_s(x, y)|^2(1 + \varphi(x, y)^2),
 \end{aligned} \tag{1.1}$$

in which $E_s(x, y)$ is the complex amplitude of an incident field, $\varphi(x, y)$ is the sample-induced phase delay. For biological samples, $\varphi(x, y)^2$ is usually very small compared to one, so the sample looks nearly transparent under a bright field microscope.

Figure 1.1(a) shows a bright field image of human glial brain tissue, which does not show detailed morphology of cells at all. Figure 1.1(c) shows a schematic diagram of Zernike's phase contrast microscopy. By putting a quarter wave dot on the optical axis at the Fourier plane, it modulates the light to enhance the contrast of a sample. Under the assumption that the aperture of the light source is small, the field amplitude and the intensity of the phase contrast image may be written by

$$\begin{aligned}
 E(x, y) &\approx E_s(x, y)i(1 + \varphi(x, y)), \\
 I(x, y) &\approx |E_s(x, y)|^2(1 + 2\varphi(x, y)).
 \end{aligned} \tag{1.2}$$

In Eq. (1.2), the sample-induced phase delay $\varphi(x, y)$ is included as a first order term, so the sample under a phase contrast microscope can provide remarkably enhanced contrast as shown in Fig. 1.1(b).

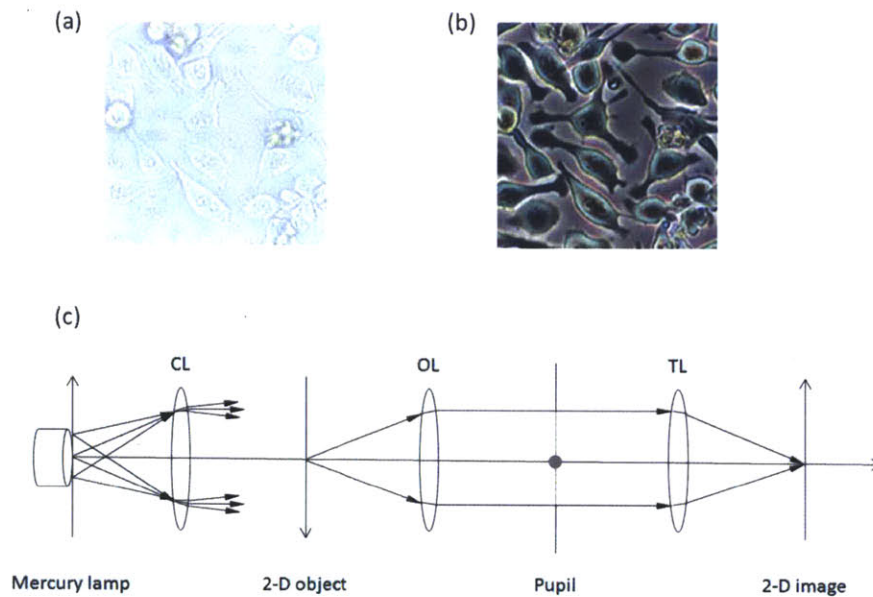


Figure 1.1. Images of human glial brain tissue by (a) bright field and (b) phase contrast [12]. (c) Schematic diagram of Zernike's phase contrast microscopy. A quarter wave dot is placed on the optical axis at the Fourier plane of the objective lens. CL: condenser lens; OL: objective lens; TL: tube lens.

This simple example demonstrates how light modulation enhances the contrast of a 2-D transparent specimen in the Zernike's phase contrast microscopy adopting a low numerical aperture illumination and imaging lenses. In practice, a sample is 3-D, and a high numerical aperture system is adopted to improve the resolution. Hence, a more rigorous theory of optical imaging is required. It will help to develop new imaging modalities and to retrieve more accurate information about a sample from its image. The importance of formulating such a theory cannot be overlooked. Historically, Zernike could develop the principle of phase contrast microscopy only based on the theoretical foundation that Abbe had laid [13].

Refractive index is an intrinsic contrast source, but at the same time it is an important biochemical parameter that is proportional to the concentration of molecules [14, 15]. By measuring the refractive index quantitatively, the alteration of cells under chemicals or drugs as well as their normal physiological activities can be monitored in most native conditions. This thesis presents 3-D optical diffraction tomography (ODT) to retrieve the 3-D refractive index map of a sample and applies them to some

interesting biological problems: the study of cell growth and monitoring the effect of drugs on multiple myeloma cells. In most practical applications of ODT, the angular coverage of an incident beam is limited due to finite system numerical aperture. The refractive index map reconstructed from the restricted data set suffers from the missing cone artifact: elongation of the reconstructed shape along the optical axis and underestimation of the value of the refractive index. This thesis presents that the missing-cone artifact can be effectively suppressed by applying positivity and piecewise-smoothness constraints in the iterative reconstruction framework.

1.2. Outline of the Thesis

Chapter 2 presents a theory of 3-D imaging in partially coherent light under a non-paraxial condition. The transmission cross-coefficient (TCC) has been used to characterize partially coherent imaging in a 2-D and 3-D paraxial model. It is shown that the 3-D TCC under the non-paraxial condition is an overlap integral of three hemispheres or 3-D pupil functions: a condenser pupil function, an objective pupil function, and the complex conjugate of the objective pupil function. By an inspection of the overlap integral, a simple formula is derived that can be efficiently calculated by multiple applications of the 3-D fast Fourier transform (FFT) instead of a 6-D integral. The theory is applied to phase contrast and differential interference contrast (DIC), and it provides the most rigorous 3-D model that has ever been suggested.

Chapter 3 presents high-resolution 3-D refractive index imaging using quantitative phase measurements. It proceeds by summarizing the 2-D quantitative phase imaging techniques that can measure the sample-induced phase delay. Combined with a tomographic method, quantitative phase imaging can provide 3-D refractive index map of a transparent sample. So-called tomographic phase microscopy (TPM) is a unique methodology that can image a live biological sample in 3-D without adding any additional contrast agents. The original version of TPM adopted a filtered back-projection algorithm that generates a diffraction

artifact. We demonstrate that optical diffraction tomography based on the scattering theory can suppress this artifact. In addition, we show the first Rytov approximation is more appropriate for biological samples than the first Born approximation. A simple iterative constraint algorithm using a positivity constraint is shown to help reduce the effect of missing spatial frequencies.

Chapter 4 presents the optical measurement of cellular dry mass, the mass of non-aqueous contents within a cell, and its application to some interesting biological problems. A method using tomographic synthesis is suggested to provide the cellular dry mass without diffraction artifacts and coherent speckle noise. Using the tomographic method, we measure cell division and demonstrate that it is a highly asymmetric process depending on cell type. By measuring the dry mass distribution of newborn cells and mitotic cells in addition to asynchronous populations, and using the Collins-Richmond model, we provide the growth curve for two types of adherent cells, HT-29 and RKO cells. Also we demonstrate that the response of multiple myeloma cells to a drug (bortezomib) can be monitored by measuring the change of dry mass. The dry mass measurement can distinguish the effect of drug within a couple of hours, faster than other techniques targeting the signatures of the apoptosis such as translocation of plasma membrane.

In Chapter 5, it is shown that the missing-cone artifact can be effectively suppressed by applying positivity and piecewise-smoothness constraints in the iterative reconstruction framework. By filling the missing cone, a 3-D refractive index map can be reconstructed from the scattering into the entire $4\text{-}\pi$ solid angle. Importantly, $4\text{-}\pi$ TPM can recover sharp edges rounded out by the missing cone, and significantly improve the accuracy of the predictions of refractive index. We also demonstrate the noise handling capability of our algorithm. With the improved accuracy, we attempt to quantify the dry mass of chromosomes in single living cells in their mitotic phase and determine the ploidy of the cells.

Finally, Chapter 6 states conclusions and future work.

Chapter 2

Theory of 3-D Partially Coherent Imaging

Reproduced in part with permission from Yongjin Sung and Colin J. R. Sheppard, "Three-dimensional imaging by partially coherent light under nonparaxial condition," J. Opt. Soc. Am. A 28, 554-559 (2011).

2.1. Development of the Theory of Optical Imaging

2.1.1. 2-D Coherent Imaging

Spatial coherence of light refers to its ability to interfere with a spatially shifted version of itself [16]. For example, the points on the wavefront of the expanded laser beam are mutually spatially coherent, while the points on an incandescent light source, e.g. mercury lamp, are mutually spatially incoherent. Optical imaging records the interference of the light passing through a sample along different paths, so the spatial coherence of the illumination significantly affects the image characteristics.

Abbe's theory was the first to characterize 2-D coherent imaging in terms of diffraction phenomena of light [17]. Any 2-D real object can be represented by a linear superposition of 2-D gratings with various spatial frequencies [18]:

$$I(x, y) = \iint_{\sigma} T(u, v) e^{i2\pi(ux+vy)} du dv, \quad (2.1)$$

where $t(x, y)$ is the transmittance function for a 2-D object. $T(u, v)$ is the Fourier component of $t(x, y)$, and can be considered as a grating of spatial frequency (u, v) .

Without aberration, 2-D optical imaging is a linear and shift-invariant process; the imaging of a 2-D grating with a specific spatial frequency is enough to characterize an optical system. In Fig. 2.1, an expanded laser beam is incident onto a grating with spatial frequency $(\mu, 0)$, and diffracted beams are imaged by a 4-f system.

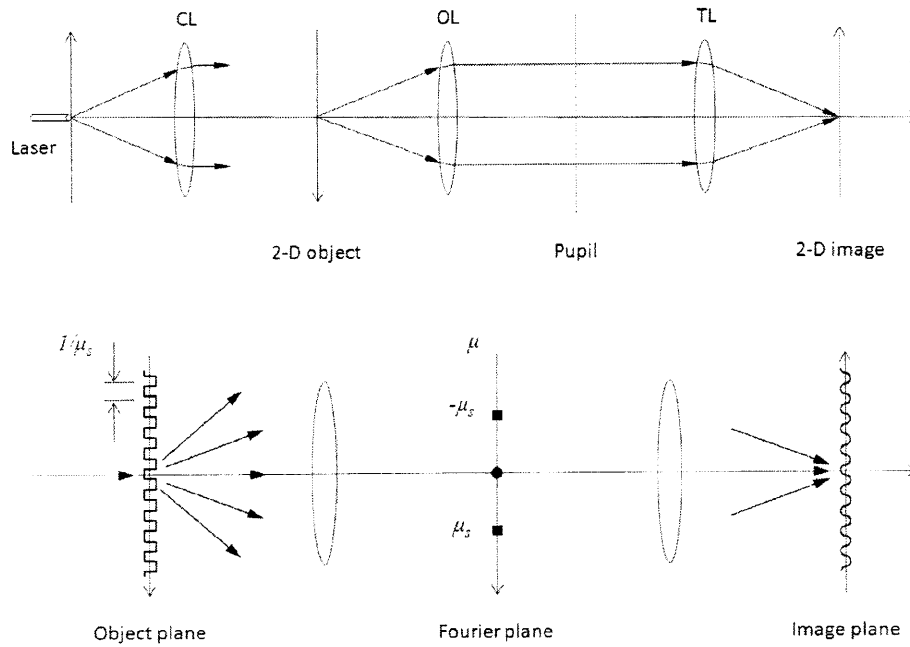


Figure 2.1. 2-D image formation in coherent light. CL: condenser lens; OL: objective lens; TL: tube lens. The physical size of lenses is limited, so only the lowest-order beams, the 0th and ± 1 st order in the figure, can pass through the lens pupils and be collected in the image plane. Because of this low-pass filtering, detailed features of a sample are lost during the imaging process. The image of a more complicated sample can be written as

$$I(x, y) = \iint_{-\infty}^{\infty} T(u, v) P(u, v) e^{i2(\mu x + \nu y)} du dv, \quad (2.2)$$

where $P(u, v)$ is an objective pupil function, which is the characteristic function that has value 1 within the circle of radius μ (μ is slightly larger than μ_s) and 0 outside. The lens aberration or various apodization effects can be included in the pupil function.

2.1.2. 2-D Partially Coherent Imaging

The light field emitted from the incoherent source acquires spatial coherence as it travels by the Van Cittert-Zernike theorem [16]; it becomes partially coherent. Most microscopic imaging including phase contrast, differential interference contrast (DIC) falls on this category. Figure 2.2 illustrates the image formation by partially coherent light, and how it is different from the coherent case. According to the Van Cittert-Zernike theorem, the coherence of the illumination depends on the size of the mercury lamp. For Köhler illumination, the partially coherent light incident on an object can be represented by a superposition of plane waves each of which has random phase fluctuations with respect to the others [16].

In the lower part of Fig. 2.2 three plane wave components that constitute the incident light are picked out and shown. The grating diffracts each plane wave into multiple orders, but the diffracted beams are angularly shifted by the amount of the incident angle onto a sample. The angular shifting of the diffracted beams enables higher order beams that were cut-off in the coherent case, e.g., the ± 2 nd order in Fig. 2.2 to pass through the lens pupils. The components add on an irradiance basis in the image plane to form a representation of the object. Hence, partially coherent imaging can provide better resolution than coherent imaging.

The image of a 2-D object formed by partially coherent illumination can be described in terms of the transmission cross coefficient (TCC) [19, 20], which is also known as partially coherent transfer function (PCTF):

$$I(x, y) = \iiint \int T(m, n) T^*(p, q) C(m, n; p, q) \exp[i2\pi\{(m-p)x + (n-q)y\}] dm dn dp dq. \quad (2.3)$$

where $C(m, n; p, q) = \iint P_{cond}(\xi, \eta) P_{obj}(\xi - m, \eta - n) P_{obj}^*(\xi - p, \eta - q) d\xi d\eta$ is the 2-D TCC, $P_{cond}(\xi, \eta)$ and $P_{obj}(\xi, \eta)$ are the condenser and objective pupil functions, respectively.

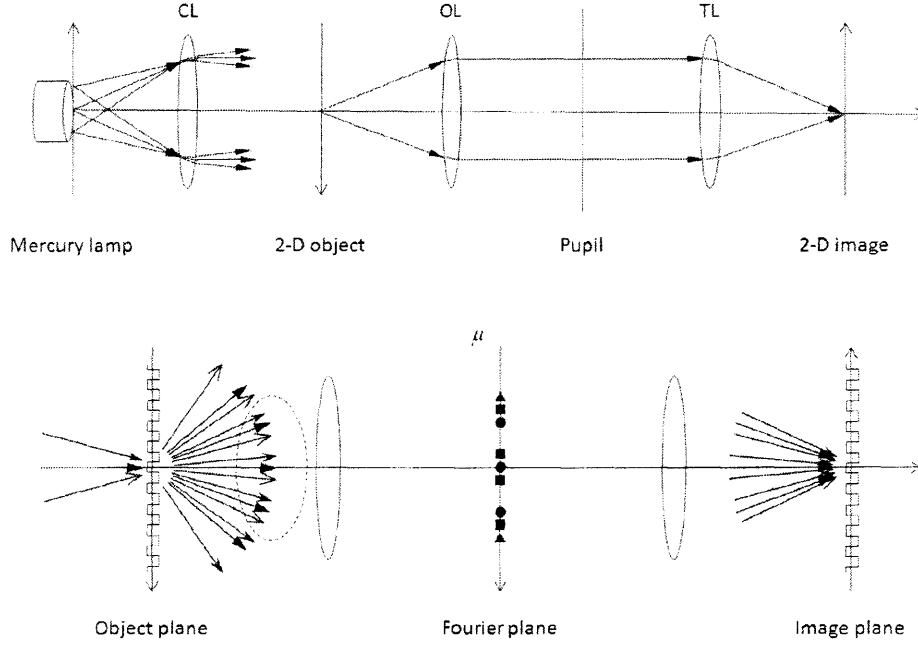


Figure 2.2. 2-D image formation in partially coherent light. The 0th, ± 1 st and ± 2 nd order components of the grating are shown as a filled circle, rectangle and triangle, respectively.

2.1.3. Imaging of 3-D Objects

In the imaging of an object with finite thickness, the Bragg condition needs to be considered in addition to the high frequency cut-off and the spatial coherence of illumination. The Bragg condition requires that the incident wave vector, diffracted wave vector, and object spectrum satisfy the following relations:

$$(U, V, W) = \vec{k}_d - \vec{k}_i,$$

$$|\vec{k}_i| = |\vec{k}_d|, \tag{2.4}$$

where \vec{k}_i and \vec{k}_d are the incident and diffracted wave vectors, respectively, U , V , and W are the spatial frequencies in the object frame corresponding to the spatial coordinates X , Y , and Z , respectively. The locus of points (U, V, W) satisfying Eq. (2.4) is a sphere, known as the Ewald's sphere. Only the object spectrum that lies on the Ewald sphere can be retrieved for the given incident beam. In transmission mode, only one-half of the sphere (a hemisphere) is accessible, which is further limited by the numerical aperture of the imaging system. Figure 2.3 demonstrates the Bragg condition for an incident beam introduced along the $+Z$ -axis. The Bragg condition is responsible for the missing cone problem that will be explained in the next chapter.

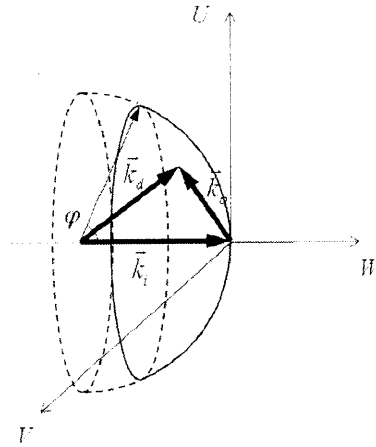


Figure 2.3. Bragg condition. (U, V, W) is the spatial frequency corresponding to the spatial coordinate (X, Y, Z) . The wave vectors of the incident beam, the diffracting beam and the object spectrum are represented by \vec{k}_i , \vec{k}_d and \vec{k}_o , respectively. φ is the numerical aperture of the system.

The 3-D transfer function has been developed within the first Born approximation by several researchers. McCutchen [21] showed that the 3-D coherent transfer function is a projection of an objective pupil onto the Ewald sphere. For incoherent imaging, Frieden [22] derived the 3-D optical transfer function under the paraxial approximation, and Sheppard [23] derived an analytic formula for the non-paraxial case. For partially coherent imaging, Streibl [24-26] described 3-D image formation in terms of the mutual intensity transfer, and Sheppard and Mao [27] derived a more general formula in terms of the transmission cross-

coefficient (TCC) or the partially coherent transfer function (PCTF). However, both approaches used the paraxial approximation, which is more suitable for a low numerical aperture system. In the next section, the 3-D PCTF is derived under non-paraxial, but scalar and Debye, approximation.

2.2. 3-D PCTF under Non-Paraxial Condition

We start from the optical transfer of the Green's function for the Helmholtz operator. Consider a point source in the 4-f imaging system as shown in Fig. 2.4.

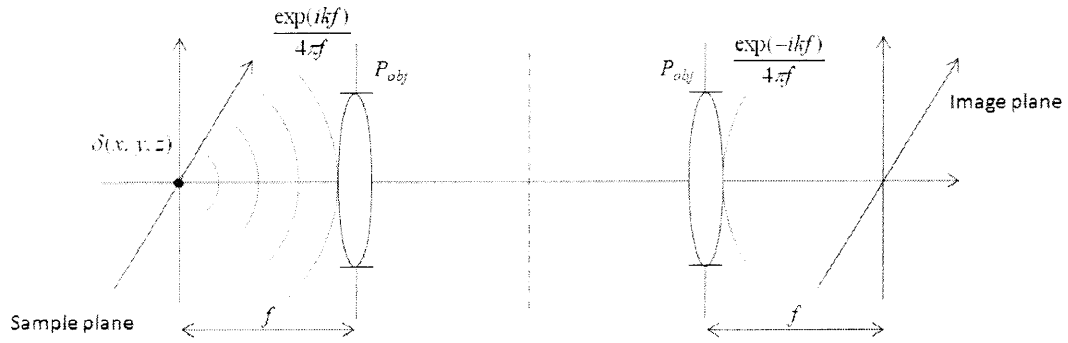


Figure 2.4. Optical transfer of a point source.

Spherical waves emitted from the point source are described by the Green's function, $G_0(\vec{x})$ for the Helmholtz operator [28].

$$(\nabla^2 + k_0^2)G_0(\vec{x}) = -\delta(\vec{x}), \quad (2.5)$$

in which $k_0 = 2\pi/\lambda$, λ is the wavelength of the incident beam in the medium, and $\vec{x} = (X, Y, Z)$ is the spatial coordinate.

From the symmetry of the imaging system, the field right after the second objective lens is the converging wavefront cut off by the finite numerical aperture. Under the Debye approximation, the field distribution in the image space formed by the finite converging wavefront can be expressed as [21]:

$$U(\vec{r}) = \frac{1}{i4\pi\lambda} \iint_{\Omega} A(\vec{q}) e^{-i2\pi\vec{q}\cdot\vec{r}} d\Omega, \quad (2.6)$$

in which \vec{r} is a spatial coordinate vector normalized by λ , dS is the incremental area on the converging wavefront, $d\Omega$ is the incremental solid angle which dS subtends at the origin of the image space, \vec{q} is a unit vector in the direction from the origin to dS . Note that the Debye approximation is not really an approximation if the lens pupils are placed in the back focal planes of the lenses, as is usual in practice. McCutchen [21] found that the Fourier transform of Eq. (2.6) can be connected to the pupil function of the objective lens, which can be written in the current notation as

$$\tilde{U}(\vec{p}) = \frac{1}{i4\pi\lambda} P_{obj}(u, v) \delta(|\vec{p}| - 1), \quad (2.7)$$

where $\vec{p} = (u, v, w)$ is a frequency vector corresponding to the normalized spatial coordinate $\vec{r} = (x, y, z)$, $P_{obj}(u, v)$ is the 2-D objective pupil function, $\delta(|\vec{p}| - 1)$ represents the projection of the pupil function onto the Ewald sphere.

Now we consider the scattering of transmitted light by a 3-D sample, and its transfer through the imaging system. Under the first Born approximation, the scattered field in the image space can be written

$$u_{scat}(\vec{x}) = - \int u_{in}(\vec{x}') f(\vec{x}') U(\vec{x} - \vec{x}') d^3x', \quad (2.8)$$

in which $u_{in}(\vec{x})$ is the incident field, $f(\vec{x})$ is the scattering potential defined as [29]

$$f(\vec{x}) = k_0^2 (n_0^2 - n(\vec{x})^2), \quad (2.9)$$

where $n(\vec{x})$ is the complex refractive index, and n_0 is the refractive index of the medium. (i.e. not of free space. The refractive index changes are smaller with respect to the medium.)

Normalizing the spatial coordinates by $\bar{r} = \bar{x}/\lambda$ in Eq. (2.8), and including the transfer of the incident field, we can write the output field in the image space as follows:

$$u_{out}(\bar{r}) = \int u_{in}(\bar{r}') T(\bar{r}') H(\bar{r} - \bar{r}') d^3 r', \quad (2.10)$$

in which $T(\bar{r}) = 1 + i\pi(n_0^2 - n(\bar{r})^2)$, $H(\bar{r}) = i4\pi\lambda U(\bar{r})$, $\tilde{H}(\bar{p}) \equiv F\{H(\bar{r})\} = P_{obj}(u, v)\delta(|\bar{p}| - 1)$.

Note that Eq. (2.10) assumes that 3-D imaging is space invariant, as also assumed by Frieden [22]. But it is known that 3-D imaging cannot be space invariant, as a defocus of the image plane will introduce aberration if the sine condition is satisfied. This problem can be overcome by interpreting Eq. (2.10) as referring to direct imaging in the transverse coordinates, but to scanning the object axially to bring the relevant plane of the object to the conjugate of the image plane. This is exactly what is done in practice in generating a 3-D image data set.

The partially coherent imaging can be described more easily by the mutual intensity defined as follows:

$$J_{out}(\bar{r}_1; \bar{r}_2) = \langle u_{out}(\bar{r}_1, t) u_{out}^*(\bar{r}_2, t) \rangle. \quad (2.11)$$

Substituting Eq. (2.10),

$$J_{out}(\bar{r}_1; \bar{r}_2) = \iint T(\bar{r}_1') T^*(\bar{r}_2') J_{in}(\bar{r}_1'; \bar{r}_2') H(\bar{r}_1 - \bar{r}_1') H^*(\bar{r}_2 - \bar{r}_2') d^3 r_1' d^3 r_2', \quad (2.12)$$

where $J_{in}(\bar{r}_1; \bar{r}_2)$ is the mutual intensity of the incident light.

Under the Debye approximation, $J_{in}(\bar{r}_1; \bar{r}_2)$ can be simplified to a function only of $\Delta\bar{r} = \bar{r}_1 - \bar{r}_2$ [6,12].

$$J_{in}(\bar{r}_1; \bar{r}_2) \approx J_{in}(\Delta\bar{r}) = \int \tilde{J}_{in}(\bar{p}) \exp[i2\pi(\bar{p} \cdot \Delta\bar{r})] d^3 p, \quad (2.13)$$

where $\tilde{J}_m(\vec{p}) = |P_{\text{cond}}(u, v)|^2 \delta(|\vec{p}| - 1)$, $|\vec{p}| = (u, v, w)$. This is equivalent to assuming a Schell model illumination beam in which the illumination intensity is uniform, which is a good approximation for Köhler microscope illumination.

For convenience, we use the linear system approach that Goodman [16, 18] adopted for the partially coherent imaging of a 2-D object. For the 3-D imaging, here we define a 6-D Fourier transform as follows:

$$\tilde{J}_{\text{out}}(\vec{p}_1; \vec{p}_2) \equiv \iint J_{\text{out}}(\vec{r}_1; \vec{r}_2) \exp[-i2\pi(\vec{p}_1 \cdot \vec{r}_1 + \vec{p}_2 \cdot \vec{r}_2)] d^3 r_1 d^3 r_2. \quad (2.14)$$

The 6-D Fourier transform of the mutual intensity in the image space can be written as

$$\tilde{J}_{\text{out}}(\vec{p}_1; \vec{p}_2) = \tilde{H}(\vec{p}_1) \tilde{H}^*(-\vec{p}_2) \int \tilde{J}_m(\vec{p}) \tilde{T}(\vec{p}_1 - \vec{p}) \tilde{T}^*(-\vec{p}_2 - \vec{p}) d^3 p, \quad (2.15)$$

in which $\tilde{T}(\vec{p}) \equiv \int T(\vec{r}) \exp[-i2\pi(\vec{p} \cdot \vec{r})] d^3 r$, and $\tilde{H}(\vec{p})$, $\tilde{J}_m(\vec{p})$ are defined in Eq. (2.10) and (2.13), respectively.

The corresponding intensity can be calculated by

$$I_{\text{img}}(\vec{r}) = J_{\text{out}}(\vec{r}; \vec{r}) = \iint \tilde{J}_{\text{out}}(\vec{p}_1; \vec{p}_2) \exp[i2\pi(\vec{p}_1 + \vec{p}_2) \cdot \vec{r}] d^3 p_1 d^3 p_2. \quad (2.16)$$

To summarize, under the non-paraxial condition the image intensity of a 3-D object by partially coherent light can be written as follows:

$$I_{\text{img}}(\vec{r}) = \iint C(\vec{p}_1; \vec{p}_2) \tilde{T}(\vec{p}_1) \tilde{T}^*(\vec{p}_2) \exp[i2\pi(\vec{p}_1 - \vec{p}_2) \cdot \vec{r}] d^3 p_1 d^3 p_2, \quad (2.17)$$

in which $C(\vec{p}_1; \vec{p}_2) = \iint \tilde{J}_m(\vec{p}) \tilde{H}(\vec{p} + \vec{p}_1) \tilde{H}^*(\vec{p} + \vec{p}_2) d^3 p$ is the 3-D TCC that can be calculated by the overlap integral of three hemi-spherical shells as shown in Fig. 2.5.

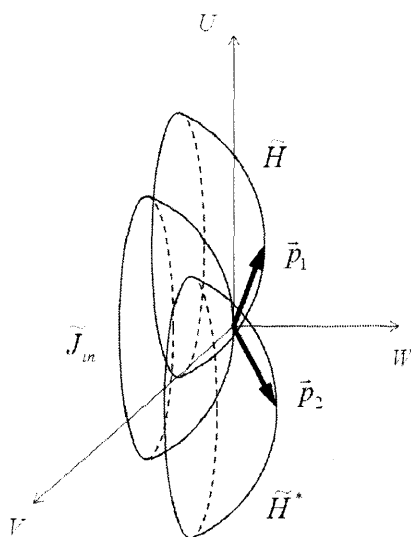


Figure 2.5. Graphical representation of the 3-D TCC under non-paraxial condition.

Streibl [26] derived expressions for the optical transfer, in a paraxial system, of a weak object (i.e. neglecting the bilinear terms) in the Born approximation. In Eqs. (26), (27) he described what he called the absorption and phase optical transfer functions. However, in our view this terminology is misleading, as these equations describe the spatial frequency content of the image, rather than the spatial frequencies of the object that are imaged, and therefore should not be considered as transfer functions. Thus his Figs. 3(a) and (b), for the coherent case, each show two Ewald spheres, implying that positive and negative axial spatial frequencies are imaged, whereas we know from the usual Ewald sphere construction that negative axial spatial frequencies only are imaged.

2.3. Simple Formula for 3-D Partially Coherent Imaging

In the previous section, we derived a non-paraxial model of 3-D partially coherent imaging, which can be summarized to Eq. (2.17). However, its calculation requires prohibitively large computation time for the 6-D integral of the TCC. In this section, we present a simple formula that can be calculated only by multiple applications of the 3-D fast Fourier transform (FFT).

As qualitatively described by Sheppard et al. [27], the 3-D non-paraxial TCC, $C(\bar{p}_1; \bar{p}_2)$ is the overlap integral of three hemi-spherical shells. Three shells can intersect in a surface, in a line, or at a point depending on the relative amount of shift, (\bar{p}_1, \bar{p}_2) . For example, for $\bar{p}_1 = \bar{p}_2 = (0,0,0)$, they overlap and collapse into one hemi-spherical shell centered at the origin. Then, the overlap integral is the area of the surface weighted by the modulated pupil functions. In another case, three shells can make a line intersection when two of them overlap while the third shifts with respect to the other two. In terms of the relative shift, the following combinations are possible: (i) $\bar{p}_1 \neq (0,0,0)$, $\bar{p}_2 = (0,0,0)$ (ii) $\bar{p}_1 = (0,0,0)$, $\bar{p}_2 \neq (0,0,0)$ (iii) $\bar{p}_1 = \bar{p}_2 \neq (0,0,0)$. The overlap integral in this case is the length of the intersecting line. Finally, three shells can intersect at a point or points. The combination of the relative shift to make the point intersection is more tricky, but, the overlap integral, which is the incremental volume of an intersecting point, is much smaller than the first two cases, line or surface contact. We discuss more about this at the end of this section. It is worthwhile to note that when $\bar{p}_1 = \bar{p}_2$, the integrand of Eq. (2.17) does not depend on the spatial coordinate, and its contribution is limited to the enhancement or degradation of the contrast. Hence, we merge these contributions into the background intensity.

To summarize, the 3-D non-paraxial TCC makes significant contribution to the image when $\bar{p}_1 \neq (0,0,0)$, $\bar{p}_2 = (0,0,0)$ or $\bar{p}_1 = (0,0,0)$, $\bar{p}_2 \neq (0,0,0)$. For these conditions, $C(\bar{p}_1; \bar{p}_2)$ can be written as follows:

$$C(\bar{p}_1; \vec{0}) = (P_{cond}^{3D} P_{obj}^{3D} * P_{obj}^{3D})(\bar{p}_1) \equiv C_1(\bar{p}_1), \quad (2.18)$$

$$C(\vec{0}; \bar{p}_2) = C(\bar{p}_2; \vec{0})^* = C_1(\bar{p}_2)^*, \quad (2.19)$$

where $P_{cond}^{3D}(\bar{p}) = |P_{cond}(u, v)|^2 \delta(|\bar{p}| - 1)$, $P_{obj}^{3D}(\bar{p}) = P_{obj}(u, v) \delta(|\bar{p}| - 1)$, $*$ is the 3-D autocorrelation defined as follows:

$$(f * g)(\bar{p}) \equiv \int f^*(\bar{q}) g(\bar{p} + \bar{q}) d^3 q. \quad (2.20)$$

In case of bright field imaging using the same numerical aperture for both objective and condenser lenses, Eq. (2.17) can be reduced to the autocorrelation of two uniform hemi-spherical shells (neglecting the aplanatic factor). It is same as the optical transfer function for high numerical aperture, which Sheppard et al. [23] has derived. In the current notation,

$$C_1(\vec{p}) = \frac{4}{\pi K} \arccos \left[\frac{1}{M} \left(\frac{2 \cos \alpha}{|w|} + 1 \right) \right], \quad (2.21)$$

in which $\vec{p} = (u, v, w)$, $M = \frac{2(u^2 + v^2)^{1/2}}{K|w|} \left(1 - \frac{K^2}{4} \right)^{1/2}$, and $K = (u^2 + v^2 + w^2)^{1/2}$.

However, most of the imaging modalities adopt various modulations for either condenser or objective pupil functions, or for both, so numerical computation of Eq. (2.18) is required. Substituting Eqs. (2.18-2.19) into Eq. (2.17), the overall image intensity can be simplified to

$$I_{img}(\vec{r}) \cong I_0 + 2 \operatorname{Re} \left[\alpha \int C_1(\vec{p}) \tilde{T}(\vec{p}) \exp[j2\pi(\vec{p} \cdot \vec{r})] d^3 p \right], \quad (2.22)$$

in which I_0 is the background intensity, $\alpha = \tilde{T}^*(\vec{0}) k_{res}^3$, k_{res} is the thickness of the Ewald sphere or the bandwidth of the incident light.

The integrals in the parenthesis are nothing more than inverse Fourier transforms, which can be efficiently calculated using the FFT algorithm [30].

$$I_{img}(\vec{r}) = I_0 + 2 \operatorname{Re} \left[\alpha F^{-1} \left\{ C_1(\vec{p}) \tilde{T}(\vec{p}) \right\} \right], \quad (2.23)$$

in which $\tilde{T}(\vec{p}) = F \left\{ 1 + i\pi(n_0^2 - n(\vec{r})^2) \right\}$, $C_1(\vec{p}) = (P_{cond}^{3D} P_{obj}^{3D} * P_{obj}^{3D})(\vec{p})$.

It is interesting to notice that the Eq. (2.23) has a similar form as the weak transfer function Sheppard et al. derived in the paraxial case. However, as shown in the form of the transmission function, Eq. (2.23) can be applied for a more general object within the first Born approximation.

Going back to the issue about relative strength of the point and the line intersection case, we compare the image intensity calculated by each of the two contributions. We perform a numerical simulation using a modified 3-D Shepp-Logan phantom, whose magnitude is adjusted to the refractive index of usual biological samples (1.35-1.37) [31]. Figure 2.6(b) and (c) show the horizontal and the vertical cross-section of the phantom, whose color represents the refractive index. Remember that we used the first Born approximation, which is valid when the overall phase delay across a sample is less than π . The phantom has a maximum phase delay around 2.5, so the first Born approximation is still applicable, although the Rytov approximation is usually preferred in biological samples [32].

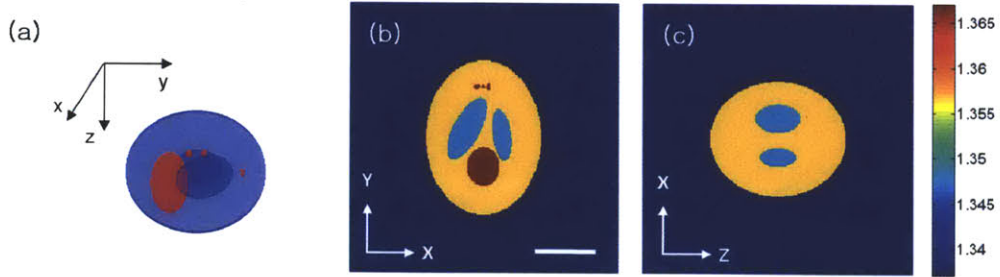


Figure 2.6. Modified 3-D Shepp-Logan phantom, the magnitude of which is adjusted to the refractive index of usual biological samples. (b) and (c) are the horizontal and the vertical cross-section, respectively. The scale bar is 5 μm .

For the calculation of the overlap integral, we consider the intersection of spheres instead of hemi-spheres of particular size, which simplifies the estimation. From geometry, three spheres can intersect in at least one point when the following condition is satisfied:

$$|\vec{p}_1 \cdot \vec{p}_2| |\vec{p}_1 - \vec{p}_2| \leq 2r |\vec{p}_1 \times \vec{p}_2|, \quad (2.24)$$

in which \vec{p}_1, \vec{p}_2 are vectors from the center of the first sphere to the centers of the other two, r is the radius of three spheres. The equality sign in Eq. (2.24) corresponds to intersection of the three spheres in a single point, whereas the $<$ sign corresponds to intersection in two points. In the case when the spatial coordinates are normalized by λ , the radius r becomes 1.

Neglecting the varying shapes of the intersecting volumes, Eq. (2.17) for the point intersection case may be approximated by

$$I_{img}(\vec{r}) \approx k_{res}^3 \sum_{\vec{p}_1} \tilde{T}(\vec{p}_1) \left\{ [C_{po\ int}(\vec{p}_1; \vec{p}_1 + \vec{p}) \tilde{T}^*(\vec{p}_1 + \vec{p}) \exp[i2\pi(\vec{p} \cdot \vec{r})]] \right\} d^3 p, \quad (2.25)$$

in which $C_{po\ int}(\vec{p}_1; \vec{p}_2) = 1$ for $\vec{p}_1, \vec{p}_2 (\neq \vec{p}_1 \text{ or } \vec{0})$ satisfying Eq. (2.24), and 0 otherwise.

$C_{po\ int}(\vec{p}_1; \vec{p}_2)$ is a function defined in a six-dimensional space, which is hard to visualize. Instead, Fig. 2.7 shows $C_{po\ int}(\vec{p}_1; \vec{p}_2)$ in a three-dimensional \vec{p}_2 space for various values of \vec{p}_1 . $C_{po\ int}(\vec{p}_1; \vec{p}_2)$ has 1 for \vec{p}_2 in the donut-shaped region that is shifted and deformed depending on the choice of \vec{p}_1 .

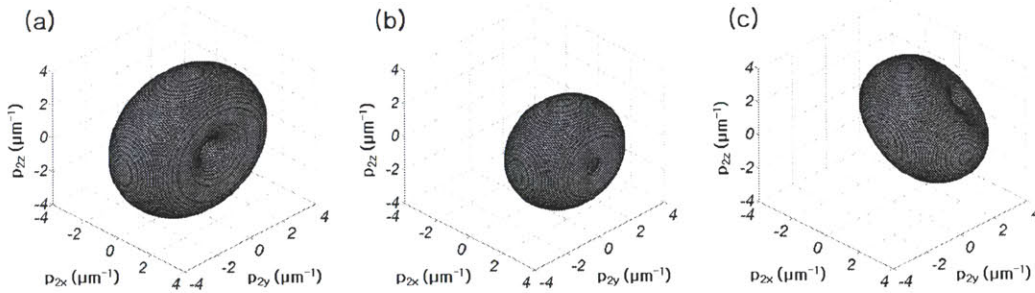


Figure 2.7. $C_{po\ int}(\vec{p}_1; \vec{p}_2)$ in \vec{p}_2 space for (a) $(p_{1x}, p_{1y}, p_{1z}) = (0.46, 0, 0)$, (b) $(p_{1x}, p_{1y}, p_{1z}) = (3.68, 0, 0)$, (c) $(p_{1x}, p_{1y}, p_{1z}) = (1.84, 1.84, 1.84)$. Unit of frequency is μm^{-1} .

Figure 2.8 compares horizontal cross-sections of the bright field image reconstructed using the line and the point intersection terms, Eq. (2.23) and Eq. (2.25) respectively. The intensity in Fig. 2.8(b) changes by less than 1% of Fig. 2.8(a), which justifies our neglect of the point intersection cases above. Although the

point intersection terms provide sharper boundaries, they are overwhelmed by the stronger, smeared out image by the line intersection terms in the bright field image.

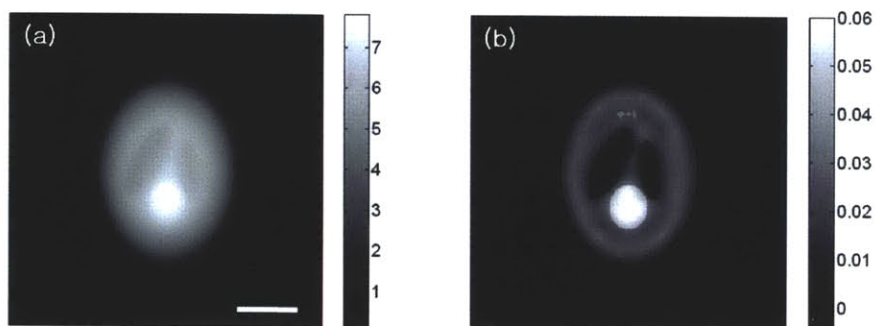


Figure 2.8. Horizontal cross-sections of bright field image reconstructed using (a) line, and (b) point intersection terms (after subtracting background). x is horizontal and y is vertical.

2.4. Application to Phase Contrast and Nomarski Differential Interference Contrast (DIC)

In this section, we test Eq. (2.23) to simulate various 3-D imaging techniques using partially coherent light. Changing the condenser and the objective pupils, Eq. (2.23) can be used to simulate various imaging modalities. More specifically, in this section we simulate phase contrast and Nomarski differential interference contrast (DIC), and compare them with bright field imaging without any modulation. Figure 2.9 shows the 2-D pupil functions for the condenser and the objective lens used for phase contrast. The 3-D pupil functions used in Eq. (2.23) are calculated by projecting the 2-D functions onto the Ewald sphere. The condenser pupil is transparent over a limited portion with a ring shape, while the objective lens provides $\pi/2$ phase retardation and 80% absorption of the field through the ring colored as a light blue region in Fig. 2.9(b).

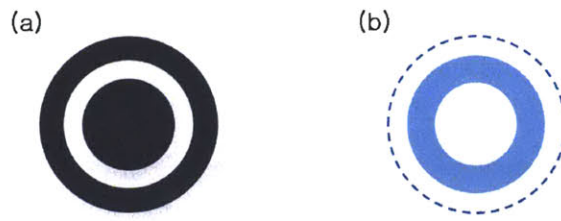


Figure 2.9. 2-D pupil functions used for the calculation of the phase contrast in Fig. 6(b), (e): (a) condenser (b) objective pupil function. The 3-D pupil function is calculated by projecting the 2-D pupil function onto the Ewald sphere. Dark grey region in (a) is opaque, and light blue region in (b) induces phase retardation with some absorption of transmitted light.

In case of the Nomarski DIC, there is no modulation in the pupil functions. Instead, two beams shifted by a Wollaston prism pass through a sample and then interfere after being merged by another Wollaston prism as shown in Fig. 2.10 [8]. The self-interference without any blocking pupils enables the imaging of a transparent sample with higher resolution and better sectioning capability. In terms of the image formation model, most of the works are for 2-D [33-35]. Preza et al. [35] suggested a 3-D model, which is an extension of their 2-D model based on the defocused point spread function.

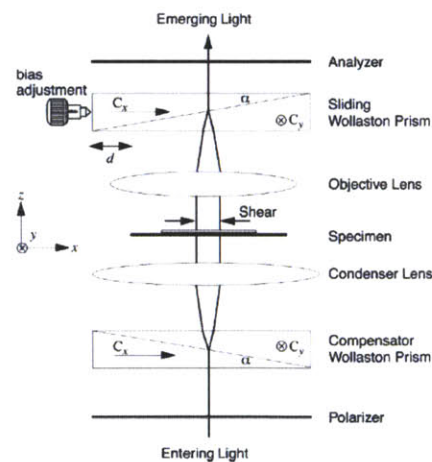


Figure 2.10. Schematic of a DIC microscope with two typical Wollaston prisms [20].

However, as Mehta et al. [34] pointed out, their model is closer to what he calls Kohler-DIC (a system with no Wollaston prism in the input arm), which may be used for Nomarski-DIC for condenser apertures

smaller than around 0.4 times the objective aperture. We show that the 3-D non-paraxial TCC derived in the previous section can be used to analyze Nomarski-DIC in a more efficient and rigorous way.

As briefly mentioned, Nomarski-DIC uses the self-interference of two beams passing through a slightly different regions of a sample. In the TCC approach, it can be described by rewriting the transmission function as follows:

$$T_N(\vec{r}) = T(\vec{r} + \Delta\vec{e}_\Delta)\exp(-i\phi) + T(\vec{r} - \Delta\vec{e}_\Delta)\exp(i\phi), \quad (2.26)$$

where \vec{e}_Δ is a unit vector in the shearing direction, 2Δ is the amount of shift, 2ϕ is the bias.

For convenience, let us define the X axis as the shearing direction without loss of generality. The Fourier transform of the transmission function can be written as

$$\tilde{T}_N(\vec{p}) = 2\tilde{T}(\vec{p})\cos(2\pi m\Delta - \phi). \quad (2.27)$$

Substituting into Eq. (2.22),

$$I_N(\vec{r}) = I_0 + 2\operatorname{Re}\left[\alpha F^{-1}\left\{C_N(\vec{p})\tilde{T}(\vec{p})\right\}\right], \quad (2.28)$$

in which $C_N(\vec{p}) \equiv 2\cos(2\pi m\Delta - \phi)C_1(\vec{p})$ is the effective transfer function for the Nomarski-DIC.

Figure 2.11 shows images calculated by simulating bright field, phase contrast, and Nomarski-DIC using the method described above. The sample in the simulation has a real refractive index, so it is transparent under bright field. Vague boundaries of the phantom in Fig. 2.11(a) and (d) are due to the second order interaction of scattered light from the sample. Figure 2.11(b) and (e) present the horizontal and the vertical cross-section of the phase contrast image using the condenser and the objective pupil in Fig. 2.10. External and internal boundaries of the phantom are clearly visible now. The halo around the phantom is one of the main features of the phase contrast. Figure 2.11(c) and (f) present the cross-sections of the

Nomarski-DIC image. Using wider numerical apertures, it provides better resolution and optical sectioning. It does not contain the halo artifact either.

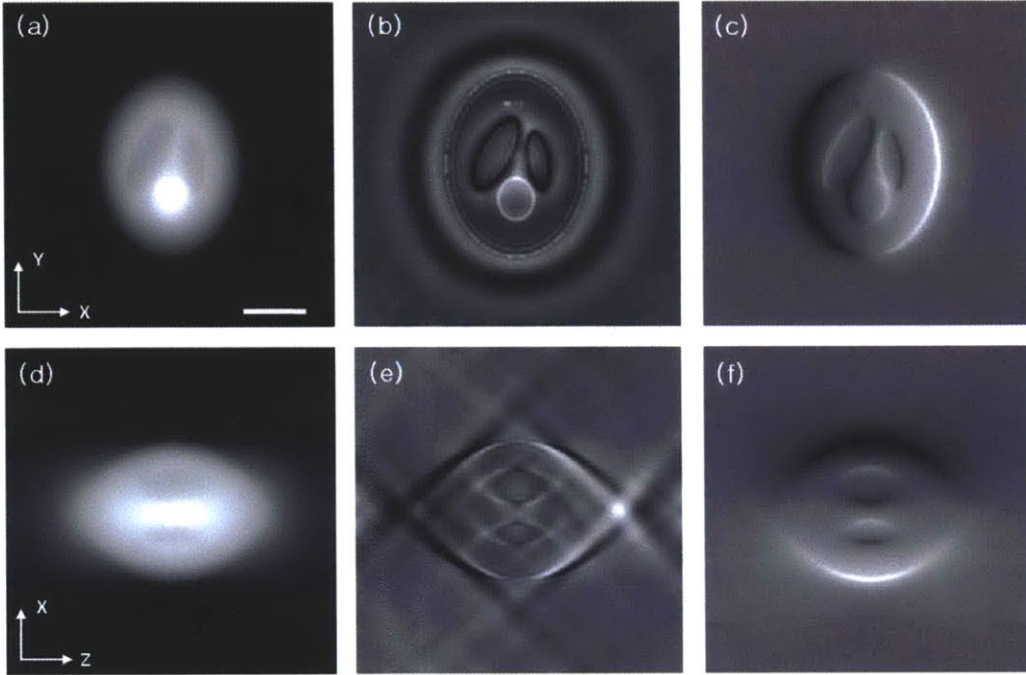


Figure 2.11. Comparison of cross-sections imaged by (a),(d) bright field, (b),(e) phase contrast and (c),(f) Nomarski DIC. (a),(b),(c) are horizontal cross-sections, (d),(e),(f) are vertical cross-sections. For phase contrast, the condenser and the objective pupil functions in Fig. 2 are used. For Nomarski-DIC, shearing is given in X direction with $2\Delta = \lambda/4NA$, $2\phi = \pi/2$. The optical axis is in Z direction and the scale bar is $5 \mu\text{m}$.

The benefit of the TCC approach is to get insight about the frequency response of an imaging system. Figure 2.12 shows cross-sections of the effective transfer function for the Nomarski DIC, which was defined in Eq. (2.28). Since it uses the full aperture, the frequency support is the same as for bright field imaging. However, for the visualization of a transparent sample, it modulates the frequency spectrum asymmetrically in the shearing direction. Hence, some features whose frequency spectrum falls in the low transmission region may not be imaged for this setting of parameters. Finally, Kohler-DIC can be simulated using the effective transfer function that can be written as

$$C_K(\vec{p}) = (P_{cond}^{3D} P_K^{3D} * P_K^{3D})(\vec{p}), \quad (2.29)$$

in which $P_K^{3D}(\vec{p}) = 2 \cos(2\pi m \Delta - \phi) P_{obj}^{3D}(\vec{p})$.

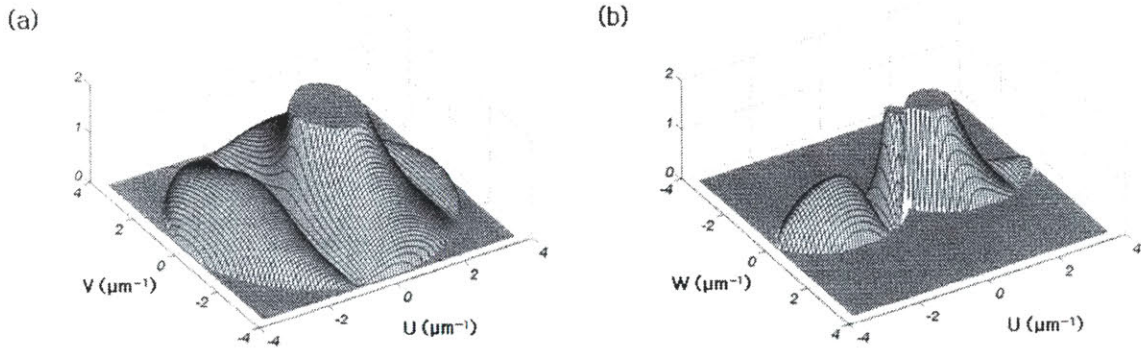


Figure 2.12. Cross-sections of the effective transfer function for Nomarski DIC ($2\Delta = \lambda/4NA$, $2\phi = \pi/2$): (a) U - V cross-section, (b) U - W cross-section. (U, V, W) is the spatial frequency corresponding to the spatial coordinate (X, Y, Z) , in which X is the shearing direction and Z is the optical axis.

Chapter 3

3-D Refractive Index Imaging by Quantitative Phase Measurement

3.1. Tomographic Phase Microscopy (TPM)

3.1.1. Quantitative Phase Imaging

Quantitative phase imaging involves measuring the phase delay of an optical beam, induced by a sample with a different refractive index from background medium. In the optical regime, the measurement of the relative phase difference is not trivial because of the high frequency of light, 10^{15} Hz. One way to do it is to measure the irradiance at multiple planes and retrieve the phase distribution by solving the transport of intensity equation [36, 37]. It works well with both coherent and non-coherent illumination, and is free from the phase unwrapping problem [38]. On the other hand, various interference-based methods have been suggested and widely used in the biomedical microscopy because of their high speed and high sensitivity capability [9-11]. The interference-based methods use a reference beam to modulate a sample beam and extract phase information out of it. Depending on the way of modulation, they can be largely divided into temporal and spatial modulation techniques.

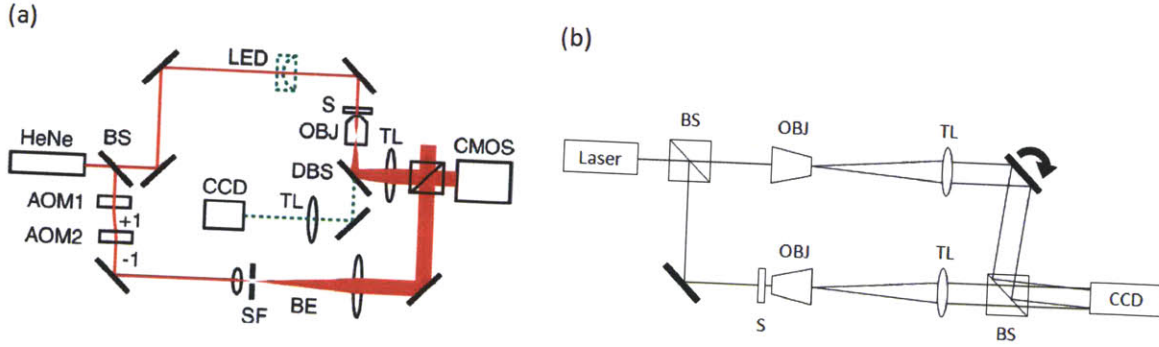


Figure 3.1. Examples of quantitative phase measurement techniques (a) Heterodyne Mach-Zehnder phase microscopy, (b) Hilbert phase microscopy. S, sample; BS, beam splitter; DBS, dichroic beam splitter; TL, tube lenses; AOM1,2, acousto-optic modulators; BE, beam expander; SF, spatial filter.

Figure 3.1 compares the Heterodyne Mach-Zehnder phase microscopy and the Hilbert phase microscopy, which adopt the temporal and the spatial modulation techniques, respectively. In the temporal modulation technique, the phase of the reference beam is shifted stepwise with respect to the sample beam. The phase shifting can be achieved either by moving a reference mirror mounted on a piezoelectric modulator [11] or by shifting the frequency of a reference beam using an acousto-optic modulator [10]. In the phase shifting interferometry adopting the temporal modulation technique, four intensity images are taken while the phase of the reference beam is shifted by $\pi/2$ each time of measurement. The sample-induced phase delay $\Delta\varphi(x, y)$ can be calculated by:

$$\Delta\varphi(x, y) = \text{Arg} \left((I_{3\pi/2} - I_{\pi/2}) + i(I_{2\pi} - I_{\pi}) \right), \quad (3.1)$$

where $I_{n\pi/2} = I_S(x, y) + I_R + 2\sqrt{I_S(x, y)I_R} \cos(\Delta\varphi(x, y) + n\pi/2)$ is the irradiance of the interferogram taken at the image plane and at different time points, $I_S(x, y)$ and I_R are the irradiances of the sample and reference fields, respectively, and $n = 1, 2, 3, 4$.

In the spatial modulation technique [9], the sample beam is modulated by slightly tilting the reference beam, by which the sample and the reference beam meet with an angle at the image plane. Figure 3.2(a)

shows a raw interferogram image, which was recorded in the Hilbert phase microscopy adopting the spatial modulation technique. The irradiance at the image plane can be written as:

$$I(x, y) = I_S(x, y) + I_R + 2\sqrt{I_S(x, y)I_R} \cos(2\pi qx - \Delta\varphi(x, y)), \quad (3.2)$$

where $I_S(x, y)$, I_R are the irradiances of the sample and reference fields, respectively, $\Delta\varphi(x, y)$ is the sample-induced phase delay, and q is the spatial frequency of the fringes in the raw interferogram image.

Figure 3.2(b) depicts the magnitude of the Fourier transform of Eq. (3.2) on a logarithmic scale. It is important to note the ± 1 st order components that contain sample information can be separated from the 0th order due to the spatial modulation. The sample induced phase delay can be calculated by moving the +1st order component to the origin of the frequency coordinates and taking the inverse Fourier transform. More specifically, the +1st order component can be written as

$$\hat{I}_{+1st}(u, v) = \int \sqrt{I_S(x, y)I_R} e^{j(2\pi qx - \Delta\varphi(x, y))} e^{-j2\pi(ux + vy)} dx dy = \hat{\Phi}(u - q, v), \quad (3.3)$$

where $\hat{\Phi}(u, v)$ is the Fourier transform of $\Phi(x, y) = \sqrt{I_S(x, y)I_R} e^{-j\Delta\varphi(x, y)}$, and the sample-induced phase delay $-\Delta\varphi(x, y)$ is the argument of the complex variable $\Phi(x, y)$. The dotted circles in Fig. 3.2(b) indicate the spatial frequency range determined by the numerical aperture of the system. Their radius in the image can be adjusted by changing the magnification. The distance between the 0th and the ± 1 st order is q , the spatial frequency of the fringes in the raw interferogram image. By choosing q to be twice of the numerical aperture, it is possible to obtain a phase image with the diffraction-limited resolution even after the resolution loss due to the spatial modulation.

The spatial modulation technique uses only one interferogram to retrieve one phase image, so the speed of phase retrieval is four times faster than the temporal modulation technique. Recording the sample-induced phase delay by utilizing a reference beam which is slightly tilted with respect to the sample beam is quite similar to the idea of the off-axis holography, hence the spatial modulation technique is called digital off-

axis holography. The use of the term “digital” means that the demodulation is done numerically instead of using reconstruction illumination. Figure 3.2(c) is the phase image of a HeLa cell, which was measured by the Hilbert phase microscopy and the method described above.

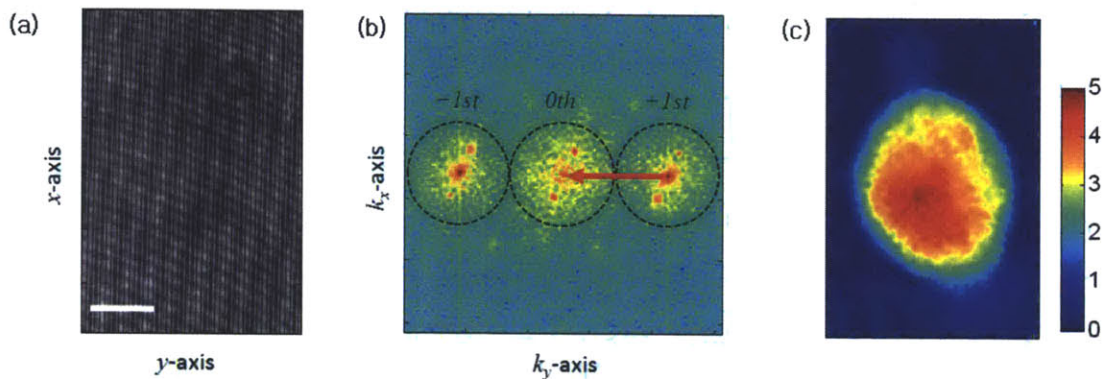


Figure 3.2. Data processing for Hilbert phase microscopy: (a) raw interferogram image, (b) Fourier transform of (a), (c) phase image obtained from (b). Scale bar, 5 μm .

3.1.2. Tomographic Reconstruction of 3-D Refractive Index Map

Tomographic phase microscopy (TPM) is a technique that our group has uniquely developed that combines the quantitative phase imaging techniques with a tomographic method for 3-D reconstruction. More specifically, TPM collects quantitative phase images for multiple sample angles of illumination and then combines the information to numerically reconstruct the 3-D refractive index map of the sample. For the phase-image acquisition, TPM can adopt either the temporal or the spatial modulation technique. Figures 3.3(a) and (b) show TPM based on the Heterodyne Mach–Zehnder phase microscopy [39] and the Hilbert phase microscopy [40], respectively.

Using TPM, Choi et al. imaged the 3-D internal structure of live biological samples with unprecedented resolution without adding any contrast agent. They showed that the refractive index of the nucleus ($n = 1.355\text{--}1.365$), apart from the nucleolus, is smaller than some parts of the cytoplasm ($n = 1.36\text{--}1.39$). They also showed that the increased scattering associated with acetal whitening results from both

increased refractive index contrast between nucleoli and the rest of the cell, and increased heterogeneity of refractive index throughout the cell. Park et al. [41] applied TPM to study the disease states of malaria-infected red blood cells; the refractive index map showed morphological alterations of host RBCs and the change in the hemoglobin concentration of cytoplasm during developmental stages. TPM has been applied to determine the thickness of ultra-thin (up to 60nm) specimen such as helical ribbons that form in cholesterol-surfactant mixtures [42]. Using this capability, Khaykovich et al. have discovered a quadratic relationship between the radius and the thickness of the helical ribbons, which shows the helical form is determined by relatively weak spontaneous bending forces arising from chirality of cholesterol molecules balanced by equally weak bending elasticity of a very thin solid band.

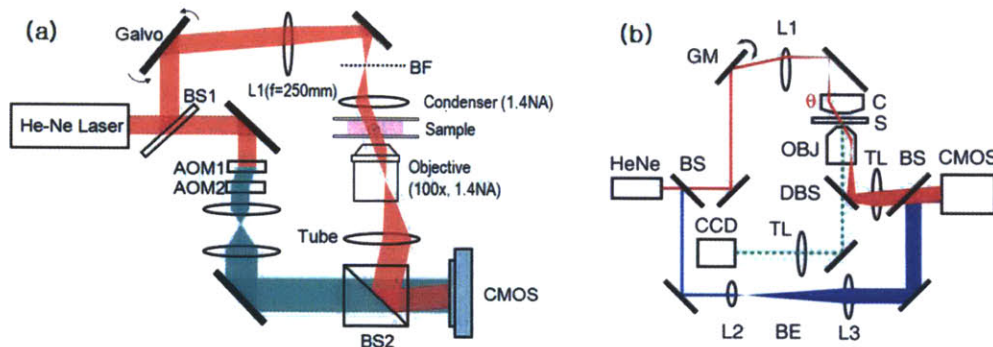


Figure 3.3. Tomographic phase microscopy. BS, beam splitters; GM, galvanometer scanning mirror; L1, focal length $f \approx 250$ -mm lens; BF, back focal plane of condenser lens. In Fig. 3.3(a), the sample laser beam with original laser frequency is shown in red, and the frequency-shifted reference laser beam is shown in blue. C, condenser lens; θ , beam tilt angle; S, sample; OBJ, objective lens; DBS, dichroic beam splitter; BE, beam expander; TL, tube lenses.

There are two ways to change the relative angle of illumination with respect to the specimen. One is to rotate the sample with the illumination beam fixed, and the other is to rotate the illumination beam with the sample fixed. Rotating the sample makes it possible to cover the entire angular range, and thus obtain the same axial resolution as the transverse resolution. But it is difficult to fix the axis of rotation, and rotation inevitably perturbs the sample. In addition, data acquisition speed is limited due to the use of mechanical rotation of the sample. Therefore, the use of sample rotation is typically restricted to solid

non-biological objects such as optical fibers [43, 44]. Special sample preparation is required for imaging biological cells [45]. On the other hand, the rotating beam approach doesn't perturb the sample during data acquisition, and is thus suitable for imaging live cells in their native state [39, 46]. Data acquisition can be fast enough to study the dynamics of the live cells. Only small modifications are needed for the instrument to fit into a conventional high NA optical microscope.

The numerical reconstruction of the 3-D refractive index map from the 2-D phase images can be done in various ways. The original TPM adopted a filtered back-projection algorithm which is based on the inverse Radon transform [39]. The inverse Radon transform reconstructs an image from its projections along various directions under the assumption that the light propagates rectilinearly within a sample [47]. The so-called projection assumption is not valid when a sample contains the internal structures at the same length scale as the wavelength of an incident beam. This is because such small structures can diffract the incident beam and the beam path is no longer rectilinear. In the optical imaging of biological samples, internal organelles such as nucleoli, mitochondria, lipid droplets, etc. can diffract the light. Hence, the tomogram reconstructed by the filtered back-projection algorithm will contain a ring-shaped artifact, which is the diffraction pattern of the small organelles located at the other heights than the focal plane. To remove such an artifact, diffraction needs to be included in the reconstruction process, using a technique known as diffraction tomography.

3.2. Optical Diffraction Tomography

Reproduced in part with permission from Yongjin Sung, Wonshik Choi, Christopher Fang-Yen, Kamran Badizadegan, Ramachandra R. Dasari, and Michael S. Feld, "Optical diffraction tomography for high resolution live cell imaging," *Opt. Express* 17, 266-277 (2009).

3.2.1. Fourier Diffraction Theorem

Using the Born approximation, Wolf derived a formulation which enables reconstruction of a 3-D object from 2-D measured E-fields [29]. With scalar field assumption, the propagation of light field, $U(\vec{R})$, through the medium, can be described by the wave equation as follows:

$$\nabla^2 U(\vec{R}) + k_0^2 n^2 U(\vec{R}) = 0. \quad (3.4)$$

Here, $k_0 = 2\pi/\lambda_0$ is the wave number in the free space with λ_0 the wavelength in the free space, and $n(\vec{R})$ is the complex refractive index. If the field is decomposed into the incident field $U^{(I)}(\vec{R})$ and scattered field $U^{(S)}(\vec{R})$,

$$U(\vec{R}) = U^{(I)}(\vec{R}) + U^{(S)}(\vec{R}), \quad (3.5)$$

then, the wave equation becomes

$$(\nabla^2 + k_0^2) U^{(S)}(\vec{R}) = f(\vec{R}) U(\vec{R}), \quad (3.6)$$

with $f(\vec{R}) = -(2\pi/\lambda_m)^2 ((n(\vec{R})/n_m)^2 - 1)$, and n_m is the refractive index of the medium. $f(\vec{R})$ is known as the object function. Based on Green's theorem, the formal solution to Eq. (3.6) can be written as

$$U^{(S)}(\vec{R}) = - \int G(|\vec{R} - \vec{R}'|) f(\vec{R}') U(\vec{R}') d^3 \vec{R}', \quad (3.7)$$

with $G(r) = \exp(ik_0 r) / (4\pi r)$ the Green's function. Since the integrand contains the unknown variable, $U(\vec{R})$, we employ an approximation to obtain a closed form solution for $U^{(S)}(\vec{R})$. The first Born approximation is the simplest we can introduce when the scattered field is much weaker than the incident field ($U^{(S)} \ll U^{(I)}$), in which case the scattered field is given by the following equation:

$$U^{(S)}(\vec{R}) = - \int G(|\vec{R} - \vec{R}'|) f(\vec{R}') U^{(I)}(\vec{R}') d^3 \vec{R}'. \quad (3.8)$$

This approximation provides a linear relation between the object function $f(\vec{R})$ and the scattered field $U^{(S)}(\vec{R})$. By taking Fourier transform of both sides of Eq. (3.8), we obtain the following relation, known as the Fourier diffraction theorem:

$$\hat{f}(K_x, K_y, K_z) = \frac{ik_z}{\pi} \hat{U}^{(S)}(k_x, k_y; z^+ = 0). \quad (3.9)$$

Here, \hat{f} and $\hat{U}^{(S)}$ are the 3-D and 2-D Fourier transform of f and $U^{(S)}$, respectively; k_x and k_y are the spatial frequencies corresponding to the spatial coordinate x and y in the transverse image plane, respectively; $z^+ = 0$ is the axial coordinate of the detector plane, which is the plane of objective focus in the experiment. (K_x, K_y, K_z) , the spatial frequencies in the object frame, define the spatial frequency vector of (k_x, k_y, k_z) relative to the spatial frequency vector of the incident beam (k_{x0}, k_{y0}, k_{z0}) , and k_z is determined by the relation $k_z = \sqrt{k_0^2 - k_x^2 - k_y^2}$. For each illumination angle, the incident wave vector changes, and so does (K_x, K_y, K_z) . As a result, we can map different regions of the 3-D frequency spectrum of the object function $f(\vec{R})$ with various 2-D angular complex E-field images. After completing the mapping, we can take the inverse Fourier transform of \hat{f} to get the 3-D distribution of the complex refractive index.

3.2.2. Data Acquisition and Processing

For experimental demonstration, a series of 2-D phase images were collected using TPM adopting temporal modulation technique. A He-Ne laser beam of wavelength 633 nm was divided into sample and reference beams. The propagation direction of the sample beam was controlled by a galvanometer mirror and the sample image of the transmitted beam was delivered to the camera by an objective and a tube lenses. Two acousto-optic modulators were used to shift the frequency of the reference beam by 1.25 kHz, and the frame rate of a CMOS camera (Photron 1024PCI) was adjusted to take images with 200 μ s intervals. For each angle of illumination, four successive interferogram images were recorded within 800 μ s and phase-shifting interferometry was used to produce a pair of quantitative phase and amplitude images. To maximize the range of illumination angles, a high NA condenser (Nikon, 1.4 NA) and objective lens (Olympus UPLSAPO, 1.4 NA) were used. The sample beam was rotated using a galvanometer mirror to cover from -70 to 70 degrees in 0.23 degree steps. It takes about 10 seconds to record a set of angular complex E-field images.

Using the set of phase and amplitude images taken at various angles of illumination, we applied diffraction tomography algorithm described in section 3.2.1. Given a quantitative phase image $\varphi(x, y; \theta)$ and an amplitude image $A(x, y; \theta)$ taken at each illumination angle, θ , we can reconstruct the total E-field, $U(x, y; \theta) = A(x, y; \theta)e^{i\varphi(x, y; \theta)}$, at the image plane. The measured field image is composed of the phase change induced by the sample and the phase ramp introduced by the tilted illumination. A corresponding set of images $U_{bg}(x, y; \theta) = A_{bg}(x, y; \theta)e^{ik_{x0}x + ik_{y0}y}$ taken when no sample is present provides the background field, which can be considered as the incident fields. Figure 3.4(a) shows the phase image $\varphi(x, y; \theta = 0)$ of a 6 μm polystyrene bead (Polysciences. Inc.) taken at zero incidence angle. Figure 3.4(b) shows the typical amplitude image of $\hat{U}(k_x, k_y; \theta)$ on a logarithmic scale.

To apply the Fourier diffraction theorem, we convert (k_x, k_y) on the right hand side into (K_x, K_y) as follows.

$$\hat{f}(K_x, K_y, K_z) = \frac{i(K_z + k_{z0})}{\pi} \hat{U}^{(S)}(K_x + k_{x0}, K_y + k_{y0}; z^+ = 0). \quad (3.10)$$

We first calculate $\hat{U}^{(S)}(k_x, k_y; \theta)$ from measured complex fields, and then shift them by $(-k_{x0}, -k_{y0})$ in spatial frequency space. Or equivalently, we can divide the scattered fields by the incident field $U_{bg}(x, y; \theta)$, which is equivalent to shifting them in Fourier space.

$$\hat{U}^{(S)}(K_x + k_{x0}, K_y + k_{y0}; \theta) = (U(x, y; \theta) - U_{bg}(x, y; \theta)) / U_{bg}(x, y; \theta). \quad (3.11)$$

Figures 3.4(c)-(d) show the results of this mapping on the $(K_x, K_y, K_z=0)$ and $(K_x, K_y=0, K_z)$ planes, respectively. The data along the blue line in Fig. 3.4(b) is mapped onto the blue half-circle on the (K_x, K_z) space of Fig. 3.4(d). Different angular images are mapped onto different spaces such that they eventually cover a significant portion of the (K_x, K_y, K_z) space of the object function $f(\vec{R})$. Looking at the frequency spectrum of Figs. 3.4(c)-(d), ring patterns are clearly visible after mapping various angular images, which is expected for the spherical shape of the sample. By taking the inverse Fourier transform of the entire 3D frequency spectrum, we obtain the 3D distribution of refractive index of the object.

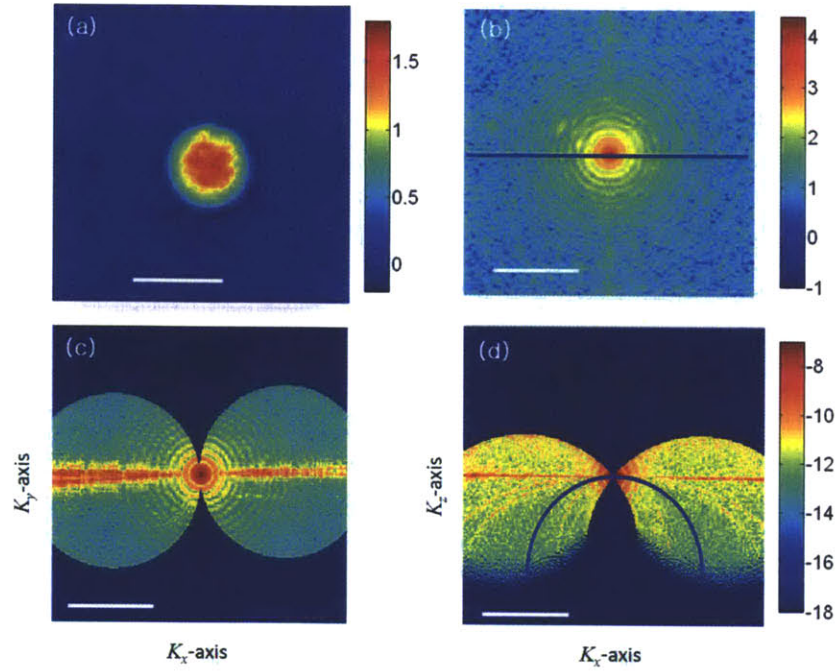


Figure 3.4. Mapping of the complex E-field onto the 3D Fourier space of the object function. (a) Quantitative phase image of a 6 μm polystyrene bead at zero degree illumination. The color bar indicates phase in radians. Scale bar, 5 μm . (b) Amplitude of the Fourier transform of the complex E-field image at zero degree illumination on a logarithmic scale. (c) Amplitude distribution in K_x - K_y plane after mapping all the angular E-field images. (d) Amplitude distribution in the K_x - K_z plane. The color bar indicates base-10 logarithm of the amplitude of E-field. The scale bars in (b-d) indicate $2 \mu\text{m}^{-1}$.

With our current configuration, we could get an image within illumination angles of up to ± 70 degrees which was measured via the spatial frequency of the fringe pattern at the image plane. As a result, we could not fill the entire region of frequency space, as can be seen in Figs. 3.5(c)-(d). In other words, the inverse problem is underdetermined. In our first round of reconstruction, we put zero values in the missing angle space. The reconstructed object function then exhibits negative bias around the sample and the refractive index is smaller than the actual value (Fig. 3.5(a)). To minimize the artifact introduced by the missing angles, we applied an iterative constraint algorithm [48, 49] based on the prior knowledge that the object function is nonnegative for the live cells. The index throughout the field of view, either inside or outside of the cell, is at least the same or higher than the medium. We first take the inverse Fourier transform of the originally mapped data with zero values for the missing space (Fig. 3.5(d)).

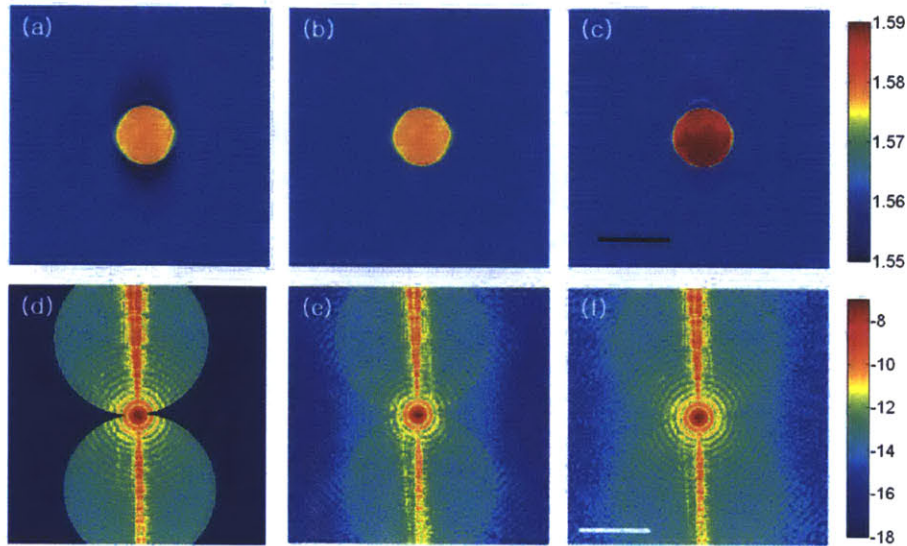


Figure 3.5. Iterative constraint algorithm. (a) Slice image of a 6 μm bead before application of the constraint algorithm. (b) Same slice image as in (a) after application of the non-negative constraint. (c) Same slice image as in (b) after 100 iterations. The color bar indicates the refractive indices at 633 nm wavelength. The scale bar, 5 μm . (d) Amplitude distribution in K_x - K_y plane before application of the constraint algorithm. (e) 3D Fourier transform of tomogram after non-negative constraint. (f) 3D Fourier transform of tomogram after 100 iterations. The color bar indicates base-10 logarithm of E-field amplitude. Scale bar, 2 μm^{-1} .

In the reconstructed image there are pixels whose index values are smaller than index of the medium (Fig. 3.5(a)). We forced these to be the same as the index of the medium and take the Fourier transform. The index values in the Fourier space in which we put zero values are no longer zero, and we obtain an approximate solution for the missing angles (Fig. 3.5(e)). But, at the same time, the data in the space which contains measured data is now modified. Since the experimentally measured data is accurate, we replace the modified data with the measured data. We iterate this procedure until the reconstructed object function converges (Fig. 3.5(c)-(f)). As a result, the negative bias is removed and the reconstructed image becomes more accurate. For the case of the polystyrene bead, we estimate that the accuracy of the measured refractive index is close to 0.001 after application of the iterative constraint algorithm. When the Fourier maps before (Fig. 3.5(d)) and after (Fig. 3.5(f)) iteration are compared, the ring patterns are generated in the missing angle regions (Fig.3.5(f)). This indicates that iterative constraint algorithm can

generate reasonably accurate solutions for the missing angle regions. The approach to use *a priori* information about a sample to compensate for the incomplete data is called the regularization. The regularization of 'rotating-beam' optical diffraction tomography will be handled more extensively in Chapter 5.

3.2.3. Born vs. Rytov Approximation

Numerical simulations have demonstrated that the Born approximation is valid when the total phase delay of the E-field induced by the specimen is less than $\pi/2$ [47]. The thickness of single biological cells is typically about 10 μm , with index difference with respect to the medium about 0.03. Thus, the phase delay induced by typical cells is approximately π at a source wavelength of $\lambda = 633 \text{ nm}$. Therefore, one would not expect the Born approximation to be valid for imaging biological cells.

We note that the Rytov approximation is more relevant to imaging biological cells than the Born approximation. It is not sensitive to the size of the sample or the total phase delay, but rather to the *gradient* of the refractive index. Specifically, the Rytov approximation is valid when the following condition is satisfied:

$$n_\delta \gg \left(\nabla \varphi^{(s)} \frac{\lambda}{2\pi} \right)^2, \text{ with } \varphi^{(s)} = \ln \left(\frac{U(\vec{R})}{U^{(i)}(\vec{R})} \right), \quad (3.12)$$

and n_δ is the index variation in the sample over the length scale of wavelength. This condition basically asserts that the Rytov approximation is independent of the specimen size and only limited by the phase gradient $\nabla \varphi^{(s)}$. For a weakly scattering sample such as biological cell, the phase change $\nabla \varphi^{(s)}$ is linearly proportional to n_δ to a first approximation, such that the relation is valid when $n_\delta \ll 1$. According to our previous work [39], the index variation n_δ is in the range of 0.03 - 0.04 for biological cells. As shown in the section 3.2.4, we obtain a high quality image of a live cell when we use the Rytov approximation, while the Born approximation leads to significant distortions in the reconstructed image.

As suggested by Devaney [50], the implementation of the Rytov approximation in the Fourier diffraction theorem requires a slightly different approach. Following Devaney's method, we introduce the complex phase $\phi(\vec{R})$, defined by $U(\vec{R}) = e^{\phi(\vec{R})}$, and substitute this into the wave equation (Eq. (3.4)). After applying the approximation of Eq. (3.12), we again obtain the Fourier diffraction theorem Eq. (3.9), but with $U^{(S)}$ replaced by $U_{Rytov}^{(S)}$ defined as

$$U_{Rytov}^{(S)} = U^{(I)}(\vec{R}) \ln \left(\frac{U(\vec{R})}{U^{(I)}(\vec{R})} \right). \quad (3.13)$$

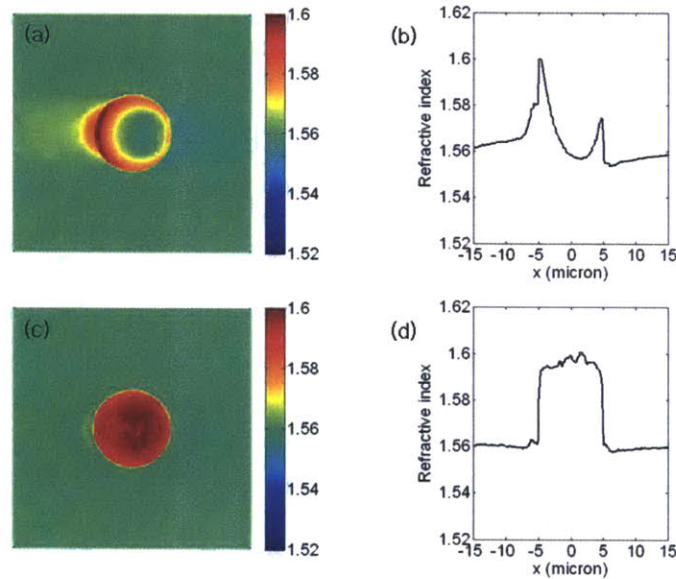


Figure 3.6. Comparison of the Born and Rytov approximations in diffraction tomography. (a) and (c): Slice images of a 10 μm bead reconstructed based on the Born and Rytov approximations, respectively. (b) and (d): Line profiles across the center of the bead. The color bar indicates refractive indices at 633 nm wavelength.

Figure 3.6 shows the slice images of a 10 μm bead reconstructed from the Born and Rytov approximations, respectively. Line profiles across the center of the bead are presented next to the slice images. The index in the middle of the bead is lower for the Born approximation while it is relatively uniform for the Rytov approximation. This demonstrates that the validity of the Born approximation is highly dependent on the size of the object and is not suitable at all for the 10 μm polystyrene bead in oil,

whose phase delay is close to 3 radians. On the other hand, the Rytov approximation is less affected by the object size and valid for the index difference of 0.03. A biological cell typically induces similar phase delay as a 10 μm bead. Thus the Rytov approximation will be appropriate for imaging biological cells.

3.2.4. Comparison with Inverse Radon Approach

To test the performance of the 3D reconstruction methods, we first obtained two sets of angular E-field images of 6 μm polystyrene beads (Polysciences) immersed in oil (Cargille, $n=1.56$) at two different foci, one in the middle of the bead and the other 4 μm above the center. When we applied the filtered back-projection algorithm based on the projection approximation, the slice image at the middle of the bead was uniform when the objective focus was set to the middle of the bead (Fig. 3.7(a)). However, when the focus was above center, the slice image in the middle of the bead presented ring patterns (Fig. 3.7(b)), which are due to diffraction of the propagating beam.

We applied diffraction tomography based on the Rytov approximation. The resulting slice images of tomograms are shown in Figs. 3.7(c) and (d) at the objective focus in the middle of the bead and 4 μm above the center of the bead, respectively. Both images show clear boundaries of the bead with uniform index distributions. This indicates that the diffraction tomography properly accounts for the effects of diffraction. Note that the index of the bead relative to that of the oil was set to 0.03. This difference is very close to the relative index of the cell to the culture medium. Hence, we expect the Rytov approximation to be applicable to imaging of single cells. Based on the analysis of the slope at the edge of the bead, the spatial resolution of the reconstructed image was estimated to be 0.35 μm in the transverse and 0.7 μm in the axial direction.

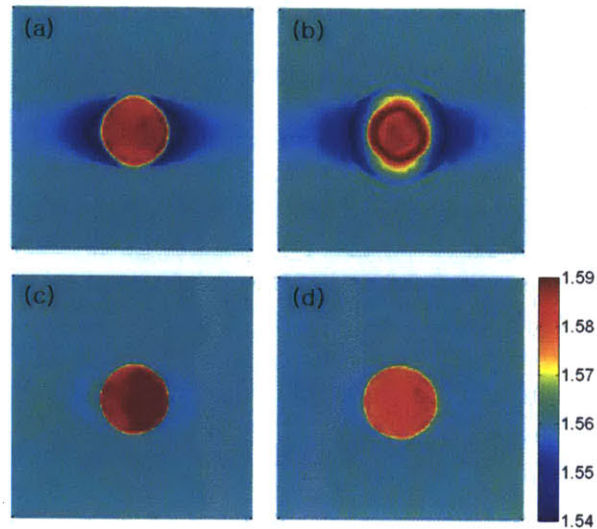


Figure 3.7. Comparison between filtered back-projection algorithm and diffraction tomography with the Rytov approximation. (a) and (b): Slice images of tomogram in the middle of a 6 μm bead reconstructed by the filtered back-projection algorithm when the objective focus is in the middle of the bead (a) and 4 μm above the center of the bead (b). (c) and (d): Same slice images as (a) and (b) after reconstructed by the diffraction tomography based on the Rytov approximation at objective focus in the middle of the bead (c) and 4 μm above the center of the bead (d). The color bar indicates refractive indices at 633 nm wavelength.

We imaged live HT-29 cells, a human colon adenocarcinoma cell line. Cells were prepared in an imaging chamber specially designed for the imaging of a live cell. It is composed of two coverslips separated by a 125 μm thick plastic spacer. Cells were incubated at 37 $^{\circ}\text{C}$ for 12 hours before the measurements such that they become fully attached to the coverslip surface. For a fixed objective focus, we took a set of angular complex E-field images and applied both filtered back-projection algorithm and diffraction tomography based on the Rytov approximations.

Figures 3.8(e)-(g) are x - y slices of tomogram images processed by the projection algorithm. Figures 3.8(i)-(k) are slice images of a tomogram reconstructed by diffraction tomography based on the Rytov approximation, corresponding to the Figs. 3.8(e)-(g), respectively. Figures 3.8(f) and (j) are the slices corresponding to the objective focus plane. Figure 3.8(e) and (i) are slice images 1.7 μm above the focus,

and Figs. 3.8(g) and (k) 2.9 μm below the focus. The bright field images (Fig. 3.8(a)-(c)) were taken for comparison by moving the objective lens at the same height as Figs. 3.8(i)-(k), respectively. It is clear that the structures in both of the refractive index tomograms are well matched to the bright field images. However, if we compare the details of the images at the tomogram slices 2.9 μm below the focus, the difference between tomograms can be seen. Figures 3.8(d), (h) and (l) are the zoom-in images of the white rectangles in Figs. 3.8(c), (g) and (k), respectively. Compared with the bright field image, tomograms processed using the filtered back-projection algorithm show ring pattern for the particles in the cytoplasm, and the two holes in the nucleolus are blurred. In contrast, in the tomogram processed by diffraction tomography, the two holes in the nucleolus are clearly resolved and the particles in the cytoplasm are well in focus (Fig. 3.8(l)). This demonstrates that the Rytov approximation is valid for taking the effect of diffraction into account in reconstructing 3D refractive index maps of live biological cells. As a result, we could clearly image the details of the 3D structures of a single live cell throughout its entire volume as well as quantify the refractive index of sub-cellular organelles.

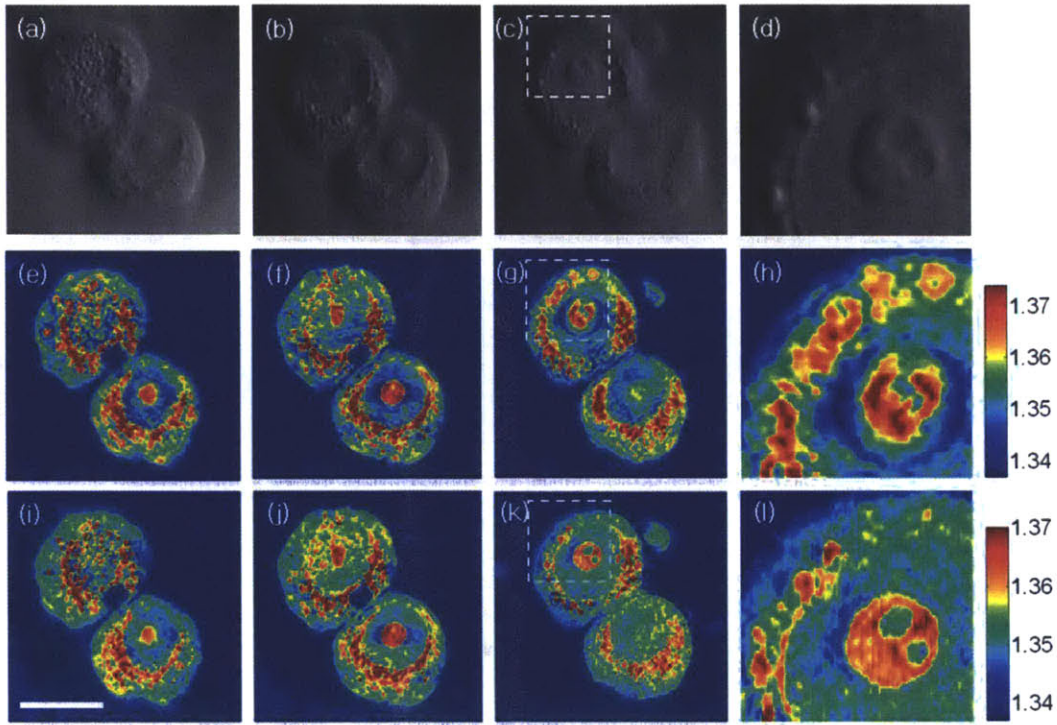


Figure 3.8. Bright field images (a-d), and 3D tomogram of HT-29 cells reconstructed by the filtered back-projection algorithm (e-h) and diffraction tomography based on the Rytov approximation (i-l). (f) and (j) are slice images corresponding to the objective focus. (e) and (i) are slice images 1.7 μm above the original focus. (g) and (k) are slice images 2.9 μm below the focus. (a-c) are bright field images at the same foci as (e-g). (d), (h) and (l) are zoom-in images of the rectangular boxes in (c), (g) and (k), respectively. The color bar indicates refractive indices at 633 nm wavelength. Scale bar, 10 μm .

Chapter 4

Cellular Dry Mass Measurement

4.1. Refractive Index and Cellular Dry Mass

Refractive index is a fundamental property of a material: it is the square root of the dielectric constant; it is a measure of the speed of light in a medium [51]; and it is related to the polarizability of a substance [52] or to the density of a glass [53]. In biology, it has been known that the refractive index is linearly proportional to the concentration of substances in solution [14, 15]. The proportionality constant is called as the specific refraction increment. In 1950s, Barer measured the specific refraction increment for the major substances that compose the cell body as listed in Table 4.1 [14].

Figure 4.1(a) shows the chemical composition of biological cells: water; proteins; carbohydrates; nucleic acids; lipids; etc [54]. Water accounts for about 70% of the total mass; the cell may be thought of as a complex solution in which the substances listed in Table 4.1 are dissolved at various concentrations. Then the refractive index for a local volume within a cell can be written as follows:

$$n(x, y, z) = n_0 + \sum_i \alpha_i C_i(x, y, z) \approx n_0 + \alpha C(x, y, z), \quad (4.1)$$

in which n_0 is the refractive index of a medium. α_i and C_i are the specific refraction increment and the local concentration for the i -th substance, respectively. The quantities α and C are the average specific

refraction increment and the local concentration of the total organic solids within the volume, respectively. The use of the average specific refraction increment α can be justified because the relative amount of substances other than proteins and nucleic acids within the cell is usually small. In addition, Table 4.1 shows that the magnitude of α for the proteins and nucleic acids is about the same, even though for nucleic acids it exhibits some variation.

Substance	Specific refraction increments, α
Bovine serum albumin	0.185
Horse serum albumin	0.184
Human serum albumin	0.186
Egg albumin	0.182
Human gamma globulin	0.188
Human serum globulins	0.181-0.186
Lactoglobulin	0.182
Human fibrinogen	0.188
Lipoproteins	0.171-0.178
Hemoglobin	0.193
Virus nucleoprotein	0.17
Nucleic acids	0.16-0.20
Peptone	0.183
Glycine	0.179
Tryptophane	0.252
Glucose	0.143
Sodium chloride	0.16

Table 4.1. Specific refraction increments of some substances of biological importance [14].

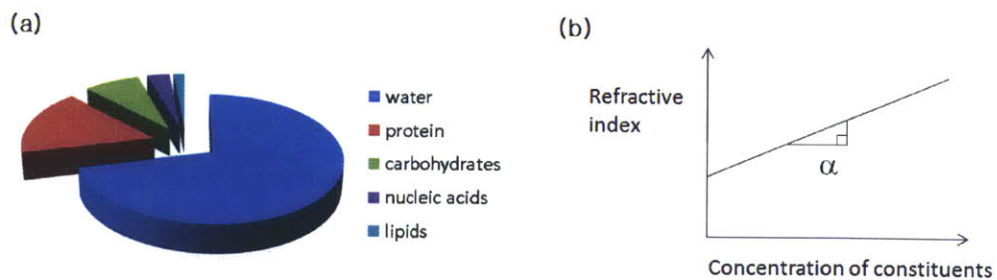


Figure 4.1. (a) Composition of biological cells, and (b) linear relationship of the refractive index and the concentration of substances in solution.

Cellular dry mass refers to the mass of the non-aqueous contents within a cell. The quantitative phase measurement has been used to provide the cellular dry mass under the assumption that the incident beam propagates rectilinearly within a sample [55]. Under the projection assumption, the phase image $\phi(x, y)$ can be interpreted as the projection of $(2\pi/\lambda)(n(x, y, z) - n_0)$ onto $Z = 0$ plane, for which λ is the wavelength of an incident beam. As a result, the cellular dry mass can be calculated from the integral of the areal density $\sigma(x, y) = (\lambda/2\pi\alpha)\phi(x, y)$ over the cell area.

4.2. Tomographic Measurement of Cellular Dry Mass

From the projection-slice theorem [47], the areal density is related to the object spectrum in the $W = 0$ plane. The projection assumption is equivalent to projecting the object spectrum on the Ewald sphere onto this plane as shown in Fig. 4.2(a). The phase imaging approach suffers from diffraction artifacts and degraded spatial resolution dependent on the distance between the Ewald sphere and the $W = 0$ plane.

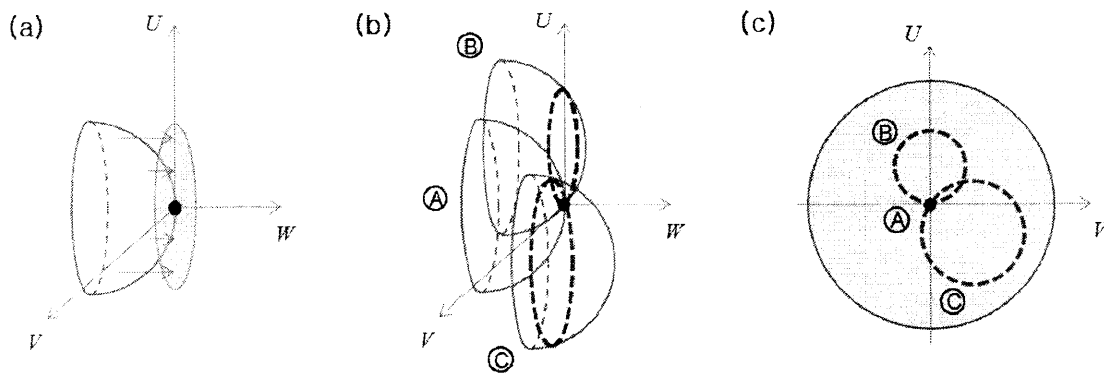


Figure 4.2. (a) Projection assumption, (b-c): diffraction corrected measurement of dry mass. Scattering fields are mapped onto (a) the Ewald sphere, whose intersection with $W=0$ plane is shown in (c).

For the tomographic approach, the object spectrum in the $W = 0$ plane is synthesized from a number of patches as shown in Fig. 4.2(b-c). Each patch represents the intersection of the $W = 0$ plane and the Ewald sphere shifted by different amounts depending on the direction of an incident beam. The object spectrum

on the patch for the incident wave vector (u_0, v_0, w_0) can be found from the Fourier diffraction theorem under the first Rytov approximation [29, 32]:

$$\tilde{f}(U, V, 0) = iw_0 \tilde{\psi}_s(U + u_0, V + v_0), \quad (4.2)$$

in which $f(x, y, z) = (2\pi/\lambda)^2 (n_0^2 - n(x, y, z)^2)$ is the scattering potential of an object, $\psi_s = \ln(E/E_i)$ is the complex phase of the scattering field. E_i and E are the incident and the total field, respectively. The points (U, V) are located on a circle centered at $(-u_0, -v_0)$ with radius $(u_0^2 + v_0^2)^{1/2}$.

By varying the angle of the incident beam, it is possible to fill the $W=0$ plane within the boundary limited by numerical aperture. One efficient way to achieve this is to scan a focused beam at the back focal plane of the condenser lens along a spiral path as shown in Fig. 4.3(b). The areal density in this case can be found using Eq. (4.3); its integral over a cell area provides the diffraction-corrected dry mass.

$$\sigma(x, y) = \frac{1}{\alpha} \int (n(x, y, z) - n_0) dz \approx -\frac{n_0}{2\alpha k_0^2} \int f(x, y, z) dz = -\frac{n_0}{2\alpha k_0^2} \iint \tilde{f}(U, V, 0) e^{i2\pi(Ux+Vy)} dU dV, \quad (4.3)$$

in which $k_0 = 2\pi/\lambda$, λ is the wavelength of the incident field. The magnitude of the truncated higher order terms in the above approximation is around 3% of the first-order term for $n = 1.36$ and $n_0 = 1.337$. If the second-order term is included, the approximation error goes below 0.3%. It is worthwhile to mention that the first-order term is not affected by the missing cone problem caused by the incomplete angular coverage of the incident beam.

Figure 4.3 shows the experimental set-up and how to obtain the diffraction-corrected dry mass. The set-up in Fig. 4.3(a) adopts off-axis digital holography combined with a dual-axis scanning galvanometer mirror. The dual-axis scanning galvanometer mirror enables fast scanning of a focused beam along a spiral path at the back focal plane of the condenser lens. Compared to conventional scans, the spiral-scan tomographic phase microscopy enables to achieve isotropic transverse resolution, which is twice better

than the diffraction limit. Figure 4.3(c) shows the diffraction-corrected phase image synthesized by the tomographic method. The sample was a HT-29 human colon cancer cell, and 400 images acquired within one second were used for the synthesis. Using 1.4-NA oil immersion objective and condenser lenses, the maximum angular coverage was 60° with respect to the optical axis.

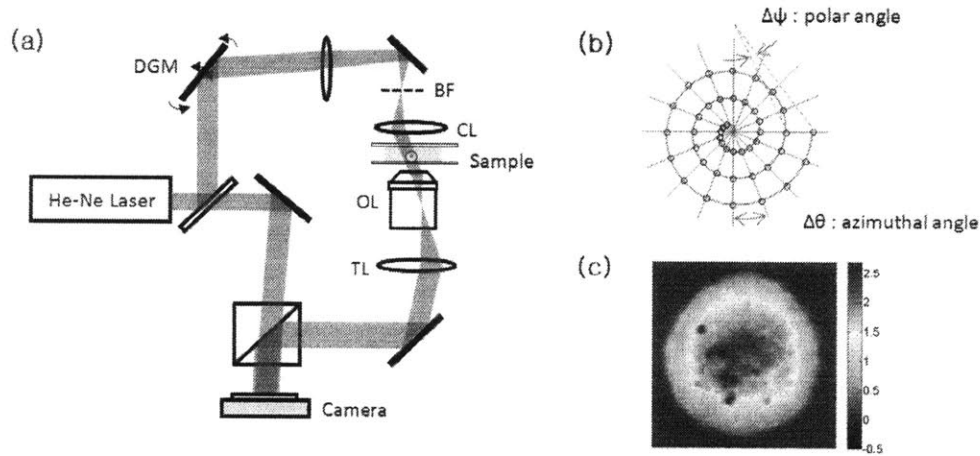


Figure 4.3. (a) Experimental set-up for spiral-scan tomographic phase microscopy, (b) spiral scan path of an incident beam, (c) phase image calculated by the method suggested in this paper. BF: Back focal plane; CL: Condenser lens; OL: Objective lens; TL: Tube lens; DGM: Dual-axis Galvanometer Mirror.

We compare the phase imaging approach using a coherent source and the tomographic approach suggested in this chapter. Figure 4.4 shows how the usual phase image can be affected by the diffraction of a small object. The sample used in the experiment is a 1-micron polystyrene bead immersed in water. Figures 4.4(a) and (b) show two phase images taken at two different locations of focus, one at the center of the bead and the other at 2 micron above the center. If the projection assumption is valid, Figs. 4.4(a) and (b) should be the same, but they are shown to be completely different. Figures 4.4(c) and (d) are the diffraction-corrected phase images for the same conditions as Figs. 4.4(a) and (b), respectively. It is clear that Fig. 4.4(d) has a phase delay which is very close to Fig. 4.4(c), relative to the difference between Figs. 4.4 (a) and (b). The slight differences between Figs. 4.4 (c) and (d) are possibly because the angular

coverage of the incident beam was not complete or because the first Rytov approximation used in the Fourier diffraction theorem was partially broken.

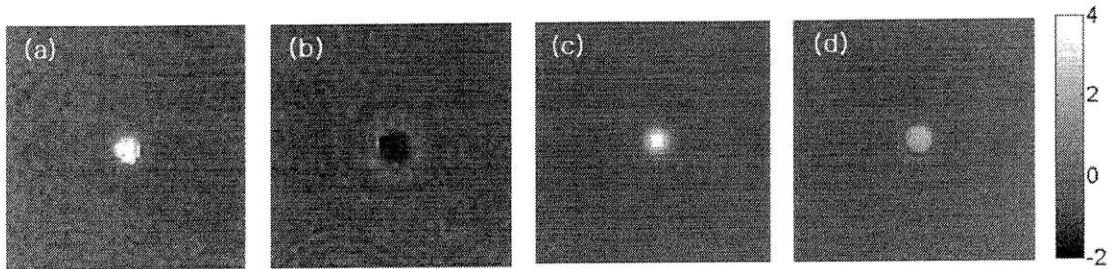


Figure 4.4. Bead defocus test. (a),(c): focus at the center, (b),(d): focus at 2 micron above the center; (a), (b): Single phase image; (c), (d): Phase delay calculated by numerical projection of reconstructed tomogram.

Another important feature of the tomographic approach is its capability to suppress the noise from speckle or dust in the beam path. Figure 4.5 shows a comparison between a usual phase image and a diffraction corrected one. The sample is a RKO human colon cancer cell. The usual phase image shown in Fig. 4.5(a) contains severe speckle noise, which is a typical signature of coherent imaging, while the diffraction corrected one in Fig. 4.5(b) shows remarkably a reduced noise level in the background region. In the tomographic approach, the incident beam is scanned across the back focal plane of the condenser lens, so that speckle noise can be reduced significantly as in the partially coherent imaging. From a slightly different point of view, the patches in Fig. 4.2(b-c) are collected for a number of different incident angles, and they overlap at multiple locations. By taking the average for the overlapping region, random contributions from the noise to the areal density or dry mass can be suppressed. The dry mass calculated by an integral over the dotted region in Fig. 4.5(b) amounts to 2.5 fg, which may be thought of as the noise level of the tomographic method.

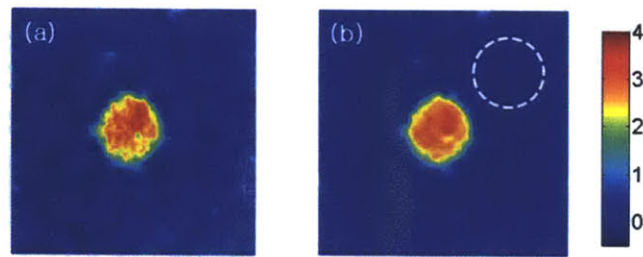


Figure 4.5. Phase delay induced by a RKO cell: (a) single phase image, (b) calculated by numerical projection of 3-D refractive index map. Mass averaged over the dotted line may be thought of as the sensitivity of measurement.

The tomographic approach is the most convincing method that has ever been suggested for the dry mass measurement of a single cell. However, there exist a couple of uncertainties remained. Firstly, the specific refraction increments are different for various substances. The use of the average specific refraction increment will neglect the difference, and provide an error. Secondly, the tomographic approach suppresses the diffraction artifact, but the effect of diffraction suppression depends on the refractive index of the organelle and the amount of defocus. For example, even with the tomographic approach, the value of the dry mass of the polystyrene bead in water was underestimated by around 10fg when the location of focus was at 2 micron above the center of the bead. Finally, moving particles inside a cell may provide additional error in the dry mass measurement. The time to measure the dry mass of a single cell is less than a second. It is possible that some particles within the cell move around while the illumination angles of the incident beam are changed.

4.3. Cell Growth Study

4.3.1. Background

The regulation of cell size is a fundamental property of cellular life. Dysfunction of the signaling pathways controlling cell growth results in cells of altered size and can lead to developmental errors,

contributing to a wide variety of conditions, including cancer, diabetes, and inflammation [56]. In a steady-state cell population, cell growth is coordinated with cell cycle progression, that is, the cellular biomass doubles in quantity during each cell cycle, so that the average cell size is constant over time. Prior research studies on yeast cell growth show that there are internal mechanisms to achieve this [57, 58]. In metazoan cells, there is some evidence that cell growth and cell cycle may be independently regulated [58, 59]. However, both the phenomenon and its biochemical circuit are only poorly understood, and the existing observations of mammalian cell growth deduced contradictory models. For example, it is known that primary rat Schwann cells exhibit a growth rate that is independent of cell size [59], while mouse lymphoblast cells grow exponentially larger with time [60]. This discrepancy may reflect the difference between cell types or the experimental conditions, and for further understanding of metazoan cell growth, it is essential to make more experimental observations of the cell size dynamics.

The major difficulty with the growth measurement is having sufficient accuracy; at least 6% accuracy is needed in size measurement to clearly distinguish the different growth models [60]. The most accurate results have been reported by Tzur et al. [60] using the diameter of spherical cells, and by Godin et al. [61] using the buoyant mass. However, the cell growth is basically the creation of new biomass, the polymerization of small molecules, so the size measurement that depends on diameter or volume may be more artifact-prone if cell density changes. The buoyant mass measurement by Godin et al. [61] is more appropriate in that respect and quite accurate, but their technique requires the cells to flow back and forth within a micro-cantilever system, whose effect on cell growth is unknown yet. The growth rate of adherent HeLa cells was measured by quantitative phase imaging [55] and by the pedestal type mass sensor [62] that monitors the resonance frequency shift as in Godin et al. [61]. The optical measurement of dry mass minimally perturbs the cell, and directly provides the dry mass, which is closely related to the growth.

4.3.2. Results and Discussion

For the long time measurement of live cells under a microscope, an on-stage cell culture system is necessary. The high-NA objective and condenser lenses for the tomographic measurement, however, allow only a small room for the sample installation, so special design considerations need to be made. The on-stage cell culture system that was used consists of a low-profile parallel-plate flow chamber (RC-31, Warner Instruments), a syringe pump for perfusion, a temperature control unit, etc. We extracted culture medium from an exponentially growing culture, and pre-equilibrated it in an incubator for at least 12hr. The oxygen concentration and pH within the chamber are maintained by the continuous flow of conditioned medium. The volume of the space formed within the flow chamber can be adjusted by changing the thickness of a gasket. The optimum thickness for the gasket was determined so that the rate of oxygen supply by the flow of the medium is twice as large as the rate of oxygen consumption by the cells inside. This thickness limits the flow speed within the chamber below 10 micron/sec, which is gentle enough not to disturb cell growth or division. The shear stress at wall is estimated to be around 1mPa, which is very small as well. For the temperature control, a heater embedded in the flow chamber warms both the medium inside and that flowing into the chamber. Line heaters were wrapped around the condenser and objective lenses to minimize heat loss through the immersion oil that is in direct contact with the lenses.

L1210 mouse lymphoblasts were grown in Leibovitz's L-15 CO₂ independent media (Invitrogen) supplemented with 10% FBS (Invitrogen), 1g/L D-(+)-glucose solution (Sigma-Aldrich) and 1% 100X penicillin-streptomycin solution (Gemini). Before the 4-5 hours of measurement, a drop containing L1210 mouse lymphoblasts from an exponentially growing culture was spread on a Poly-L-lysine coated cover slip (40mm, round, no. 1). The number of cells in the culture was monitored using the hemocytometer (Hausser). The concentration of cells on the cover slip was adjusted so that one to two cells are observed within the 50x50-micron field of view.

HT-29 and RKO colon cancer cells were cultured in Dulbecco modified Eagle medium (DMEM) supplemented with 10% FBS and 1% 100X penicillin-streptomycin solution. At 70-80% confluency, cells

were collected by trypsin EDTA (invitrogen) and then diluted to the similar concentration used for L1210. The conditioned medium was collected from the culture of similar confluency. A drop of the diluted cells was spread on a cover slip and then incubated for at least 24hr before the measurement.

The division asymmetry is important because the growth rate of two different daughter cells should be coordinated to guarantee the size homeostasis in the cell population. The division asymmetry proves that there should exist a control mechanism for the growth rate of the cells. The more asymmetric the division is, the more adjustment or control is required. Despite this importance, very few observations of the division asymmetry have been made. Figure 4.6 shows the division asymmetry of HT-29 and RKO colon cancer cells together with that of L1210 mouse lymphoblasts. The division asymmetry of L1210 cells is 7.5 ± 4.8 (%), which is close to the asymmetry measurement based on volume [60]. The division asymmetry of HT-29 and RKO cells are 10.0 ± 6.4 (%) and 13.0 ± 6.8 (%), respectively. HT-29 and RKO cells grow adherently to the surface, while L1210 cells grow in suspension. The observation we made above seems to suggest that adherent cells divide more asymmetrically than floating cells.

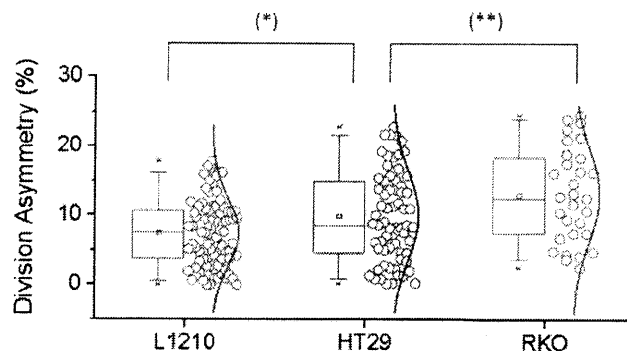


Figure 4.6. Division asymmetry of eukaryotic cells. 7.5 ± 4.8 , 10.0 ± 6.4 , and 13.0 ± 6.8 for L1210, HT-29, and RKO cells, respectively. (*) $p=0.0077$, (**) $p=0.034$.

From the Collins-Richmond model [60, 63, 64], the growth rate as a function of size or dry mass can be calculated based on the distribution of asynchronous steady-state populations, newborns and mitotic cells.

$$f(s) = k \left(2 \int \psi(s) ds - \int \phi(s) ds - \int \lambda(s) ds \right) / \lambda(s), \quad (4.4)$$

in which $f(s)$ is the growth rate as a function of dry mass s . The quantities $\psi(s)$, $\phi(s)$ and $\lambda(s)$ are the probability densities of newborns, mitotic cells and asynchronous populations, respectively. The parameter k is the division rate or the rate of increase in numbers of cells.

Unlike the other methods measuring the resonant frequency shift [61, 62], the optical measurement of dry mass can easily provide the newborn and mitotic cell distribution as well as asynchronous one. Compared to phase imaging [55], the benefit of tomographic approach is its capability of measuring round cells with similar accuracy to thin cells by using the diffraction correction technique explained above. This fact is especially important for the case of dividing cells since they stay round during the division process.

The inputs for the Collins-Richmond model are the probability densities of newborns, mitotic cells and asynchronous populations. Using the Collins-Richmond model, one can calculate the growth rate vs. dry mass curve from the measured inputs. Figure 4.7 shows the inputs and the calculation result for the Collins-Richmond model that was applied to HT-29 and RKO cells. Figures 4.7(a) and (d) show the dry mass distribution of asynchronous populations with the kernel density estimates drawn together as a thick line. The kernel density estimation is a non-parametric way of estimating the probability density function based on a finite data set [65, 66]. For the analysis, a MATLAB based kernel density estimator written by Botev [67] was used. Figures 4.7(b) and (e) show the cumulative dry mass distribution of asynchronous populations, newborns and mitotic cells using the kernel density estimation. Figures 4.7(c) and (f) are the results of the Collins-Richmond model, the growth rate vs. dry mass curves for HT-29 and RKO cells, respectively. The growth rate for both adherent cells exhibits a linear relationship with the dry mass, which provides strong support of the exponential growth model.

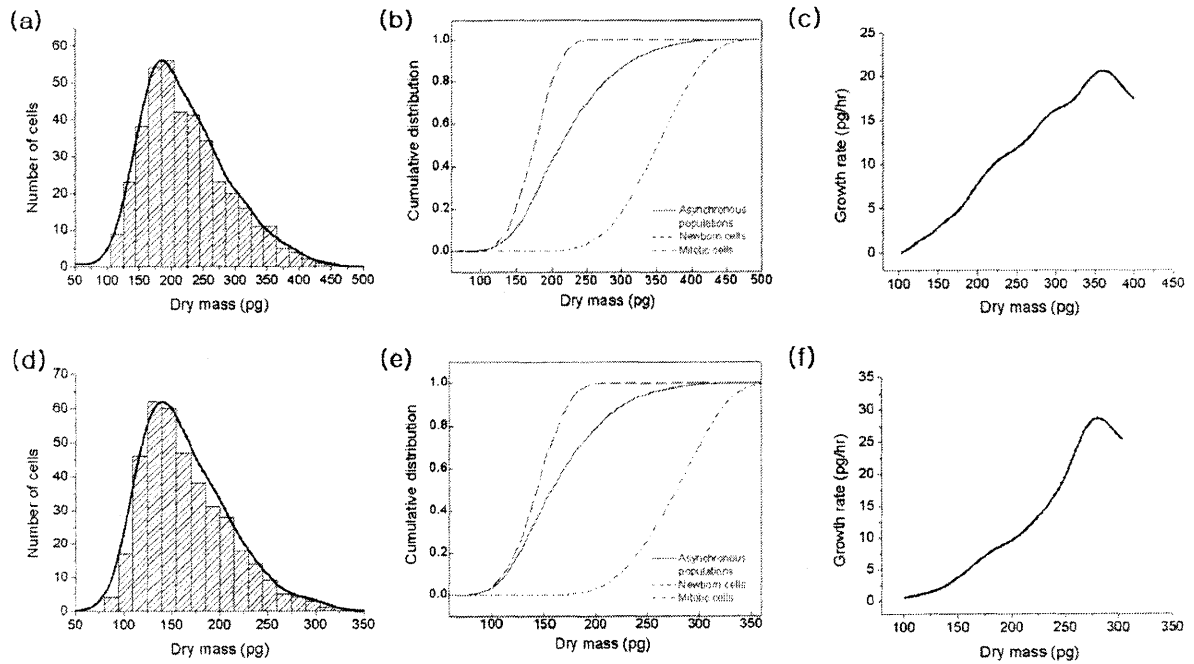


Figure 4.7. Collins-Richmond model for HT-29 (a-c) and RKO cells (d-f). (a), (d): dry mass distribution of asynchronous steady-state populations (kernel density estimates are drawn together); (b), (e): cumulative distribution of asynchronous populations, newborn, and mitotic cells (calculated from kernel density estimates); (c), (f): growth rate vs. dry mass.

4.4. Drug Effect Monitoring of Multiple Myeloma Cells

4.4.1. Background

Multiple myeloma (MM) is a cancer of plasma cells and represents the second most common hematologic malignancy in the western world [68, 69]. Although MM is incurable as of today, its prognosis has been drastically changed by the introduction in clinics of novel agents such as proteasome inhibitor (PI) bortezomib (PS-341) and immunomodulatory drugs (IMiDs). Bortezomib, the first in class PI, was approved under an accelerated program by the FDA as a third-line agent in MM treatment in 2003 on the base of its remarkable effectiveness in phase II/III clinical trials. Currently, bortezomib is approved as a

front-line agent for the treatment of MM and second-line therapy for mantle cell lymphoma. However, clinical studies showed around two thirds of patients treated with bortezomib as a single agent are resistant, raising the question of the mechanisms behind bortezomib effectiveness [70, 71]. These mechanisms are only partially understood and no predictive factor of response is available for clinical use. A deeper understanding of the pathways activated during bortezomib-induced death and the exquisite molecular targets affected by its activity would be crucial to improve the clinical response rate, design ad hoc combinatory treatments and more effective new-generation PIs.

The molecular target of bortezomib is the 26S proteasome, a barrel-shaped, 2400 kDa multi-catalytic protease complex expressed in the cytoplasm and nucleus of eukaryotic cells [72, 73]. The proteasome is the major proteolytic machinery of eukaryotic cells and it is crucial for the timely degradation of proteins involved in cell cycle [74], cytokine production [75], angiogenesis [76] and apoptosis [77, 78]. It is also responsible for the dismantling of misfolded/unfolded proteins, including newly synthesized, defective polypeptides (rapidly degraded polypeptides or RDPs) whose accumulation could be toxic [79]. Most of the proteasome substrates are directed toward degradation via conjugation with a poly-ubiquitin chain in a process mediated by the serial activity of three enzymes: ubiquitin (Ub)-activating enzymes, E1 [77]; Ub-conjugating enzymes or E2 [80]; and Ub-ligase or E3 [81]. Indeed, the hallmark of proteasome inhibition is accumulation of poly-Ub proteins. This can be monitored via several molecular biology techniques, including protein electrophoresis and immunoblotting, and immunofluorescent staining of polyubiquitinated proteins [82]. While both immunoblotting and immunofluorescence are easy to perform on cell lines in vitro, the former technique requires a large number of cells while the latter has a photo-bleaching problem, which limits the duration of observation, thus negatively impacting time-course experiments.

We proceed to investigate whether hallmark of the cellular response to bortezomib could be unequivocally established in MM cell lines by means of tomographic measurement of cellular dry mass, and if this technique is capable of distinguishing between cells irreversibly committed to death and others

that could be still rescued by removing the toxic stimulus. We demonstrate that tomographic measurement of cellular dry mass is a feasible technique to study longitudinally the effect of drug treatment on MM cells. Being a per-cell based technique, a limited number of cells (less than 150) is sufficient to obtain quality data. The increase in mass can be monitored without adding anything.

4.4.2. Results and Discussion

Normal plasma cells were obtained from bone marrow aspirates obtained during orthopedic surgery of patients undergoing total hip or knee replacement. The presence of hematologic or solid cancer excluded the patients as healthy controls. Informed consent was obtained from all patients in accordance with the Helsinki protocol. Mononucleated cells were isolated via Ficoll Hypaques density gradient centrifugation and plasma cells were subsequently identified via positive immunomagnetic selection against CD138 using an Auto MACS magnetic cell sorter (Miltenyi Biotec Inc., Auburn, CA).

Human MM cell lines (MM.1S and RPMI8226) and normal plasma cells were cultured in RPMI media supplemented with 10% FBS, glutamax (1 mM), and 1% 100X penicillin-streptomycin solution. Cells were treated with 20 nM bortezomib for the indicated times below, washed twice in PBS, resuspended in fresh RPMI media. It took less than 20 minutes to search for the cells while moving the field of view, and to take 140 tomograms.

Using the tomographic system, we measured the volume and dry mass of normal plasma cells and MM.1S human myeloma cells. As shown in Fig. 4.8, MM.1S cells have a larger volume and dry mass than normal plasma cells, possibly due to the massive production of M proteins within the myeloma cells. The density of both samples is estimated to be same, 100 g/L.

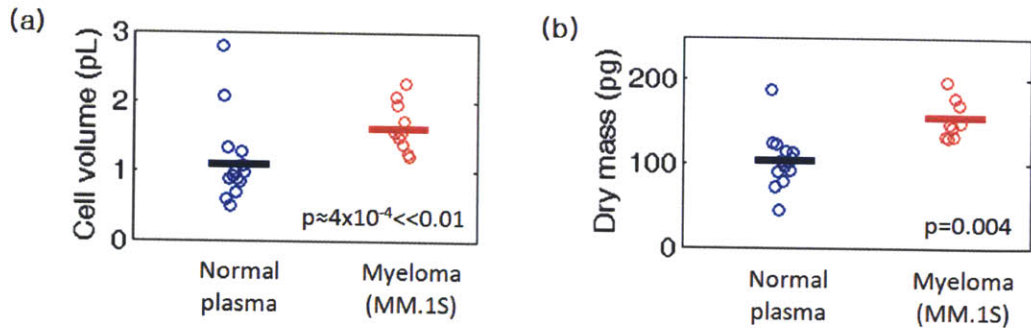


Figure 4.8. Volume and dry mass of normal plasma cells and MM.1S multiple myeloma cells. Myeloma cells have larger dry mass than normal plasma cells mainly due to their larger volume. (Their density is same; plasma cells $\sim 100 \pm 24$ g/L, myeloma cells 100 ± 19 g/L).

Figures 4.9 (a) and (b) show the cross-section of the refractive-index map of a MM.1S cell before and 4hr after adding 20nM bortezomib. The refractive index is the concentration of the dry mass, non-aqueous content of a cell, so Fig. 4.9 suggests the concentration of the myeloma cells increases upon the treatment with bortezomib. We believe this increase in concentration is due to the accumulation of the polyubiquitinated proteins. The treated cell is shown to shrink in volume probably as a response to the drug, but the dry mass (the integral of the concentration over the volume) increases more than that due to its normal growth.

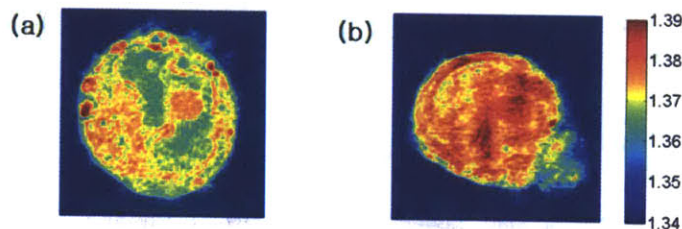


Figure 4.9. Cross-section of refractive index map of a RPMI8226 human myeloma cell at 0hr and 4hr after the treatment (20nM bortezomib).

Figure 4.10 compares the response of MM.1S and RPMI 8226 cells, which are known to have different sensitivity to the bortezomib treatment. The EC_{50} dose of bortezomib for RPMI has been reported to be 2.5-10 times higher than for MM.1S by different authors. After 1hr of adding 20nM bortezomib, the dry

mass of the MM.1S cell populations increases from 134 ± 48 to 153 ± 61 pg, which is statistically significant ($p = 0.0046$). On the other hand, the dry mass of the RPMI 8226 cells does not change significantly ($p = 0.85$).

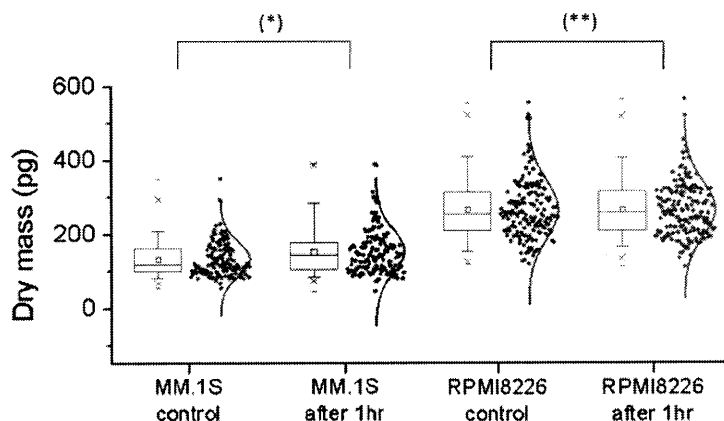


Figure 4.10. Dry mass change after adding proteasome inhibitor (20nM bortezomib) to MM.1S and RPMI8226 cells (140 cells for each). (*) $p = 0.0046$, (**) $p = 0.85$.

Figure 4.11 shows the dry mass of the MM.1S cell populations treated by 20-nM bortezomib for 4 hrs, and compares it with the 1-hr treatment and the control group. The average values of dry mass for the 1-hr and the 4-hr treatment groups are almost the same, which suggests that the effect of the bortezomib is active within the first hour and then stays at the same level. Figure 4.11(b) shows the probability distribution of dry mass for the control, 1-hr and 4-hr treatment groups. The probability density of the dry mass is the outcome of an intricate balance between the production and destruction of cellular masses as well as of cell division. The control group has a strong peak around 100 pg and a small peak around 165 pg. Compared to the control, in the 1-hr treatment group the main peak is reduced by about 27%, and the probability density of the cells with dry mass larger than 200 pg increases. On the other hand, in the 4-hr treatment group another peak around 170 pg appears with the same height as the main peak, and the probability density of the cells with large dry mass is reduced. It is not clear what mechanism in the cells causes the change in the distribution between 1-hr and 4-hr treatment groups, but it suggests various defense mechanisms may be occurring in the cell population as an adaptive response to the drug.

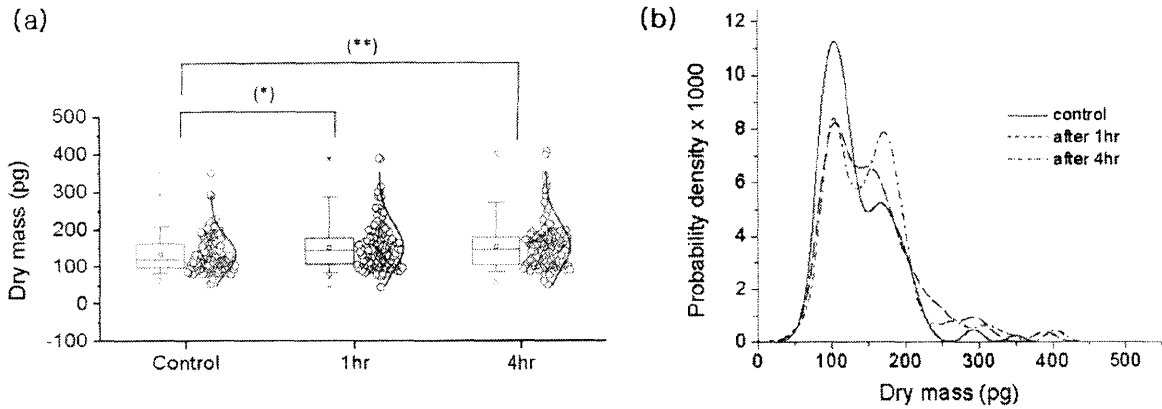


Figure 4.11. Dry mass change after adding proteasome inhibitor (20nM bortezomib) to MM.1S (multiple myeloma) cells (140 cells for each). (*) $p = 0.0046$, (**) $p = 0.0019$.

Figure 4.12 shows the dry mass of the RPMI 8226 cell populations treated by 20nM bortezomib for 4 hrs, and compares it with the both the 1-hr treatment and control groups. The 1-hr treatment group does not show a significant increase in dry mass compared to the control, which is not surprising considering that 20 nM is a relatively well tolerated dose for RPMI 8226 cells. However, the dry mass of the 4hr treatment group is significantly different from to the control, which suggests a time delay exists between the drug administration and onset of pro-apoptotic effects.

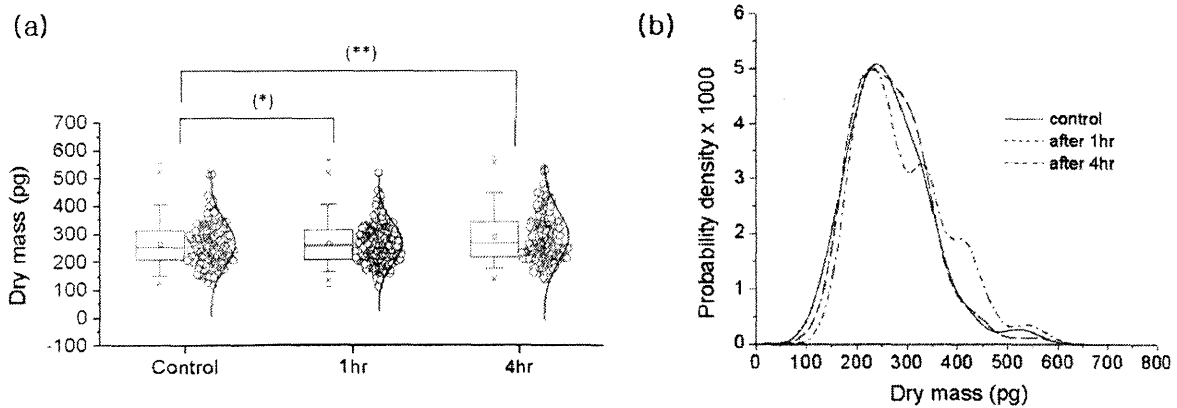


Figure 4.12. Dry mass change after adding proteasome inhibitor (20nM bortezomib) to RPMI8226 (multiple myeloma) cells (140 cells for each). (*) $p = 0.85$, (**) $p = 0.0041$.

Figure 4.13 compares the dry mass of the RPMI 8226 cell populations treated by various amounts of bortezomib for 1 hr. With 100-nM bortezomib, the average value of dry mass increases from 265 ± 79 pg to 290 ± 94 pg. Further increase of the dose does not increase the dry mass, although cells with large dry mass are observed more frequently in the group treated with 200 nM bortezomib than the group treated with 100 nM. For the dose larger than 200 nM, floating cells with irregular cell membranes are often observed, which indicates the dose is high enough to drive some cells directly into the necrosis. Looking only at the change in dry mass, it is interesting to observe that treatment with 20-nM bortezomib for 4 hrs is as effective as that with 100 nM for 1 hr. If there exists any time delay similar to what has been observed in the group treated with 20 nM, it would be less than 1 hr in the 100-nM group; the latency time depends on the dosage. It is also interesting to compare the probability distributions of the group treated with 20 nM for 4 hr and the group treated with 100 nM for 1 hr. In the 20-nM, 4-hr treatment group, the peak probability stays about the same, while in the 100-nM, 1-hr treatment group the peak probability decreases. The decrease in the peak probability was also observed in the MM.1S cells treated with 20 nM for 1 hr. Considering all these results, the response of myeloma cells to bortezomib depends both on the dose and the duration of treatment.

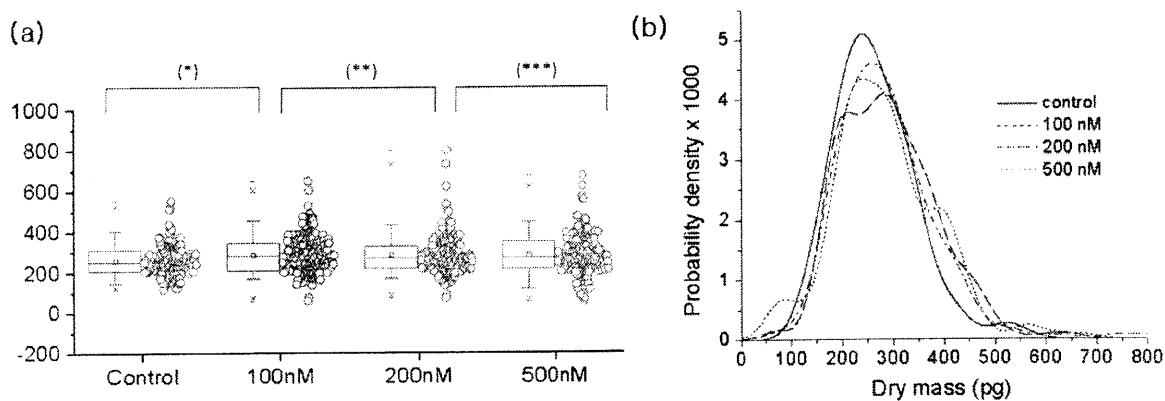


Figure 4.13. Dry mass change after adding proteasome inhibitor of various concentrations to RPMI8226 (multiple myeloma) cells (140 cells for each). (*) $p=0.0075$, (**) $p=0.024$, (***) $p=0.82$. Cells that go through necrosis are often observed at 500 nM.

Chapter 5

4- π Tomographic Phase Microscopy

Reproduced in part from Yongjin Sung and Ramachandra R. Dasari, " Deterministic regularization of three-dimensional optical diffraction tomography," J. Opt. Soc. Am. A (under review).

5.1. Introduction

Diffraction tomography is an inverse scattering technique used to reconstruct a three dimensional object from a series of two dimensional measurements of the scattering field. Based on the Fourier diffraction theorem introduced in Chapter 2, 2-D scattering fields can be mapped onto a 3-D frequency spectrum of the scattering potential. The so-called Fourier mapping is conceptually straightforward and fast, but the mapping of the 2-D scattering field onto 3-D rectangular coordinates requires an interpolation and induces an artifact. As an analog of the filtered back-projection, the filtered back-propagation method [83] resolves this problem, and is known to provide a better quality [84]. However, the filtered back-propagation is valid only within the Born approximation, and its 3-D application is quite involved. On the other hand, iterative reconstruction can overcome these limitations by iteratively updating a trial solution based on a scattering model and *a priori* knowledge about a sample. The main benefits of iterative reconstruction come from the regularizing effect of the iterative process and the capability of incorporating various pieces of information about a sample such as maximum energy, piecewise smoothness, etc. Iterative reconstruction has been applied to projection tomography that neglects

diffraction effects [85-87] and then to diffraction tomography [88, 89] which Zunino et al. used to find the magnetization distribution in a buried layer from measurements of magnetization at the surface [88]. Bronstein et al. applied it to suppress the noise in the broad-band ultrasound tomography [89].

In this chapter, we apply iterative reconstruction to 3-D optical diffraction tomography (ODT) and focus on the recovery of the missing cone. The missing cone originates from incomplete angular coverage of the incident beam and arises in most practical applications of diffraction tomography. The missing cone leads to elongation of the reconstructed shape along the optical axis and to underestimation of refractive index [2]. It is worthwhile to note that the rotating-sample tomography also suffers from the missing cone problem when the sample is rotated around one axis [90]. We mention that iterative reconstruction without additional constraints has been called ART (algebraic reconstruction technique). Ladas and Devaney [91] showed that ART is capable of reconstructing a sample from a limited amount of data only insofar as the data are noise-free [84]. By removing the missing-cone using the regularization, the 3-D refractive index map can be reconstructed from the scattering into the whole solid angle or the 4π .

To analyze the imaging characteristics of optical diffraction tomography, we look into the transfer function. Figures 5.1(a) and (b) show the transfer functions for 2-D and 3-D 'rotating-beam' optical diffraction tomography, respectively. Figure 5.1(a) may be considered as the K_x - K_z cross section of the 3-D transfer function shown in Fig. 5.1(b). In this case, the arcs in Fig. 5.1(a) represent the cross-sections of the Ewald sphere, the hemispherical surface, with the K_x - K_z plane in Fig. 5.1(b) for various illumination angles. It is important to note there exists a region that is not covered by the transfer function even with the maximum angular coverage of the incident beam, from -90° to 90° with respect to the optical axis. The region is called missing cone of 'rotating-beam' optical diffraction tomography. A similar missing cone occurs in 'rotating-sample' tomography when a sample is rotated with respect to one axis. Figures 5.1(c) and (d) show how the missing cone affects the reconstruction of a homogeneous, spherical bead. In this simulation, the scattering field was generated by the method that will be explained below, and the Fourier mapping was used for the reconstruction. The angular coverage is from -60° to 60° , which is about the

maximum practically achieved with the high NA (1.4) oil immersion lens. Figure 5.1(c) is the cross-section of the reconstructed bead within the plane containing the optical axis, and Fig. 5.1(d) is the refractive index profile along the optical axis. As expected from the Gibbs ringing, the missing cone is responsible for the elongation of the reconstructed object along the optical axis direction. In addition, the refractive index of a bead is underestimated correspondingly.

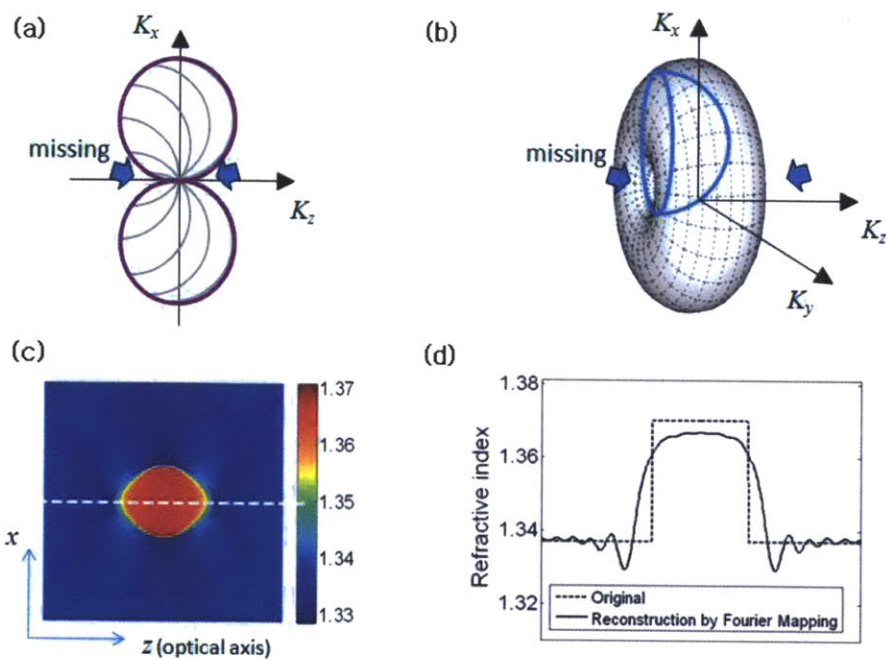


Figure 5.1. Transfer function of diffraction tomography and some results of reconstruction. (a) Transfer function of 2-D diffraction tomography and (b) 3-D diffraction tomography, (c) vertical cross-section of the reconstructed refractive index map using the Fourier mapping, (d) index profile of (c) along the dotted line. The sample used for the simulation is a homogeneous, spherical bead with the refractive index 1.37. (K_x, K_y, K_z) , the spatial frequencies in the object frame.

The next section shows how in the iterative reconstruction framework additional constraints suppress these artifacts and improve the accuracy of the prediction of the refractive index. More specifically, we apply both the positivity constraint and the piecewise smoothness constraint for the reconstruction of

several samples. It is important to note that these constraints can be applied for any kind of samples without additional measurement.

5.2. Iterative Reconstruction with Additional Constraints

Iterative reconstruction is a method to update a trial solution based on a scattering model and *a priori* knowledge about a sample until it converges. The main benefits of iterative reconstruction come from the regularizing effect of the iterative process and the capability of incorporating various pieces of information about a sample such as maximum energy, piecewise smoothness, etc. Iterative reconstruction has been applied to projection tomography that neglects diffraction effects [85-87] and then to diffraction tomography [88, 89] which Zunino et al. used to find the magnetization distribution in a buried layer from measurements of magnetization at the surface [88]. Bronstein et al. applied it to suppress the noise in the broad-band ultrasound tomography [89]. We mention that iterative reconstruction without additional constraints has been called ART (algebraic reconstruction technique). Ladas and Devaney [91] showed that ART is capable of reconstructing a sample from a limited amount of data only insofar as the data are noise-free [84].

5.2.1. Diffraction Tomography as Inverse Problem

Optical diffraction tomography can be considered as a problem of minimizing the following functional:

$$\Phi_{\mu}(f;g) = \frac{1}{2} \sum_n \|A_n f - g_n\|^2 + \alpha J(f), \quad (5.1)$$

in which $\Phi_{\mu}(f;g)$ is the cost functional, α is a regularization parameter, $J(f)$ is the penalty functional, f is the objective function to be reconstructed, A_n is the n th diffractive projection of f onto the plane $z=0$, g_n is the measured scattering field, $U(\bar{R})/U^{(l)}(\bar{R}) - 1$ in the first Born approximation, or g_n is $\ln(U(\bar{R})/U^{(l)}(\bar{R}))$ in the first Rytov approximation.

The regularization parameter α can be chosen based on various methods [92]. Equation (5.1) is minimized by the function f_μ that can be found by the following iteration [93]:

$$f_\mu^{(k+1)} = f_\mu^{(k)} + \tau \sum_n (A_n^\dagger g_n - A_n^\dagger A_n f_\mu^{(k)}) - \tau \alpha \nabla J(f_\mu^{(k)}), \quad (5.2)$$

in which τ is the relaxation parameter, and A_n^\dagger is the adjoint operator defined below.

Within the first Born or Rytov approximation, the forward operator for the 3-D optical diffraction tomography may be defined as follows:

$$A_n f = \iint \frac{1}{i4\pi w} \tilde{f}(K_x, K_y, K_z) e^{i2\pi(K_x x + K_y y)} dK_x dK_y, \quad (5.3)$$

in which \tilde{f} is the Fourier transform of f , $k_z = \sqrt{(1/\lambda)^2 - (K_x + k_{x0}(\theta_n))^2 - (K_y + k_{y0}(\theta_n))^2}$,

$K_z = k_z - k_{z0}(\theta_n)$, and $k_{z0}(\theta_n) = \sqrt{(1/\lambda)^2 - k_{x0}(\theta_n)^2 - k_{y0}(\theta_n)^2}$.

For the adjoint operator A_n^\dagger , we define inner products as in Ladas & Devaney [94]:

$$(g_1, g_2)_X = \int g_1^*(x, y) g_2(x, y) dx dy, \quad (5.4)$$

$$(f_1, f_2)_Y = \int f_1^*(x, y, z) f_2(x, y, z) dx dy dz.$$

in which X, Y are the Hilbert space of square integrable functions defined on $\mathcal{R}^2, \mathcal{R}^3$, respectively. Then, the adjoint operator A_n^\dagger is the operator satisfying the following relationship:

$$(A_n f, g)_X = (f, A_n^\dagger g)_Y, \quad (5.5)$$

which can be calculated by

$$A_n^\dagger g = \iint \frac{1}{-i4\pi k_z} \tilde{g}(K_x, K_y) e^{i2\pi(K_x x + K_y y + K_z z)} dK_x dK_y. \quad (5.6)$$

Finally, the composite operator in Eq. (5.2) may be simplified as follows:

$$A_n^\dagger A_n f = \iint \frac{1}{(4\pi k_z)^2} \tilde{f}(K_x, K_y, K_z) e^{i2\pi(K_x x + K_y y + K_z z)} dK_x dK_y. \quad (5.7)$$

Using the forward operator defined in Eq. (3.11), we can generate scattering fields that is valid within the first Rytov approximation. As a sample we use a 3-D Shepp-Logan phantom [95] modified to have the real refractive index of usual biological samples (1.35-1.37) with negligible absorption.

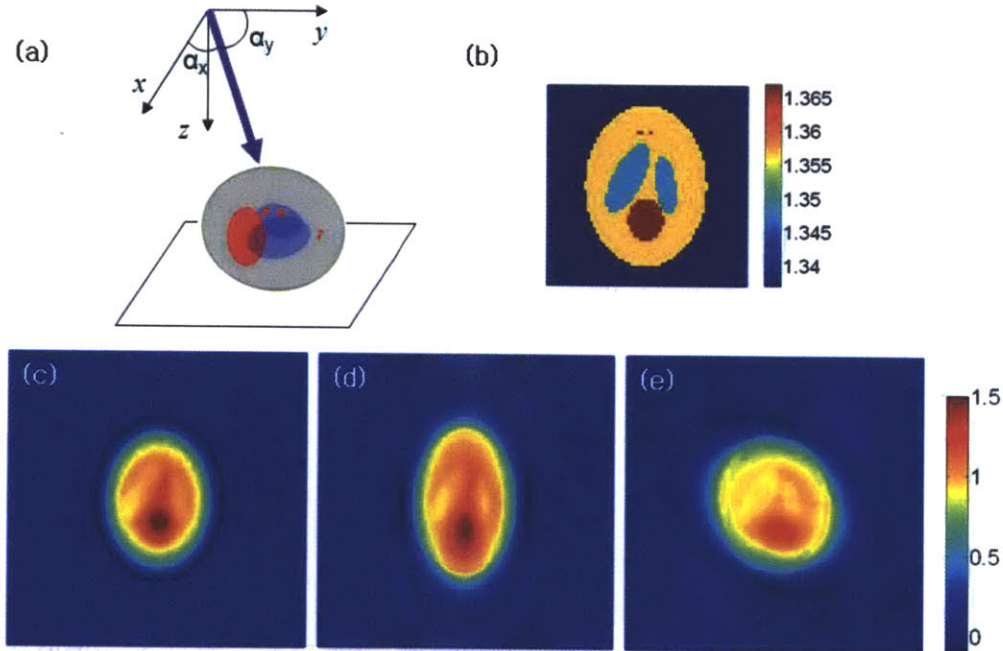


Figure 5.2. Modified 3-D Shepp-Logan phantom and its scattering fields calculated for various illumination angles: (a) 3-D rendered phantom with the wave vector of the incident wave shown as a thick, purple line, (b) center cross-section of the phantom refractive index, (c)-(e) scattered fields calculated for the incident angle of (c) $\alpha_x=90^\circ, \alpha_y=90^\circ$, (d) $\alpha_x=90^\circ, \alpha_y=49.5^\circ$, (e) $\alpha_x=51.5^\circ, \alpha_y=78.3^\circ$. Color bar for (c)-(e) indicates the phase delay in radian after the phase unwrapping.

Figures 5.2(a)-(b) shows the schematic of the set-up for the numerical simulation. In Fig. 5.2(a), z is the optical axis, and the thick, purple line represents the wave vector of the incident beam. Figure 5.2(b) is the center cross-section of the 3-D phantom, in which color represents the refractive index value. Figures 5.2(c)-(e) show scattering fields from the modified 3-D Shepp-Logan phantom for various illumination angles. For the reconstruction of the tomogram, 200 phase images were used for incident angles varying from 0° to 60° with respect to the optical axis. Since the index of refraction of the phantom is real, the phase delay induced in the scattering field contains information about the sample.

5.2.2. Edge Preserving Regularization

The exact form of the penalty functional in Eq. (5.1) is determined by the kind of constraint used for the regularization. For example, the penalty functional for the Tikhonov regularization $J(f) = 1/2 \int |f|^2 dV$ penalizes the energy of the objective function so that the optimized solution possesses minimal energy of noise [96]. Alternatively, the functional that penalizes the gradient of the objective function may be used to smooth out the noise while preserving the sharp edge. The so-called edge preserving regularization corresponds to using the piecewise smoothness constraint. Charbonnier et al. suggested criteria for the form of the penalty functional that will define an edge preserving regularization with guaranteed convergence to a solution [97]. Equation (3.16) shows an example satisfying those criteria; it will be used in this section.

$$J(f) = 1/2 \int \psi(|\nabla f|^2) dV , \quad (5.8)$$

in which f is the objective function, dV is the volume element in space, $\psi(t) = \sqrt{t + \beta^2}$, and β is an arbitrary, small number that prevents $\psi'(t)$ from having a singular value at $t=0$.

Now we introduce some noise into the scattering fields generated by numerical simulation. The physical origin of the noise can be speckle, dust in the beam path, phase unwrapping error, etc. For example, Fig.

5.3(a) shows the same cross-section as Fig. 5.2(c) after being corrupted by Gaussian noise adjusted to have a noise level of the same order of magnitude as the signal. From the corrupted scattering fields, we try to reconstruct the original 3-D phantom first by the Fourier mapping and then by the iterative reconstruction with the edge preserving regularization. Figures 5.3(b)-(c) show the center cross-section of the reconstructed 3-D refractive index map. In the Fourier mapping process, there can be an overlap in the frequency domain since the data are collected from various illumination angles. In such a case, we take the average, which helps to suppress the noise to some extent. For example, in Fig. 5.3(b) the boundary of internal structures is visible, which is surprising considering the noise level in the scattering fields as in Fig. 5.3(a). Figure 5.3(c) is the same cross-section as Fig. 5.3(b), but after the iterative reconstruction using the edge preserving regularization.

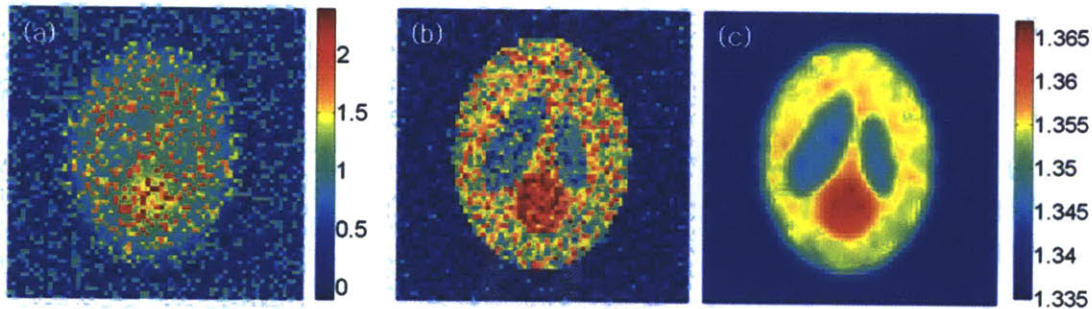


Figure 5.3. Noise handling capability of edge preserving regularization. (a) An example of a scattering field corrupted with additive noise, (b) horizontal cross-section of the reconstructed 3-D image using direct mapping by the Fourier diffraction theorem, (c) horizontal cross-section of the reconstructed 3-D image by the iterative reconstruction with the edge preserving penalty.

As the figure clearly shows, most of the noise in the scattering fields is suppressed, while the boundaries of the internal structure stay sharp. The noise handling capability of the edge preserving regularization was demonstrated by Bronstein et al. [89] in the 2-D diffracting field under the first Born approximation. However, here we show the edge preserving regularization can restore the absolute value of the 3-D refractive index, even when the scattering fields are corrupted by the same level of phase noise as signal.

In addition, our result is based on the first Rytov approximation, which is more appropriate for the optical imaging of biological samples [32].

5.2.3. Effect of Constraints on Missing Angle Recovery

Delaney & Bresler applied the edge-preserving regularization to the missing cone problem of projection tomography using a non-diffracting source [86]. They showed the edge-preserving regularization can recover edges that were smoothed out by the missing cone. For projection tomography, the inverse Radon transform is used for the reconstruction, which assumes the incident field propagates rectilinearly within the sample [98]. This assumption is not valid in optical imaging of a biological sample because small organelles within the sample diffract the transmitted light. Therefore, projection tomography cannot be used for high-resolution, optical imaging of 3-D biological samples. In this section, we apply the edge-preserving regularization to 3-D optical diffraction tomography, and show how it recovers the sharp edge smoothed by the missing cone and improves the accuracy of the prediction of the refractive index.

In this section the piecewise smoothness constraint is used together with the positivity constraint. In the Gibb's ringing, a sharp edge reconstructed from the spectrum of finite bandwidth displays an undershoot below the background amplitude. Similarly, the refractive index profile reconstructed from a finite bandwidth spectrum contains negative regions with the refractive index below that of the medium. Since the refractive index is proportional to the concentration of dry mass, the medium is supposed to have the smallest refractive index [15]. Hence, using this prior knowledge we can force those negative regions to have the same refractive index as the medium, by which we can create new information that may improve the overall image quality. Together with the Fourier mapping, we already showed the positivity constraint is capable of recovering missing cone to some extent [32]. Our interest here is to further improve the image by combining the piecewise smoothness constraint with the others in an iterative reconstruction

framework. The use of the positivity constraint to retrieve the out-of-band information is also known as Gerchberg-Papoulis algorithm [99, 100].

Using the projection operator, the positivity constraint can be incorporated into the iterative reconstruction as follows:

$$f_{\mu}' = D_{\Omega}f_{\mu} + \bar{D}_{\Omega}P_{+}f_{\mu}, \quad (5.9)$$

in which D_{Ω} is the band-limiting operator preserving only the components inside the frequency band Ω , \bar{D}_{Ω} is a complementary operator to D_{Ω} preserving only components outside of the band, Ω is the frequency support of the measured spectrum, and P_{+} is the projection operator for the positivity constraint which is defined as $P_{+}f_{\mu} = f_{\mu}$ if $f_{\mu} > 0$, and 0 otherwise.

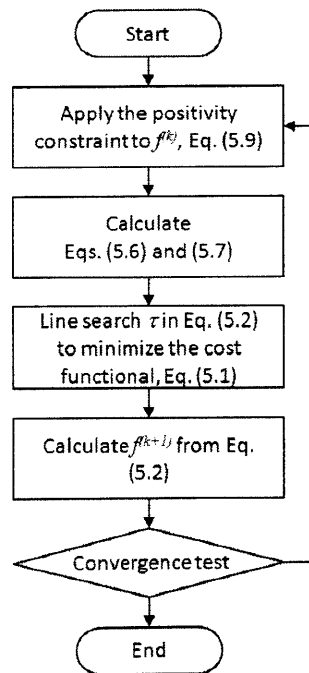


Figure 5.4. Flow chart for the iterative reconstruction with the positivity and the piecewise smoothness constraints.

Figure 5.4 summarizes the iterative reconstruction process described in this section.

For the case of the recovery of the sharp edge, we look at the refractive index profile along the optical axis. The index profile in the transverse direction is not affected by the missing cone, and it is sharp with two times better resolution than the diffraction limit [32]. For the accuracy of the prediction of the refractive index, we introduce the refractive index histogram as shown in Fig. 5.5(b). An ideal reconstruction of a homogeneous sample will provide a delta-function like peak, so the width of the broadened peak can be used to estimate the accuracy of the prediction.

Let us consider a spherical bead sample with homogeneous refractive index of 1.37, the same as in the previous section. Figure 5.5(a) shows profiles of the refractive index along the optical axis after reconstruction by various methods. As observed before, for angular coverage from -60° to 60° the Fourier mapping provides an edge smoothed out approximately over the radius of the bead. The positivity constraint helps to recover the edge, but it induces strong oscillation of the profile at the center of the bead. On the other hand, the iterative reconstruction together with the positivity and the piecewise smoothness constraint provide a sharp edge with noticeable reduction in the oscillation of the profile. Figure 5.5(b) shows more dramatically how the missing cone artifact is reduced by additional constraints. In case of the Fourier mapping, the peak of the index histogram is formed near 1.367, which underestimates the refractive index by 0.003. Because the refractive index of a biological sample usually differs from the culture medium by less than 0.03, this underestimation can be a significant error. The positivity constraint helps to increase the mean value almost to the original one, but the width of the peak, which is about 0.005, indicates the index prediction across the volume is still not accurate enough. However, iterative reconstruction, using the positivity and the piecewise smoothness constraints, provides a sharp peak centered at 1.37 with the width less than 0.001. This result suggests that we can obtain a 3-D refractive index map with an accuracy of less than 0.001 using practically attainable angular coverage from -60° to 60° .

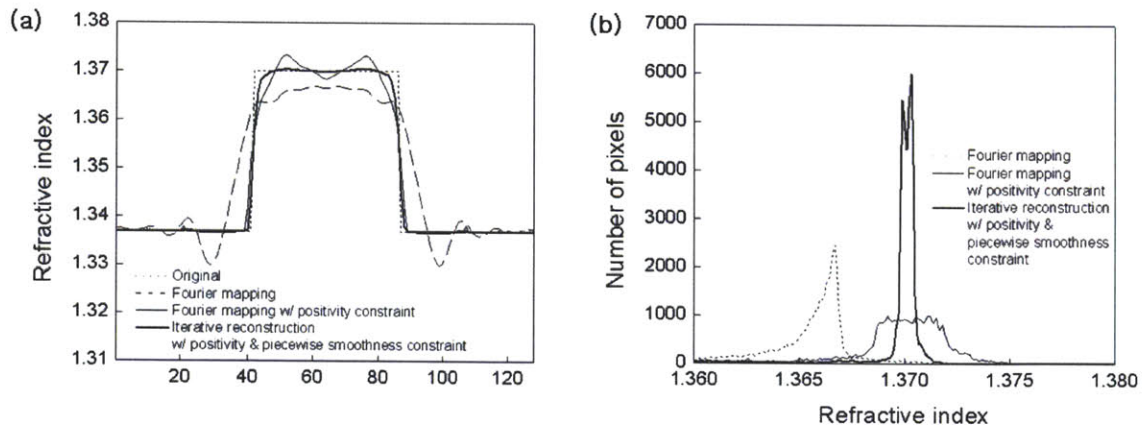


Figure 5.5. Simulation with a spherical bead: (a) comparison of index profile along the optical axis, (b) histogram of the 3-D refractive index map, which was reconstructed by various methods.

The missing cone artifact becomes more serious when a sample is squashed in the optical axis direction as in Fig. 5.6(a). As a result, the flattened sample has an elongated spectrum in the κ_z direction as in Fig. 5.6(b), in which κ_z is the spatial frequency corresponding to the optical axis, z . The frequency support of the transfer function is fixed for given angular coverage, while the elongated spectrum has more information missing.

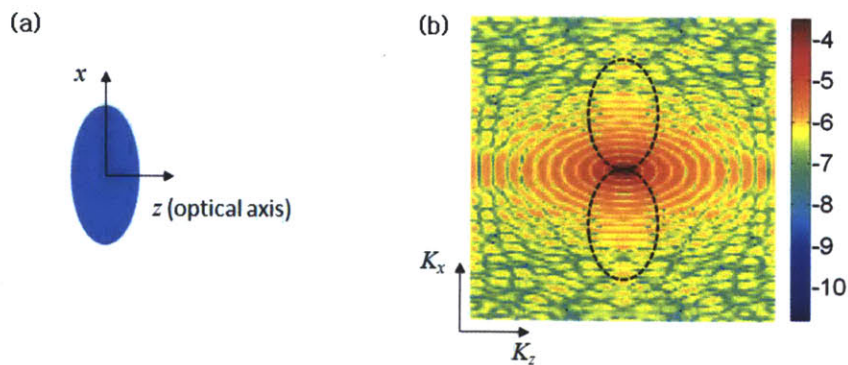


Figure 5.6. (a) A spherical bead squashed in the optical axis direction with the aspect ratio of 2 to 1, (b) spatial frequency spectrum of (a), in which the frequency support of the transfer function for the angular coverage from -60° to 60° is drawn as a dotted line. The color bar indicates the amplitude of the spectrum in the logarithmic scale with base 10.

Figure 5.7 shows refractive index profiles along the optical axis and corresponding index histograms of the squashed bead after reconstruction using various methods. As shown in Fig. 5.7(a), the edge of the squashed bead is smoothed out more broadly than the spherical bead, and the index histogram in Fig. 5.7(b) has a peak near 1.359 corresponding to an underestimation of 0.011. Interestingly, the index histogram has another peak near 1.34, which is an artifact caused by the missing cone. As for the spherical bead, the positivity constraint helps to recover the edge of the squashed bead. However, the index histogram predicts the refractive index of the squashed bead with 0.003 overestimation. In contrast, the iterative reconstruction used with the positivity and the piecewise smoothness constraints restores the edge more sharply, and predicts the refractive index within 0.001 accuracy.

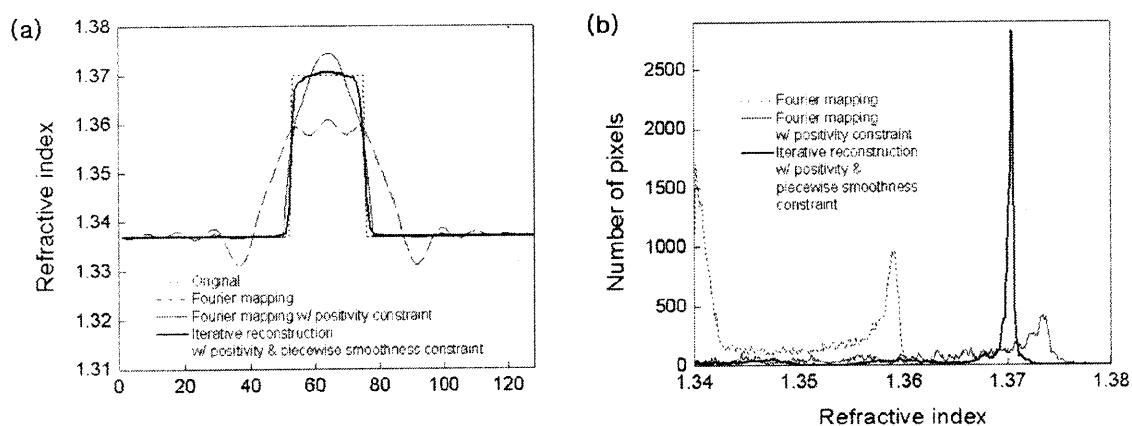


Figure 5.7. Simulation with a squashed bead in Fig. 6(a): (a) comparison of index profiles along the optical axis. (b) histograms of the 3-D refractive index map reconstructed by various methods.

It is important to note that the positivity constraint is given to the negative region mainly formed in outside of a sample, while the piecewise smoothness constraint is given to the overall region. For this reason the smoothness constraint may be more effective than the positivity constraint in a non-homogeneous sample containing various internal structures. Consider a sample consisting of two regions of different refractive index as in Fig. 5.8. This may be thought of as a simplified model of a biological cell with the inner part representing the nucleus.

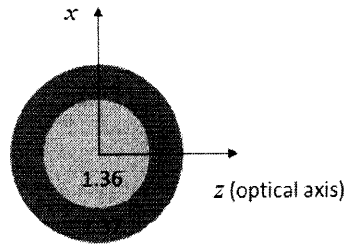


Figure 5.8. A non-homogeneous sample consisting of two regions of different refractive index. The numbers in the figure are the values of the refractive index.

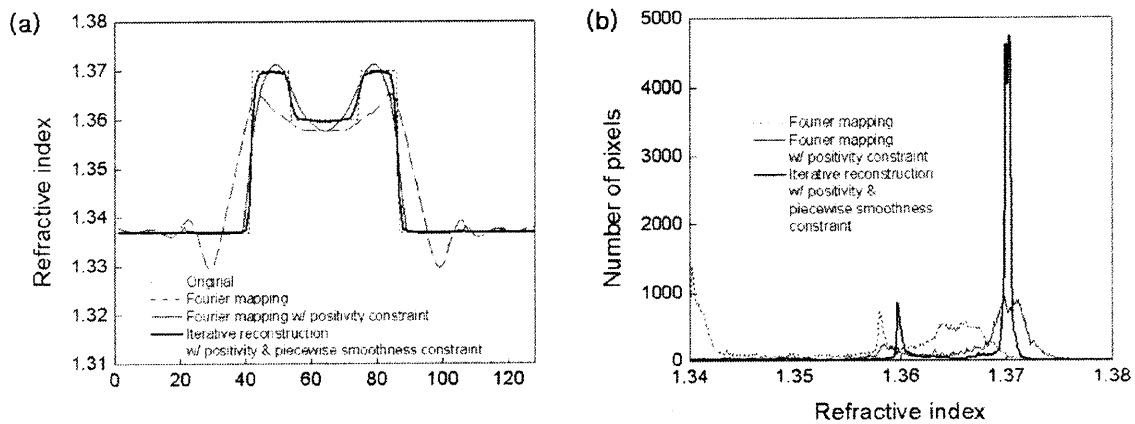


Figure 5.9. Simulation with a non-homogeneous sample representing a biological cell: (a) comparison of index profiles along the optical axis, (b) histograms of the 3-D refractive index map reconstructed by various methods.

Figure 5.9 shows refractive index profiles along the optical axis and corresponding index histograms for the sample shown above. From the Fourier mapping, the reconstructed sample has two boundaries, both of which are smoothed out by the missing cone, and the index histogram shows a similar underestimation of the refractive index for both regions. In case of the Fourier mapping with the positivity constraint, the outer boundary is restored, while the inner boundary shows considerable deviation from the original one. From the index histogram, the refractive index of the outer region is increased to near 1.37 although with some broadened profile. However, the peak for the inner region is not clear, but vaguely indicates somewhere below 1.36. In contrast, the iterative reconstruction together with the positivity and the

piecewise smoothness constraint restores the inner boundary as sharply as the outer one. What is more important, the index histogram indicates the refractive index for both regions is predicted within 0.001 accuracy. Since a biological sample consists of various organelles with different refractive index, the piecewise smoothness constraint would be critical for the accurate prediction of the refractive index of internal organelles.

5.3. Stain-Free Chromosome Imaging in Live Cells

5.3.1. Bead Calibration

Figure 5.10 is presents an example of using Fourier mapping and direct inversion, based on the Fourier diffraction theorem [32].

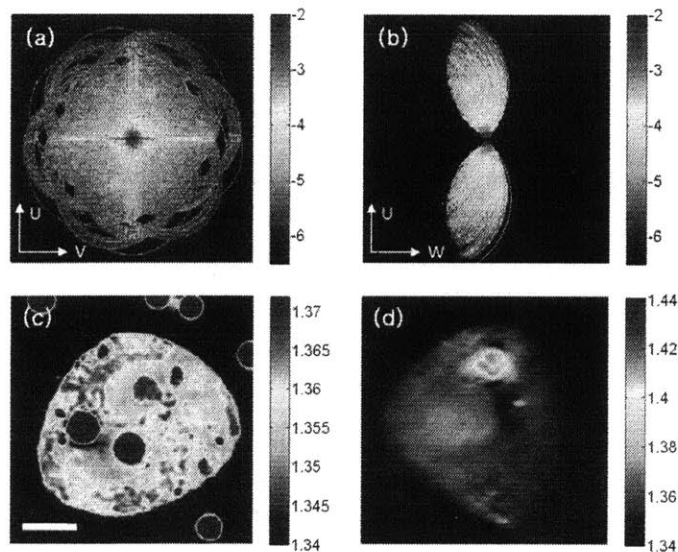


Figure 5.10. Fourier mapping and direct inversion: (a) horizontal and (b) vertical cross-sections of spatial frequency spectrum obtained from spiral beam scanning, (c) horizontal and (d) vertical cross-sections of reconstructed tomogram. The scale bar indicates 5 micron.

As shown in Fig. 5.10(a), the spiral scan of incident beam enables us to cover the full extent of the horizontal cross-section of spatial frequency spectrum within twice the numerical aperture. However, the

vertical cross-section in Fig. 5.10(b) indicates that there exists a region for which no data is available. The so-called missing cone is responsible for the elongation of a reconstructed tomogram along the direction of the optical axis and the systematic underestimation of refractive index as shown in Fig. 5.10(d). Except for the underestimation problem, the horizontal cross-section in Fig. 5.10(c) is good enough to show a detailed picture of internal organelles and well-defined cell boundary. The color scale in Fig. 5.10(c) was adjusted to show the internal organelles most clearly.

Next, the iterative reconstruction algorithm with the positivity and the piecewise-smoothness constraints was applied to the same data set as above [101]. Figures 5.11(a) and (b) show horizontal and vertical cross-sections of spatial frequency spectrum after 100 iterations. Importantly, the algorithm permitted the missing cone region of the spectrum to be filled with information with same magnitude as the measured data. Compared to Fig. 5.10(d), the vertical cross-section of the reconstructed tomogram in Fig. 5.11(d) has a significantly reduced height with an overall increase of refractive index value inside. From the tomogram, the refractive index of the silica bead underneath the HeLa cell is estimated to be 1.425 ± 0.005 , for which the standard deviation represents the spatial distribution of refractive index. To check the boundary-recovery capability of the new algorithm, we obtained the cell boundary using the LSCM, which is free from the missing-cone problem [102]. More specifically, we added fluorescein, which does not penetrate into the cell, to the medium, and then obtained the boundary as a negative of the image from the LSCM. It is shown in Fig. 5.11(e). Remarkably, that the cell boundary obtained by TPM is almost the same as that obtained using missing-cone-free LSCM.

The above improvement comes about due to the positivity and the piecewise-smoothness constraints together with the regularizing effect of the iterative algorithm itself [101]. The positivity constraint is a nonlinear process, generating new data in the missing cone region by out-of-band extrapolation [99, 100]. However, when used alone it generates large fluctuations in the reconstructed image. Additionally, its effect is mostly limited to the external structure of a sample; the missing-cone artifact on the internal organelles cannot be corrected by the positivity constraint alone. Hence, the piecewise-smoothness

constraint is necessary to smooth out the fluctuations and to eliminate the effect of the missing cone artifact on the internal organelles [86, 97, 101].

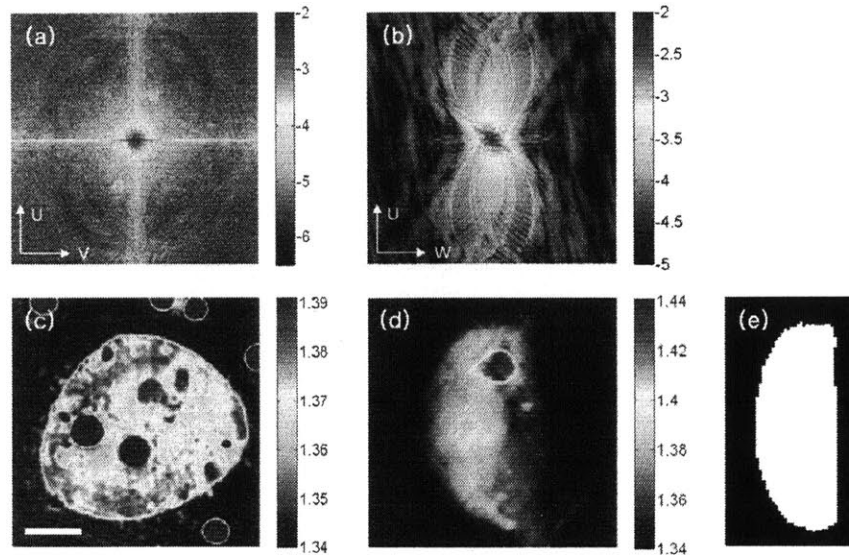


Figure 5.11. Iterative reconstruction with the positivity and the piecewise smoothness constraint: (a) horizontal and (b) vertical cross-sections of spatial frequency spectrum after 100 iteration, (c) horizontal and (d) vertical cross-sections of reconstructed tomogram, (e) vertical cross-section of cell boundary obtained by LSCM. The scale bar indicates 5 micron.

5.3.2. Dry Mass of Chromosomes

With the improved accuracy, we attempt to quantify the chromosomes in single living cells in their mitotic phase and determine the ploidy of the cells. Normal human somatic cells are diploid since they have 2×23 chromosomes. On the other hand, cancer cells tend to have either more or fewer number of chromosomes. Although some of cancer cells have the same ploidy as normal cells, they are less invasive than the rest. Therefore, measuring ploidy provides a good diagnosis of cancer cells. The current practice known as DNA analysis uses flow cytometry and fluorescent markers to perform the statistical analysis on number of cells. In our study, we quantify chromosome content from the 3D refractive index map of

chromosomes in single living cells in their native states. Using 4-pi TPM, we successfully differentiate two types of cancer cells, HT 29 and T84, both originated from the colon from the measured ploidy.

HeLa, HT-29 and T84 cells were cultured in Dulbecco modified Eagle medium (DMEM) supplemented with 10% FBS and 1% 100X penicillin-streptomycin solution. The cells were synchronized in metaphase by the Thymidine-Nocodazole block: 40% confluent cells were incubated for 24hrs in 2mM Thymidine, released for 3hrs in fresh medium, and then incubated for 12hrs in 200ng/ml Nocodazole. After the synchronization, the metaphase cells were collected by a centrifuge and resuspended in a culture medium containing 200ng/ml Nocodazole and 0.25 μ M nucleic acid stain fluorescent dye (SYTO 13, Invitrogen). A drop of cells from the suspension was spread on a Poly-L-lysine coated cover slip (40mm, round, no. 1), and then incubated for 30min in a CO₂ incubator.

The sample was observed on a wide-field microscope (Axio Observer.D1, Zeiss) to search for the cells with the condensed chromosomes aligned at the center. After that, the cell was brought into the field of view, and measured by 4- π TPM. From the reconstructed tomogram, the chromosome region was selected by thresholding. The threshold value was found by comparing the cross-section of the refractive index map and the boundary of the chromosome obtained by the fluorescence. Thus selected refractive index map of chromosome was integrated over the volume to provide the dry mass of the chromosome:

$$m_{chromosome} = 1/\alpha \iiint_{V_c} (n(x, y, z) - n_0) dV \quad (5.10)$$

in which V_c is the chromosome region selected by the thresholding, $\alpha=0.18$ (g/mL)⁻¹, n and n_0 are the refractive indices of the chromosome and medium, respectively.

Figure 5.12 shows the dry mass of chromosome of two human colon cancer cells, HT-29 and T84. The dry mass of HT-29 cells (42 ± 1.8 pg) is estimated to be about 18% larger than and that of T84 cells (34.6 ± 3.3 pg). This result consists with the cytogenetic analysis result provided by ATCC, in which the modal number of HT-29 cells (71) is about 21% larger than that of T84 cells (56).

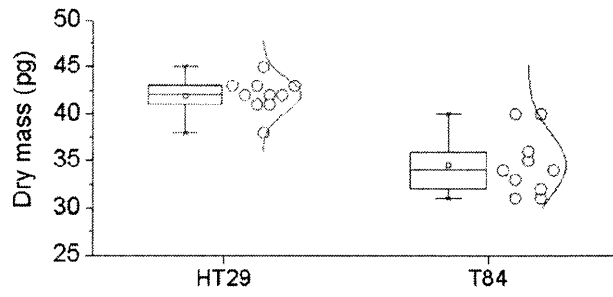


Figure 5.12. Dry mass of chromosomes. HT-29: 42 ± 1.8 , T84: 34.6 ± 3.3 (pg). These values consist with the modal number provided by ATCC through cytogenetic analysis (HT-29: 71, T84: 56).

Chapter 6

Summary and Future Directions

6.1. Summary

This thesis has explored three-dimensional (3-D) imaging modalities for refractive index measurement and some interesting biological studies utilizing their capability.

The theory of 3-D imaging using partially coherent light has been presented under the non-paraxial, but scalar and Debye, approximation. Starting from the optical transfer of the Green's function for the Helmholtz operator, we derived the image intensity in terms of the 3-D non-paraxial transmission cross-coefficient (TCC). By an inspection of the overlap integral, we derived a simple formula that can be efficiently calculated. Using this formula, we simulated phase contrast and Nomarski-DIC to image a modified 3-D Shepp-Logan phantom. The calculated images revealed major features of each technique, and the frequency response of the Nomarski-DIC was presented using the effective transfer function.

2-D quantitative phase imaging techniques to measure the sample-induced phase delay have been summarized. Tomographic phase microscopy (TPM) can provide the 3-D refractive index map of live biological samples. The original version of TPM adopted a filtered back-projection algorithm, which suffers from a diffraction artifact. We have shown that optical diffraction tomography based on scattering theory can remove this artifact. We have proved that the first-order Rytov approximation enables accurate

imaging of biological cells, whereas the first-order Born approximation causes distortion in the reconstructed images. The iterative constraint algorithm helps to reduce the effect of missing illumination and observation angles.

A tomographic method to synthesize the true projection of the refractive index map has been suggested. The method is free from diffraction artifacts and provides a low noise level of around 2.5 fg. We have measured division asymmetry of three types of eukaryotic cells, HT-29 (10.0 ± 6.4 (%)), RKO human colon cancer cells (13.0 ± 6.8 (%)) and L1210 mouse lymphoblast cells (7.5 ± 4.8 (%)). It is interesting to note that the division asymmetry differs between adherent cells (HT-29 and RKO cells) and floating cells (L1210 cells). Also, the two adherent cell types, both human colon cancer cells, have different division asymmetry. By measuring the dry mass distribution of newborn cells and mitotic cells in addition to the asynchronous populations, and using the Collins-Richmond model, we have measured the growth curve for two types of adherent cells, HT-29 and RKO cells. The measured growth curves have shown size-dependent growth rate, which supports the existence of an internal mechanism for growth control in adherent cells.

We have demonstrated the effect of drugs on multiple myeloma (MM) cells can be monitored by measuring the dry mass change within a treated group. The dry mass change by a drug (bortezomib) using the proteasome inhibition pathway is thought to be due to the accumulation of polyubiquitinated proteins or garbage proteins. Different response times to the same amount of drug (20nM) were observed in MM.1S (one hour) and RPMI8226 (four hours) cells, which had been known to have different drug sensitivities. The increase of dose from 50% of EC_{50} to twice EC_{50} shortened the response time of RPMI8226 cells to drug from four hours to one hour, but the dry mass increase due to the treatment was the same in both groups. For all the observations made, it was shown that the dry mass measurement is capable of monitoring drug effect on MM cells without adding any extra contrast agent.

We have applied the deterministic regularization algorithm to 3-D optical diffraction tomography. Using constraints of piecewise smoothness and positivity constraint as prior information, we were able to suppress both the missing cone artifact and noise. In a numerical simulation, we were able to predict the refractive index to an accuracy within 0.001 irrespective of the shape of the sample, using a practically attainable angular coverage from -60° to 60° . Using the suggested algorithm, we have shown that the refractive index of a silica bead in a HeLa cell can be predicted accurately, which demonstrates our capability of measuring the refractive index of internal organelles. With the improved accuracy, we have quantified the dry mass of chromosomes in HT-29 and T84 human colon cancer cells synchronized at metaphase. The dry mass of HT-29 cells (42 ± 1.8 pg) was estimated to be about 18% larger than and that of T84 cells (34.6 ± 3.3 pg), which consists with the cytogenetic analysis result, in which the modal number of HT-29 cells (71) is about 21% larger than that of T84 cells (56).

6.2. Future Directions

Tomographic phase microscopy (TPM) can theoretically have two times higher resolution than the diffraction limit in the transverse direction, while its axial resolution remains the same as the diffraction limit [32, 103]. In real practice, however, the lateral resolution is close to the diffraction limit and axial resolution is significantly worse than the limit. This is mainly because of the limited angular coverage and the way we change the illumination direction with respect to a sample. Figure 6.1(a) shows the transfer function of the diffraction tomography when data is acquired only in transmission mode. The volume of support is the trace of the Ewald sphere moving across spatial frequency space as the illumination angle is scanned. The height of the donut-shaped transfer function is smaller than the width, which means the axial resolution is poorer than the transverse resolution. In order to solve the practical problem of missing angles, the reflection mode detection will need to be incorporated in addition to the transmission mode. This will result in the enlargement of spectral coverage as shown in the right-hand figure of Figure 6.1(b).

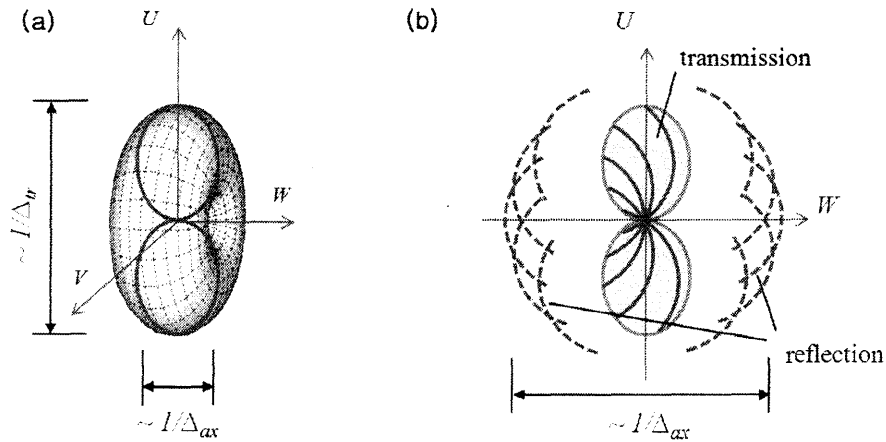


Figure 6.1. (a) Transfer function of diffraction tomography in transmission mode. Transverse resolution is inversely proportional to the width of the diameter of the torus, and axial resolution to the height. (b) U - W cross-section of the transfer function in transmission and reflection mode. The addition of the reflection mode tomography provides better axial resolution by sampling high spatial frequency in axial direction.

Long-term observation of biological specimens is critical in many applications including cell cycle studies and monitoring the roles of various chemicals inducing such effects as apoptosis in cancer cells. The label-free and 3-D imaging capability of TPM makes it highly appropriate for the long-term observation of biological specimens because it is free from the artifacts of the exogenous agents – invasiveness, non-uniform binding and temporal degradation of signals. However, the need for high-numerical-aperture objective and condenser lenses, whose working distances are extremely short, prevents the use of a conventional live cell chambers. In the current TPM setup, the cell samples are viable for longer than 30 hours, but they are not guaranteed to be in a healthy state. It may be necessary to further optimize parameters such as the temperature and flow rate of the culture medium, amount of exposure to the light, etc.

TPM can provide a 3-D refractive index map of a live cell, which has found many important biological applications as described earlier. However, its limited throughput has prevented us from acquiring the large amounts of statistical data necessary to account for the complexity of biological studies. We note that micro-fluidics has a unique feature that can reinforce the benefits of TPM: flowing and manipulating

cells while taking various measurements. The technique has been successfully applied in the commercial systems such as Coulter counter, FACS (Fluorescence-activated cell sorter), etc. Here, we propose to integrate the high-speed tomographic phase microscopy with a micro-fluidic system to rapidly and reliably transport a large number of cells through the microscope field-of-view. This will make TPM a high-throughput, label-free imaging device that will permit statistical studies to be performed and target cells from the pool to be screened.

As an initial step for this implementation, our group had conducted a preliminary study [104]. The so-called synthetic aperture tomography showed that a sample in translational motion can be imaged by the tomographic phase microscopy. We note that this previous study requires two major improvements in order to be adapted to with micro-fluidic studies: imaging with continuous flow and enhanced spatial resolution. In a micro-fluidic channel, the cells usually move fast, tumble up and down, and rotate in a random direction. In order to resolve this issue, we firstly need to flow cells in a well-controlled manner. It will be necessary to design a specialized micro-fluidic channel to realize a laminar flow in the sampling region. Also, the overall thickness of the channel will need to be reduced to fit within the small gap between the condenser and objective lenses. The residual disturbance of the sample such as rotation and tumbling may be compensated during image post-processing. Secondly, the imaging resolution needs to be improved. In the previous proof-of-concept study, the NA of the system was not high enough to clearly resolve internal organelles. The cylindrical lenses induced aberration especially for the high-spatial-frequency components of the optical signals so that the NA had to be reduced well below the system NA. As a result, the reconstructed image had a poorer resolution than the original TPM. It will be helpful to design a lens system in such a way as to minimize the aberration and thus to make full use of the available NA. In conjunction with this hardware improvement, it will be necessary to implement a diffraction tomography algorithm for focused-illumination images to remove the diffraction artifact of the previous approach.

References

1. W. Denk, J. H. Strickler, and W. W. Webb, "Two-photon laser scanning fluorescence microscopy," *Science* **248**, 73 (1990).
2. M. J. Rust, M. Bates, and X. Zhuang, "Sub-diffraction-limit imaging by stochastic optical reconstruction microscopy (STORM)," *Nature methods* **3**, 793-796 (2006).
3. B. Huang, W. Wang, M. Bates, and X. Zhuang, "Three-dimensional super-resolution imaging by stochastic optical reconstruction microscopy," *Science* **319**, 810 (2008).
4. S. W. Hell, "Toward fluorescence nanoscopy," *Nature biotechnology* **21**, 1347-1355 (2003).
5. P. T. C. So, C. Y. Dong, B. R. Masters, and K. M. Berland, "Two-photon excitation fluorescence microscopy," *Annual Review of Biomedical Engineering* **2**, 399-429 (2000).
6. J. R. Lakowicz and B. R. Masters, "Principles of fluorescence spectroscopy," *Journal of Biomedical Optics* **13**, 029901 (2008).
7. F. Zernike, "Phase contrast, a new method for the microscopic observation of transparent objects," *Physica* **9**, 686-698 (1942).
8. G. Nomarski, "Microinterféromètre différentiel à ondes polarisées," *J. Phys. Radium* **16**, 9S-13S (1955).
9. T. Ikeda, G. Popescu, R. R. Dasari, and M. S. Feld, "Hilbert phase microscopy for investigating fast dynamics in transparent systems," *Opt. Lett* **30**, 1165-1167 (2005).
10. C. Fang-Yen, S. Oh, Y. Park, W. Choi, S. Song, H. S. Seung, R. R. Dasari, and M. S. Feld, "Imaging voltage-dependent cell motions with heterodyne Mach-Zehnder phase microscopy," *Optics Letters* **32**, 1572-1574 (2007).
11. H. Iwai, C. Fang-Yen, G. Popescu, A. Wax, K. Badizadegan, R. R. Dasari, and M. S. Feld, "Quantitative phase imaging using actively stabilized phase-shifting low-coherence interferometry," *Optics Letters* **29**, 2399-2401 (2004).
12. Nikon, "Introduction to Phase Contrast Microscopy," MICROSCOPYU (<http://www.microscopyu.com/articles/phasecontrast/phasemicroscopy.html>).
13. H. Köhler, "On Abbe's Theory of Image Formation in the Microscope," *Journal of Modern Optics* **28**, 1691-1701 (1981).
14. R. Barer, "Refractometry and interferometry of living cells," *JOSA* **47**, 545-556 (1957).
15. R. Barer and S. Tkaczyk, "Refractive index of concentrated protein solutions," (1954).

16. J. W. Goodman, "Statistical optics," New York, Wiley-Interscience, 1985, 567 p. **1**(1985).
17. E. Abbe, "Beiträge zur Theorie des Mikroskops und der mikroskopischen Wahrnehmung," *Archiv für mikroskopische Anatomie* **9**, 413-418 (1873).
18. J. W. Goodman, *Introduction to Fourier optics* (Roberts & Company Publishers, 2005).
19. H. Hopkins, "On the diffraction theory of optical images," *Proceedings of the Royal Society of London. Series A. Mathematical and Physical Sciences* **217**, 408 (1953).
20. C. J. R. Sheppard and T. Wilson, "Fourier imaging of phase information in scanning and conventional optical microscopes," *Philosophical Transactions of the Royal Society of London. Series A, Mathematical and Physical Sciences* **295**, 513 (1980).
21. C. McCutchen, "Generalized aperture and the three-dimensional diffraction image," *J. Opt. Soc. Am* **54**, 240-244 (1964).
22. B. Frieden, "Optical transfer of the three-dimensional object," *JOSA* **57**, 56-65 (1967).
23. C. Sheppard, M. Gu, Y. Kawata, and S. Kawata, "Three-dimensional transfer functions for high-aperture systems," *Journal of the Optical Society of America A* **11**, 593-598 (1994).
24. N. Streibl, "Fundamental restrictions for 3-D light distributions," *Optik* **66**, 341-354 (1984).
25. N. Streibl, "Depth transfer by an imaging system," *Journal of Modern Optics* **31**, 1233-1241 (1984).
26. N. Streibl, "Three-dimensional imaging by a microscope," *Journal of the Optical Society of America A* **2**, 121-127 (1985).
27. C. Sheppard and X. Mao, "Three-dimensional imaging in a microscope," *Journal of the Optical Society of America A* **6**, 1260-1269 (1989).
28. A. Marathay, "Fourier transform of the Green's function for the Helmholtz equation," *JOSA* **65**, 964-965 (1975).
29. E. Wolf, "Three-dimensional structure determination of semi-transparent objects from holographic data," *Optics Communications* **1**, 153-156 (1969).
30. E. Brigham and R. Morrow, "The fast Fourier transform," *Spectrum, IEEE* **4**, 63-70 (2009).
31. M. Kalashnikov, W. Choi, C. Yu, Y. Sung, R. Dasari, K. Badizadegan, and M. Feld, "Assessing light scattering of intracellular organelles in single intact living cells," *Optics express* **17**, 19674-19681 (2009).
32. Y. Sung, W. Choi, C. Fang-Yen, K. Badizadegan, R. Dasari, and M. Feld, "Optical diffraction tomography for high resolution live cell imaging," *Optics express* **17**, 266-277 (2009).
33. C. Cogswell and C. Sheppard, "Confocal differential interference contrast (DIC) microscopy: including a theoretical analysis of conventional and confocal DIC imaging," *Journal of microscopy* **165**, 81-101 (1992).
34. S. Mehta and C. Sheppard, "Partially coherent image formation in differential interference contrast (DIC) microscope," *Optics express* **16**, 19462-19479 (2008).

35. C. Preza, D. Snyder, and J. Conchello, "Theoretical development and experimental evaluation of imaging models for differential-interference-contrast microscopy," *J. Opt. Soc. Am. A* **16**, 2185–2199 (1999).
36. M. R. Teague, "Deterministic phase retrieval- A Green's function solution," *Optical Society of America, Journal* **73**, 1434-1441 (1983).
37. N. Streibl, "Phase imaging by the transport equation of intensity," *Optics Communications* **49**, 6-10 (1984).
38. L. Waller, L. Tian, and G. Barbastathis, "Transport of Intensity phase-amplitude imaging with higher order intensity derivatives," *Optics express* **18**, 12552-12561 (2010).
39. W. Choi, C. Fang-Yen, K. Badizadegan, S. Oh, N. Lue, R. Dasari, and M. Feld, "Tomographic phase microscopy," *Nature methods* **4**, 717-719 (2007).
40. C. Fang-Yen, W. Choi, Y. Sung, C. J. Holbrow, R. R. Dasari, and M. S. Feld, "Video-rate tomographic phase microscopy," *Journal of Biomedical Optics* **16**, 011005 (2011).
41. Y. K. Park, M. Diez-Silva, G. Popescu, G. Lykotrafitis, W. Choi, M. S. Feld, and S. Suresh, "Refractive index maps and membrane dynamics of human red blood cells parasitized by *Plasmodium falciparum*," *Proceedings of the National Academy of Sciences* **105**, 13730 (2008).
42. B. Khaykovich, N. Kozlova, W. Choi, A. Lomakin, C. Hossain, Y. Sung, R. R. Dasari, M. S. Feld, and G. B. Benedek, "Thickness–radius relationship and spring constants of cholesterol helical ribbons," *Proceedings of the National Academy of Sciences* **106**, 15663 (2009).
43. A. Barty, K. Nugent, A. Roberts, and D. Paganin, "Quantitative phase tomography," *Optics Communications* **175**, 329-336 (2000).
44. W. Gorski and W. Osten, "Tomographic imaging of photonic crystal fibers," *Optics Letters* **32**, 1977-1979 (2007).
45. F. Charri re, N. Pavillon, T. Colomb, C. Depeursinge, T. J. Heger, E. A. D. Mitchell, P. Marquet, and B. Rappaz, "Living specimen tomography by digital holographic microscopy: morphometry of testate amoeba," *Optics express* **14**, 7005-7013 (2006).
46. V. Lauer, "New approach to optical diffraction tomography yielding a vector equation of diffraction tomography and a novel tomographic microscope," *Journal of microscopy* **205**, 165-176 (2002).
47. A. C. Kak and M. Slaney, "Principles of computerized tomographic imaging," (1988).
48. K. Tam and V. Perez-Mendez, "Tomographical imaging with limited-angle input," *JOSA* **71**, 582-592 (1981).
49. B. P. Medoff, W. R. Brody, M. Nassi, and A. Macovski, "Iterative convolution backprojection algorithms for image reconstruction from limited data," *J. Opt. Soc. Am* **73**, 1493-1500 (1983).
50. A. Devaney, "Inverse-scattering theory within the Rytov approximation," *Optics Letters* **6**, 374-376 (1981).
51. B. E. A. Saleh, M. C. Teich, and B. E. Saleh, "Fundamentals of photonics," (1991).

52. C. Kittel and P. McEuen, *Introduction to solid state physics* (Wiley New York, 1986), Vol. 4.
53. S. Al-Ani and C. Hogarth, "Correlation of refractive index and density in high refractive index glasses," *Journal of materials science letters* **6**, 519-521 (1987).
54. J. D. Watson, "Molecular biology of the gene," *Molecular biology of the gene*. (1970).
55. G. Popescu, Y. K. Park, N. Lue, C. Best-Popescu, L. Deflores, R. R. Dasari, M. S. Feld, and K. Badizadegan, "Optical imaging of cell mass and growth dynamics," *American Journal of Physiology-Cell Physiology* **295**, C538 (2008).
56. M. N. Hall, M. C. Raff, and G. Thomas, *Cell growth: control of cell size* (CSHL Press, 2004).
57. S. Elliott and C. McLaughlin, "Rate of macromolecular synthesis through the cell cycle of the yeast *Saccharomyces cerevisiae*," *Proceedings of the National Academy of Sciences of the United States of America* **75**, 4384 (1978).
58. P. Jorgensen and M. Tyers, "How cells coordinate growth and division," *Current biology* **14**, R1014-R1027 (2004).
59. P. Echave, I. J. Conlon, and A. C. Lloyd, "Cell size regulation in mammalian cells," *Cell cycle* **6**, 218-224 (2007).
60. A. Tzur, R. Kafri, V. S. LeBleu, G. Lahav, and M. W. Kirschner, "Cell growth and size homeostasis in proliferating animal cells," *Science* **325**, 167 (2009).
61. M. Godin, F. F. Delgado, S. Son, W. H. Grover, A. K. Bryan, A. Tzur, P. Jorgensen, K. Payer, A. D. Grossman, and M. W. Kirschner, "Using buoyant mass to measure the growth of single cells," *Nature methods* **7**, 387-390 (2010).
62. K. Park, L. J. Millet, N. Kim, H. Li, X. Jin, G. Popescu, N. Aluru, K. J. Hsia, and R. Bashir, "Measurement of adherent cell mass and growth," *Proceedings of the National Academy of Sciences* **107**, 20691 (2010).
63. G. I. Bell and E. C. Anderson, "Cell Growth and Division:: I. A Mathematical Model with Applications to Cell Volume Distributions in Mammalian Suspension Cultures," *Biophysical Journal* **7**, 329-351 (1967).
64. J. Collins and M. Richmond, "Rate of growth of *Bacillus cereus* between divisions," *Microbiology* **28**, 15 (1962).
65. E. Parzen, "On estimation of a probability density function and mode," *The Annals of Mathematical Statistics* **33**, 1065-1076 (1962).
66. M. Rosenblatt, "Remarks on some nonparametric estimates of a density function," *The Annals of Mathematical Statistics* **27**, 832-837 (1956).
67. Z. Botev, "Kernel Density Estimator," MATLAB Central File Exchange (2007).
68. A. F. Kisselev and A. L. Goldberg, "Proteasome inhibitors: from research tools to drug candidates," *Chemistry & biology* **8**, 739-758 (2001).
69. W. M. Kuehl and P. L. Bergsagel, "Multiple myeloma: evolving genetic events and host interactions," *Nature Reviews Cancer* **2**, 175-187 (2002).

70. P. G. Richardson, P. Sonneveld, M. Schuster, D. Irwin, E. Stadtmauer, T. Facon, J. L. Harousseau, D. Ben-Yehuda, S. Lonial, and H. Goldschmidt, "Extended follow-up of a phase 3 trial in relapsed multiple myeloma: final time-to-event results of the APEX trial," *Blood* **110**, 3557 (2007).
71. P. G. G. Richardson, B. Barlogie, J. Berenson, S. Singhal, S. Jagannath, D. Irwin, S. V. Rajkumar, T. Hideshima, H. Xiao, and D. Esseltine, "Clinical factors predictive of outcome with bortezomib in patients with relapsed, refractory multiple myeloma," *Blood* **106**, 2977 (2005).
72. K. C. Anderson, "Moving disease biology from the lab to the clinic," *Cancer* **97**, 796-801 (2003).
73. K. C. Anderson and I. M. Ghobrial, *Multiple Myeloma: Translational and Emerging Therapies* (Informa Healthcare, 2007).
74. M. Glotzer, A. W. Murray, and M. W. Kirschner, "Cyclin is degraded by the ubiquitin pathway," *Nature* **349**, 132-138 (1991).
75. J. Wang and M. A. Maldonado, "The ubiquitin-proteasome system and its role in inflammatory and autoimmune diseases," *Cell Mol Immunol* **3**, 255-261 (2006).
76. D. Hamahan and J. Folkman, "Patterns and emerging mechanisms of the angiogenesis switch during tumorigenesis," *Cell* **86**, 354-364 (1997).
77. A. L. Haas, J. Warms, A. Hershko, and I. A. Rose, "Ubiquitin-activating enzyme. Mechanism and role in protein-ubiquitin conjugation," *Journal of Biological Chemistry* **257**, 2543 (1982).
78. L. M. Schwartz, A. Myer, L. Kosz, M. Engelstein, and C. Maier, "Activation of polyubiquitin gene expression during developmentally programmed cell death," *Neuron* **5**, 411-419 (1990).
79. J. Adams, *Proteasome inhibitors in cancer therapy* (Humana Pr Inc, 2004).
80. J. S. Thrower, L. Hoffman, M. Rechsteiner, and C. M. Pickart, "Recognition of the polyubiquitin proteolytic signal," *The EMBO Journal* **19**, 94-102 (2000).
81. E. P. Risseuw, T. E. Daskalchuk, T. W. Banks, E. Liu, J. Cotelesage, H. Hellmann, M. Estelle, D. E. Somers, and W. L. Crosby, "Protein interaction analysis of SCF ubiquitin E3 ligase subunits from Arabidopsis," *The Plant Journal* **34**, 753-767 (2003).
82. G. Bianchi, L. Oliva, P. Cascio, N. Pengo, F. Fontana, F. Cerruti, A. Orsi, E. Pasqualetto, A. Mezghrani, and V. Calbi, "The proteasome load versus capacity balance determines apoptotic sensitivity of multiple myeloma cells to proteasome inhibition," *Blood* **113**, 3040 (2009).
83. A. Devaney, "A filtered backpropagation algorithm for diffraction tomography," *Ultrasonic imaging* **4**, 336-350 (1982).
84. G. Tsihrintzis and A. Devaney, "Higher-order (nonlinear) diffraction tomography: reconstruction algorithms and computer simulation," *Image Processing, IEEE Transactions on* **9**, 1560-1572 (2002).
85. M. Defrise and C. De Mol, "A regularized iterative algorithm for limited-angle inverse Radon transform," *Journal of Modern Optics* **30**, 403-408 (1983).

86. A. Delaney and Y. Bresler, "Globally convergent edge-preserving regularized reconstruction: an application to limited-angle tomography," *Image Processing, IEEE Transactions on* **7**, 204-221 (2002).
87. M. Persson, D. Bone, and H. Elmqvist, "Total variation norm for three-dimensional iterative reconstruction in limited view angle tomography," *Physics in Medicine and Biology* **46**, 853 (2001).
88. A. Zunino, F. Benvenuto, E. Armadillo, M. Bertero, and E. Bozzo, "Iterative deconvolution and semiblind deconvolution methods in magnetic archaeological prospecting," *Geophysics* **74**, L43 (2009).
89. M. Bronstein, A. Bronstein, M. Zibulevsky, and H. Azhari, "Reconstruction in diffraction ultrasound tomography using nonuniform FFT," *Medical Imaging, IEEE Transactions on* **21**, 1395-1401 (2003).
90. F. Charrière, A. Marian, F. Montfort, J. Kuehn, T. Colomb, E. Cuche, P. Marquet, and C. Depeursinge, "Cell refractive index tomography by digital holographic microscopy," *Optics Letters* **31**, 178-180 (2006).
91. K. Lada and A. Devaney, "Iterative methods in geophysical diffraction tomography," *Inverse Problems* **8**, 119 (1992).
92. M. Bertero and P. Boccacci, *Introduction to inverse problems in imaging* (Taylor & Francis, 1998).
93. M. Piana and M. Bertero, "Projected Landweber method and preconditioning," *Inverse Problems* **13**, 441 (1997).
94. K. Ladas and A. Devaney, "Generalized ART algorithm for diffraction tomography," *Inverse Problems* **7**, 109 (1991).
95. M. Schabel, "3D Shepp-Logan phantom," MATLAB Central File Exchange (2006).
96. C. Vogel, *Computational methods for inverse problems* (Society for Industrial Mathematics, 2002).
97. P. Charbonnier, L. Blanc-Feraud, G. Aubert, and M. Barlaud, "Deterministic edge-preserving regularization in computed imaging," *Image Processing, IEEE Transactions on* **6**, 298-311 (2002).
98. A. Kak and M. Slaney, "Principles of computerized tomographic imaging," (1988).
99. R. Gerchberg, "Super-resolution through error energy reduction," *Journal of Modern Optics* **21**, 709-720 (1974).
100. A. PAPOULIS, "A New Algorithm in Spectral Analysis and Band-Limited Extrapolation," *IEEE TRANSACTIONS ON CIRCUITS AND SYSTEMS* **22**, 735 (1975).
101. Y. Sung and R. Dasari, "Deterministic regularization of three-dimensional optical diffraction tomography," *Optics express*.
102. J. Pawley and B. Masters, "Handbook of biological confocal microscopy," *Journal of Biomedical Optics* **13**, 029902 (2008).

103. O. Haeberlé, K. Belkebir, H. Giovaninni, and A. Sentenac, "Tomographic diffractive microscopy: basics, techniques and perspectives," *Journal of Modern Optics* **57**, 686-699 (2010).
104. N. Lue, W. Choi, G. Popescu, K. Badizadegan, R. R. Dasari, and M. S. Feld, "Synthetic aperture tomographic phase microscopy for 3D imaging of live cells in translational motion," *Optics express* **16**, 16240-16246 (2008).